Faculteit Wetenschappen
Departement Fysica

Model-based reconstruction algorithms for dynamic X-ray CT

Modelgebaseerde reconstructiealgoritmes voor dynamische X-stralen CT

Proefschrift voorgelegd tot het behalen van de graad van

Doctor in de Wetenschappen: Fysica

aan de Universiteit Antwerpen, te verdedigen door

Vincent Van Nieuwenhove

Promotoren:
Prof. dr. Jan Sijbers
Dr. ir. Jan De Beenhouwer

Antwerpen, 2017

Doctoral committee

Prof. dr. Sara Bals
Dr. ir. Jan De Beenhouwer
Prof. dr. Joris Dirckx
Prof. dr. Jan Sijbers

Other jury members

Prof. dr. Bernadette Hahn
Prof. dr. Greet Kerckhofs
Dr. Lucia Mancini

Contact information:

✉ **Vincent Van Nieuwenhove**
imec-Vision Lab, Dept. of Physics
University of Antwerp (CDE)
Universiteitsplein 1, Building N1.11
B-2610 Wilrijk, Antwerpen, Belgium
☎ +32 (0)3 265 24 49
+32 (0)495 90 41 82
Vincent.VanNieuwenhove@uantwerpen.be
http://visielab.uantwerpen.be/people/vincent-van-nieuwenhove

Table of Contents

Table of Contents iii

Samenvatting v

Summary ix

1 Introduction 1
- 1.1 X-ray imaging 3
  - 1.1.1 X-ray generation 3
  - 1.1.2 X-ray matter interaction 5
  - 1.1.3 X-ray detection 8
  - 1.1.4 Projection geometries 8
- 1.2 Computed tomography 8
  - 1.2.1 Analytical reconstruction algorithms 10
  - 1.2.2 Algebraic reconstruction algorithms 16
  - 1.2.3 Statistical reconstruction algorithms 21
- 1.3 Dynamic computed tomography 21
  - 1.3.1 Dynamic tomographic model 21
  - 1.3.2 4D-CT 22
  - 1.3.3 Deformation correction 24
  - 1.3.4 Applications 24
- References 26

2 Dynamic intensity normalization 33
- 2.1 Introduction 34
- 2.2 Method 35
  - 2.2.1 Conventional flat field correction 35
  - 2.2.2 Dynamic flat field correction 36
- 2.3 Experiments 40
  - 2.3.1 Simulation study 40
  - 2.3.2 Experimental data 42
- 2.4 Results and discussion 43
  - 2.4.1 Simulation study 43
  - 2.4.2 Experimental data 45
  - 2.4.3 General remarks 50
- 2.5 Conclusion 52
- References 52

3 **Affine deformation estimation and correction** **55**
3.1 Introduction 56
3.2 Method 57
3.2.1 Definitions 57
3.2.2 Affine transformation and cone beam projections 58
3.2.3 Estimation of motion/deformation parameters 59
3.3 Experiments 65
3.3.1 Phantom study 65
3.3.2 Real data 68
3.4 Results and discussion 69
3.4.1 Phantom study 69
3.4.2 Real data 72
3.4.3 4D reconstructions 76
3.4.4 Medical applications 76
3.5 Conclusion 76
3.6 Appendix 77
References 78

4 **MoVIT** **83**
4.1 Introduction 84
4.2 Method 85
4.2.1 Stationary algebraic tomography 85
4.2.2 Dynamic tomographic model 86
4.2.3 MotionVector-based Iterative Technique 87
4.2.4 Deformation estimation 89
4.3 Experiments and results 90
4.3.1 Reconstruction methods 90
4.3.2 Figures of merit 91
4.3.3 Numerical simulations 91
4.3.4 Polyurethane dataset 92
4.4 Discussion 100
4.4.1 Numerical simulations 100
4.4.2 Polyurethane dataset 100
4.5 Conclusion 101
References 101

5 **Conclusions** **105**

A **List of common abbreviations** **109**

B **Scientific contributions** **111**

Samenvatting

X-stralen computertomografie (CT) is een krachtige, niet-destructieve beeldvormingstechniek om het inwendige van een gescand object te visualiseren. Op basis van meerdere X-stralen beelden die uit verschillende richtingen zijn opgenomen kan een 3D model van het sample worden berekend met behulp van een reconstructiealgoritme. Doordat CT een zeer flexibele beeldvormingstechniek is, kan het gebruikt worden in een brede waaier aan toepassingen zoals medische, biomedische en industriële beeldvorming.

Om accurate visualisaties van het interne van een object te verkrijgen moet het beeldvormingsproces en het object zelf accuraat gemodelleerd worden. Standaard CT-algoritmes modeleren deze processen als zijnde stationair. Helaas wordt er aan deze stationariteitsvoorwaarde vaak niet voldaan. Indien de dynamica niet-verwaarloosbaar is, zorgt het nalaten van haar modellering voor artefacten in de reconstructiebeelden. Om deze artefacten te vermijden (of te verminderen) zullen er in dit werk verschillende dynamische processen gemodelleerd en vervolgens geïncorporeerd worden in een reeks CT-algoritmes.

In hoofdstuk 2 wordt er gefocust op de dynamica van het beeldvormingsproces. Meer specifiek, er zal een geavanceerd normalisatiealgoritme voor X-stralenprojecties worden voorgesteld. Dit algoritme compenseert voor de instabiliteit van de inkomende X-stralenbundel, een probleem dat vaak in synchrotron lichtbronnen wordt tegengekomen en resulteert in systematische fouten in de genormaliseerde beelden.

In de daaropvolgende hoofdstukken wordt er gefocust op dynamische computertomografie. Gedurende een dynamische tomografieopname is het object niet langer stationair. Hierdoor zijn er twee belangrijke uitdagingen: Ten eerste veroorzaakt de vervorming van het object zogenaamde bewegingsartefacten waardoor de reconstructiebeelden onscherp zijn en verdubbelingen van structuren kunnen vertonen. Ten tweede is de gebruiker vaak geïnteresseerd in de dynamica van het proces op zich en niet enkel in het 3D-model van het object. Hiervoor moet het proces met een voldoende hoge tijdsresolutie worden opgenomen, wat niet evident is met de trage CT-acquisitie. Om deze problemen te overwinnen werden er twee algoritmes ontwikkeld: een affien deformatiecorrectiealgoritme (Hoofdstuk 3) en een 4D-CT reconstructiekader (Hoofdstuk 4).

In de volgende secties wordt een samenvatting van de verschillende hoofdstukken gegeven.

Hoofdstuk 1 – Inleiding

In dit hoofdstuk wordt de basis van X-stralenbeeldvorming, computertomografie en dynamische computertomografie voorgesteld. Deze kennis zal veelvuldig gebruikt worden in de daaropvolgende hoofdstukken.

Hoofdstuk 2 – Dynamische intensiteitsnormalisatie

In dit hoofdstuk wordt een geavanceerde projectienormalisatietechniek geïntroduceerd die de dynamica van het X-stralen beeldvormingssysteem in rekening brengt. In CT wordt typisch de opgenomen projectiedata genormaliseerd met gemiddelde flat fields (X-ray beelden opgenomen zonder voorwerp) die voor de scan worden opgenomen. Jammer genoeg zijn deze flat fields in een synchrotron vaak niet-statisch door vibrerende beamline componenten zoals de monochromator, tijdsveranderende detectoreigenschappen en andere factoren. Deze dynamica zorgt voor significante systematische fouten in de intensiteitsnormalisatie.

Daarom wordt in de voorgestelde techniek de dynamica van deze flat fields in rekening gebracht. Door middel van hoofdcomponentenanalyse van een set van flat fields wordt er een set eigen flat fields berekend. Een lineaire combinatie van deze eigen flat fields wordt dan gebruikt om elke projectie individueel te corrigeren.

Experimenten tonen aan dat de voorgestelde dynamische flat field correctie leidt tot een substantiële vermindering van de systematische fouten in de intensiteitsnormalisatie van de projecties in vergelijking met conventionele flat field correctie.

Hoofdstuk 3 – Affiene deformatieschatting en correctie in cone-beam computertomografie

In micro-CT komen lange acquisitietijden, in de grootteorde van uren, vaak voor. Dit is nodig om een voldoende hoge signaal-ruisverhouding en spatiale resolutie te verkrijgen. Deze lange acquisitietijden worden vooral veroorzaakt door de lage X-stralen flux die typisch wordt terug gevonden in deze scanners. Daardoor is er gedurende deze opnames een hoog risico op sample beweging of vervorming. Tomografische reconstructiealgoritmes die deze dynamica niet in rekening brengen, krijgen te maken met bewegingsartefacten in de reconstructiebeelden, waardoor de beelden vaag zijn en strepen vertonen.

Om deze artefacten tegen te gaan, wordt er een efficiënt algoritme geïntroduceerd om globale affiene deformaties direct te corrigeren op de cone-beam projecties. Hiervoor wordt een relatie tussen de affiene transformatie en de cone-beam transformatie bewezen en gebruikt. De parameters die de deformatie loodrecht op de projectierichting beschrijven worden voor elke projectie individueel geschat door het minimaliseren van een vlak gebaseerd inconsistentiecriterium. Het criterium vergelijkt elke projectie van de hoofdscan met alle projecties van een korte referentiescan die voor of na de hoofdscan wordt opgenomen. De voorgestelde techniek is data gebaseerd waardoor het plaatsen van markers of het gebruik van trackingsystemen vermeden wordt.

Experimenten, met gesimuleerde en experimentele data, tonen aan dat het voorgestelde affiene deformatieschatting en correctiealgoritme in staat is om een substantiële reductie van de bewegingsartefacten in cone-beam CT reconstructiebeelden te realiseren.

Hoofdstuk 4 – MoVIT: Een tomografisch reconstructiekader voor 4D-CT

4D computertomografie (4D-CT) tracht de temporele dynamica van een 3D sample te visualiseren met een voldoende hoge temporele en spatiale resolutie. Opeenvolgende tijdspannes worden typisch sequentieel opgenomen, gevolgd door de reconstructie van elke afzonderlijk tijdsspanne. Deze benadering heeft veel projecties per scan nodig om reconstructiebeelden met een voldoende hoge kwaliteit (in termen van artefacten en signaal-ruisverhouding) te verkrijgen. Bij gevolg is er een balans tussen de rotatiesnelheid van de bron en detector en de kwaliteit van de reconstructiebeelden.

In dit hoofdstuk wordt Motion Vector-based Iterative Technique (MoVIT) voorgesteld. Dit algoritme reconstrueert het object op elke individuele tijdspanne, waarbij ook de projecties van naburige tijdsspannes in rekening worden gebracht. Er wordt aangetoond dat deze strategie de balans tussen de rotatiesnelheid en de signaal-ruisverhouding verbetert.

Het reconstructiekader is op zowel numerieke simulaties en op 4D X-stralen CT datasets van polyurethaanschuim onder compressie getest. De resultaten tonen aan dat de beelden verkregen met het MOVIT algoritme een significant hogere signaal-ruisverhouding hebben in vergelijking met de beelden van conventionele reconstructiealgoritmes.

Hoofdstuk 5 – Besluit

In dit hoofdstuk worden algemene conclusies getrokken over het gepresenteerde werk.

Summary

X-ray computed tomography (CT) is a powerful non-destructive imaging technique to visualize the interior of an object. Based on several X-ray images acquired from different directions, a 3D model of the object is calculated with a reconstruction algorithm. Due to its powerful characteristics, X-ray CT is frequently used in numerous applications, such as medical, biomedical and industrial imaging.

In order to obtain accurate visualisations of the interior of the object, the imaging process and the object itself should be correctly modelled. Typical CT algorithms model these processes as stationary. Unfortunately, this stationarity assumption is often not met. If the dynamics are non-negligible, failure to model them leads to artefacts in the calculated reconstruction images. Therefore, several dynamics will be modelled in this work and included in a range of CT algorithms in order to eliminate or reduce these artefacts.

Chapter 2 will focus on the dynamics of the imaging process. More specifically, a normalization algorithm to correct for the incoming beam variations during the acquisition of X-ray images will be proposed. These intensity variations are often encountered in synchrotron light sources and result in systematic errors in the intensity normalization.

In the subsequent chapters, the focus changes to dynamic computed tomography. During the acquisition of a dynamic tomographic scan, the object is no longer assumed to be stationary. Due to these dynamics we are faced with two major challenges: Firstly, the deformation causes deformation artefacts which blur the reconstructed images and can cause doubling of certain structures. Secondly, the experimenter is often interested in the dynamics of the process, in addition to the 3D model of the object itself. Therefore the sample should be visualised with a sufficiently high temporal resolution, which is not straight forward with the slow acquisition times of CT. In order to overcome these challenges, two algorithms will be proposed: an affine deformation correction algorithm (Chapter 3) and a 4D-CT reconstruction framework (Chapter 4).

In what follows, the chapters of this thesis are summarized.

Chapter 1 – Introduction

This chapter introduces the reader to the basics of X-ray imaging, computed tomography and dynamic computed tomography. This knowledge will be frequently used in the following chapters.

Chapter 2 – Dynamic intensity normalization

In this chapter, an advanced projection normalisation technique is introduced that takes into account the dynamics of the X-ray imaging system. In CT, it is common practice to normalize the acquired projection data with averaged flat fields (X-ray images taken without the object) taken prior to the scan. Unfortunately, in synchrotron light sources the flat fields are often far from stationary due to source instabilities, vibrating beamline components such as the monochromator, time varying detector properties, or other confounding factors. These dynamics result in significant systematic errors in intensity normalization.

In this chapter, an efficient method is proposed to account for dynamically varying flat fields. Through principal component analysis of a set of flat fields, eigen flat fields are computed. A linear combination of the most important eigen flat fields is then used to individually normalize each X-ray projection.

Experiments show that the proposed dynamic flat field correction leads to a substantial reduction of systematic errors in projection intensity normalization compared to conventional flat field correction.

Chapter 3 – Affine deformation estimation and correction in cone beam computed tomography

In micro-CT, long scan times, in the order of hours, are common to obtain a sufficiently high SNR and spatial resolution due to the low X-ray flux of the scanners. Hence, micro-CT experiments bear a high risk of sample motion and deformation during the acquisition. Tomographic reconstruction algorithms that do not account for this suffer from motion artefacts in the reconstructed images such as blurring or streaking.

To remedy these artefacts, we introduce an efficient algorithm to estimate and correct for global affine deformations directly on the cone beam projections. To this purpose a relationship between affine transformations and the cone beam transform is proved and used. The deformation parameters that describe deformation perpendicular to the projection direction are estimated for each projection by minimizing a plane-based inconsistency criterion. The criterion compares each projection of the main scan with all projections of a fast reference scan, which is acquired prior or posterior to the main scan.

Experiments with simulated and experimental data show that the proposed affine deformation estimation method is able to substantially reduce motion artefacts in cone beam CT images.

Chapter 4 – MoVIT: A tomographic reconstruction framework for 4D-CT

4D computed tomography (4D-CT) aims to visualise the temporal dynamics of a 3D sample with a sufficiently high temporal and spatial resolution. Successive time frames are typically obtained by sequential scanning, followed by independent reconstruction of each 3D dataset. Such an approach requires a large number of projections for each scan to obtain images with sufficient quality (in terms of artefacts and SNR). Hence, there is a clear trade-off between the rotation speed of the gantry (i.e. time resolution) and the quality of the reconstructed images.

In this chapter, the Motion Vector-based Iterative Technique (MoVIT) is introduced which reconstructs a particular time frame by including the projections of neighbouring time frames as well. It is shown that such a strategy improves the trade-off between the rotation speed and the SNR.

The framework is tested on both numerical simulations and on 4D X-ray CT datasets of polyurethane foam under compression. Results show that reconstructions obtained with MoVIT have a significantly higher SNR compared to the SNR of conventional 4D reconstructions.

Chapter 5 – Conclusions

In this chapter general conclusions are drawn from the work presented in this thesis.

1

Introduction

Contents

1.1 X-ray imaging 3
   1.1.1 X-ray generation 3
   1.1.2 X-ray matter interaction 5
   1.1.3 X-ray detection 8
   1.1.4 Projection geometries 8
1.2 Computed tomography 8
   1.2.1 Analytical reconstruction algorithms 10
   1.2.2 Algebraic reconstruction algorithms 16
   1.2.3 Statistical reconstruction algorithms 21
1.3 Dynamic computed tomography 21
   1.3.1 Dynamic tomographic model 21
   1.3.2 4D-CT 22
   1.3.3 Deformation correction 24
   1.3.4 Applications 24
References 26

This chapter introduces the basic concepts of X-ray imaging and computed tomography (CT). Computed tomography is a non-invasive technique that allows visualizing the interior of a stationary object. In order to do this, several X-ray images (typically called projections or radiographs) from different angles around the object are acquired. Afterwards, reconstruction images of the object are calculated based on the acquired X-ray projections. The CT process is conceptually visualised in Figure 1.1.

The acquisition process of an X-ray image will be described in more detail in Section 1.1. In Section 1.2, the theory behind the reconstruction algorithms will be explained. In the last section, dynamic computed tomography (Section 1.3), we no longer assume that the inspected object is stationary. Therefore the dynamic behaviour is modelled in the image reconstruction algorithm.

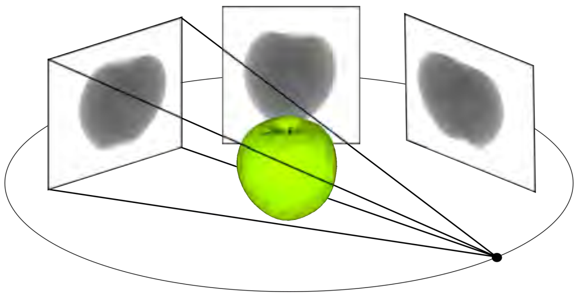

(a) During the acquisition several X-ray images are acquired from different angles.

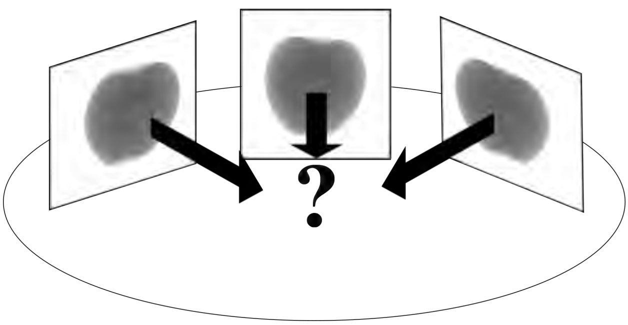

(b) A reconstruction algorithms calculates the 3D object based on the acquired projections.

Figure 1.1: Conceptual visualization of the CT scan of an apple.

This chapter will only give a concise description of the mentioned concepts. A more detailed description of computed tomography can be found in [1, 2].

1.1 X-ray imaging

In this section the necessary equipment to acquire an X-ray image and the underlying physics will be discussed. Firstly, an X-ray source, generating the X-rays, is needed. The types of sources and their characteristics will be discussed in Section 1.1.1. Secondly, the incoming X-ray beam will interact with an object resulting in an altered outgoing beam. This process is discussed in more detail in Section 1.1.2. Finally, the intensity of the outgoing beam is measured with a detector, as discussed in Section 1.1.3.

X-ray projections can be acquired using different scanners which have their own acquisition geometry. The main geometry types are described in Section 1.1.4.

1.1.1 X-ray generation

In medical imaging and in laboratory-based micro-CT systems the generation of X-rays is typically achieved with an *X-ray tube* (see Figure 1.2a). In an X-ray tube, a filament is heated to approximately $2400\,K$, as such the binding energy of the electrons to the metal of the filament is overcome and electrons are emitted [1]. These electrons are then accelerated by a high voltage ($10\,kV < U_a < 300\,kV$) towards a tungsten anode. With the entry of the electrons in the anode the electrons interact with the atoms of the anode with the production of a wide spectrum of X-rays as a result.

In Figure 1.2b a typical X-ray tube spectrum of the polychromatic beam is shown, on which two distinct features can be observed:

1. A broad continuous spectrum can be observed which is caused by a process known as *bremsstrahlung*. As the electrons enter the surface of the anode, they are decelerated by the Coulomb fields of the surrounding atoms. The maximum energy (E_{max}) of the photons can be determined by $E_{max} = eU_a$, where $e = 1,602 \cdot 10^{-19}\,C$ is the charge of an electron. However, typically several photons are created during the deceleration of a single electron. As a result, most photons will have a lower energy than E_{max} and will be distributed over a wide spectrum of energies, resulting in a polychromatic X-ray beam. The intensity of the X-rays generated with this process decrease linearly with increasing energy [1].

2. Sharp peaks can be observed in the spectrum. These are caused by *characteristic X-ray emission*: if an electron interacts with an inner electron of an

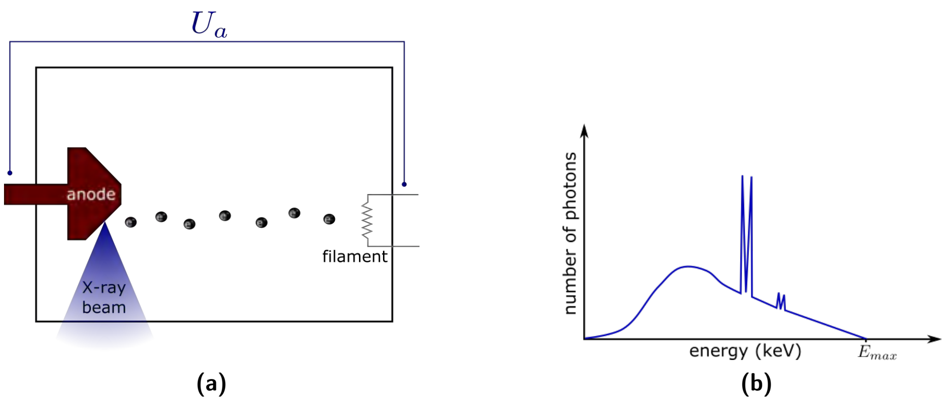

Figure 1.2: (a) Conceptual visualisation of an X-ray tube. (b)Conceptual visualisation of a typical X-ray spectrum of a beam generated with an X-ray tube.

atom of the anode material, the inner electron can be ejected. This vacancy will be filled by an electron of a higher shell, which will produce a photon with an energy equal to the energy difference between the two shells. Since the energy difference between these energy shells is fixed, this process results into distinct peaks in the X-ray spectra.

The spot where the X-rays are created on the anode is called the focal spot. Ideally, this spot should be a point source. Since this is in practice not achievable manufacturers of X-ray tubes try to minimize the size of the focal spot. Failure to do so results in penumbra blurring, resulting in a loss of spatial resolution of the X-ray images. This effect is illustrated in Figure 1.3.

To guide the electrons to a small focal spot, their trajectory is controlled by electron optics. However, since 99% of the kinetic energy of the incoming electrons is transferred into heat during the interaction with the anode, serious heating problems occur. To prevent melting, the heat can be distributed over a larger area of the anode by the use of rotating anodes. These rotating anode tubes are often used in medical scanners as they are capable of producing high brilliance X-ray bundles. However, in micro focus X-ray tubes (with a typical focal spot size of $1 - 50\,\mu m$) these rotating anodes are typically not used due to insufficient stability and thus a loss of resolution. As a result, micro focus tubes can only be operated at relatively low power [3]. To remedy this, new X-ray sources have been introduced with a liquid metal jet anode, resulting in a better heat dissipation and thus enabling higher power micro focus X-ray tubes [4].

Alternatively, *synchrotron light sources* can be used to produce X-rays [5]. In these facilities, electrons are accelerated to nearly the speed of light and are

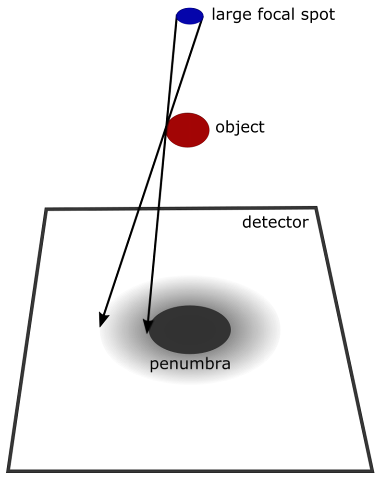

Figure 1.3: Illustration of the effect of a large focal spot on the acquired X-ray image.

kept circulating in a storage ring. At certain places the electron beam is guided through insertion devices such as wigglers. These manipulate the direction of the beam, resulting in the production of X-rays which are guided to a wide range of work stations, often called beamlines. Some beamlines are especially equipped with instrumentation to acquire tomographic X-ray scans. In contrast to X-ray tubes, synchrotron light sources produce very high intensity X-ray beams. This allows acquiring high signal-to-noise ratio (SNR) datasets and/or very fast imaging with similar resolution as micro-CT scanners. Due to their high intensity beams monochromators can be used, resulting in a monochrome X-ray beam. While these monochromators drastically reduce the X-ray flux they also eliminate beam hardening artefacts (see Section 1.1.2). More details about the exact build-up of a tomographic beamline can be found in [6].

Synchrotron light sources can be found all over the world. A few examples are the ESRF (France), Diamond Light Source (United Kingdom), SLS (Switzerland), Max IV (Sweden), Elettra (Italy), APS (USA) and the Australian Synchrotron (Australia). In Figure 1.4 an aerial view the ESRF is shown to give an impression of the size of a typical synchrotron light source.

1.1.2 X-ray matter interaction

X-rays are primarily known for their penetrating abilities through optically opaque materials. However, imaging of the inside of an object would be impossible if the X-rays simply travelled through the object without interacting with it. Indeed, while the X-ray beam travels through the sample absorption and scattering of the beam

Figure 1.4: An aerial view of the ESRF, a synchrotron light source near Grenoble, France.

occurs, resulting in an exponential reduction of the amount of photons. While the underlying physical interactions are Rayleigh scattering, Compton scattering, photoelectric absorption and pair production, a much simpler model, the *Beer-Lambert law*, is often used to describe the attenuation of a monochromatic X-ray beam. The Beer-Lambert law is given by following formula:

$$I = I_0 e^{-\int \mu(x)\,\mathrm{d}x}, \tag{1.1}$$

where I_0 is the incoming intensity, I the measured intensity, and $\mu(x)$ the spatially dependent attenuation coefficients. Note that, the measured intensity contains information about a line integral of the attenuation coefficients and thus projects all information of a line in the volume on a single detector pixel. Due to this property the acquired images are called projection images.

In practice, one is especially interested in the spatial variation of the attenuation values. Therefore, the acquired projection data is converted to the projection integral (p):

$$p = \int \mu(x)\,\mathrm{d}x = -\ln\left(\frac{I}{I_0}\right). \tag{1.2}$$

The division of the measured intensity with the incoming intensity is often referred to as *flat field correction* or *normalisation*. The negative logarithm is known as the *log correction* of the projection data.

In practice the incoming intensity is measured by acquiring several projections without object in the beam before and/or after the scan, also known as flat field or white field images. The mean flat field is then calculated to reduce the variance of the noise as much as possible. Then Eq. 1.2 is pixel-wise executed with the mean flat field as the incoming intensity.

The Beer-Lambert law (see Eq. 1.1) is flawed for polychromatic radiation.

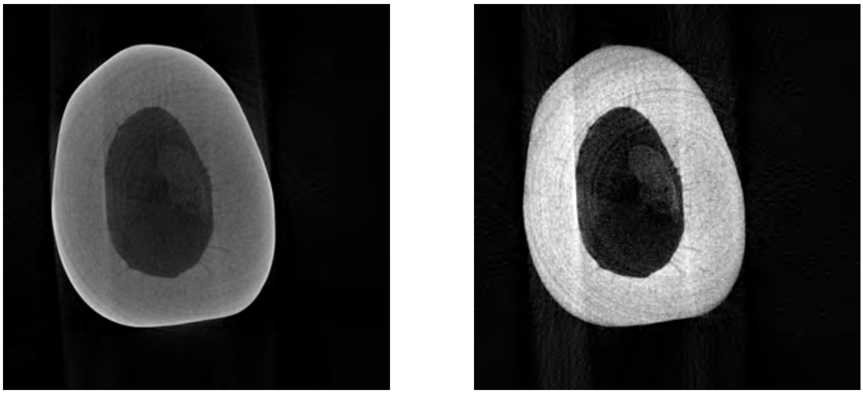

(a) (b)

Figure 1.5: Reconstruction images of the femur of a rat (a) without beam hardening correction (b) and with beam hardening correction (linearization approach as described in [7]). This scan was acquired without hardware filtering of the beam to visualise the cupping effect more clearly. This dataset was acquired with a Skyscan 1072 micro CT scanner.

Due to the energy dependency of the attenuation coefficients ($\mu(x, E)$) the Beer-Lambert law should be generalized to:

$$I = \int_0^{E_{max}} I_0(E) e^{-\int \mu(x,E)\,\mathrm{d}x}\,\mathrm{d}E, \tag{1.3}$$

However, this model is seldom used in practice. Neglecting the energy dependency causes cupping effects, also known as beam hardening artefacts, in CT reconstruction images as can be seen in Figure 1.5b. In this figure a reconstruction image of the femur of a rat is shown without and with a software-based beam hardening correction [7]. Notice that the border of the bone is much brighter on the reconstruction image without correction although the attenuation coefficient of the material is similar to that of the rest of the bone.

Another flaw of the flat field procedure (see Eq. 1.2) is that it assumes the incoming beam to be stationary. However, this is often not the case in synchrotron light sources (see Section 1.1.1) due to a number of confounding factors. The conventional flat field procedure does not take this dynamic behaviour into account which results in artefacts in the normalised projections if the dynamics are non-negligible. Therefore, a dynamic flat field correction procedure was developed, which is described in Chapter 2.

1.1.3 X-ray detection

Historically, a film containing silver bromide was used to acquire X-ray images. These days, however, silver bromide films have become obsolete and are replaced by semiconductor flat panel detectors. These can be split in two categories: direct and indirect detectors. Direct detectors convert the incoming X-ray beam directly into an electric signal. However, direct detectors are until now rarely used in imaging. The second, more popular and cheaper class of detectors are the indirect detectors [8, 9]. These detectors convert the X-rays to visible light with a phosphors plate also called a scintillator [1]. This visible light can then be detected with a charge-coupled device (CCD) or CMOS based camera.

Flat panel detectors are build-up out of numerous detector elements (detector pixels), arranged in multiple rows and colons. A typical detector has between 1000-4000 rows and columns and thus ranging from 1 to 16 mega pixel.

1.1.4 Projection geometries

The geometrical properties of the X-ray beam and the detector define the projection geometry. In the 2D case, parallel beam and fan beam geometries are the most common. In the parallel beam case the different rays are parallel to each other. In contrast, the rays of a fan beam originate from a single point and diverge towards the detector. In the 3D case, the same distinction can be made. On the one hand we have the parallel beam, on the other hand the cone beam geometry which is the 3D analogue of the fan beam geometry. In practice both 3D geometries are encountered. In micro-CT, the X-rays from an X-ray tube originate, approximately, from a single point. As a result, the acquisition geometry can be described with a cone beam geometry. In synchrotron light sources the X-rays travel approximately parallel to each other and thus have to be described with a parallel beam geometry. All of the mentioned geometries are visualised in Figure 1.6.

1.2 Computed tomography

In X-ray imaging, projection images of the studied object can be acquired. However, valuable spatial information about the object is lost in the process since the 3D spatial information is projected on a single 2D detector. Computed tomography aims to obtain this 3D information by acquiring multiple X-ray projections at different angles around the object.

CT scanners can be split up in different classes. The most well-known class of CT scanners is the medical CT scanner (see Figure 1.7a), which can be found in almost every hospital. However, other types of scanners can be found in the research and industrial environment. In biomedical research, in vivo micro CT

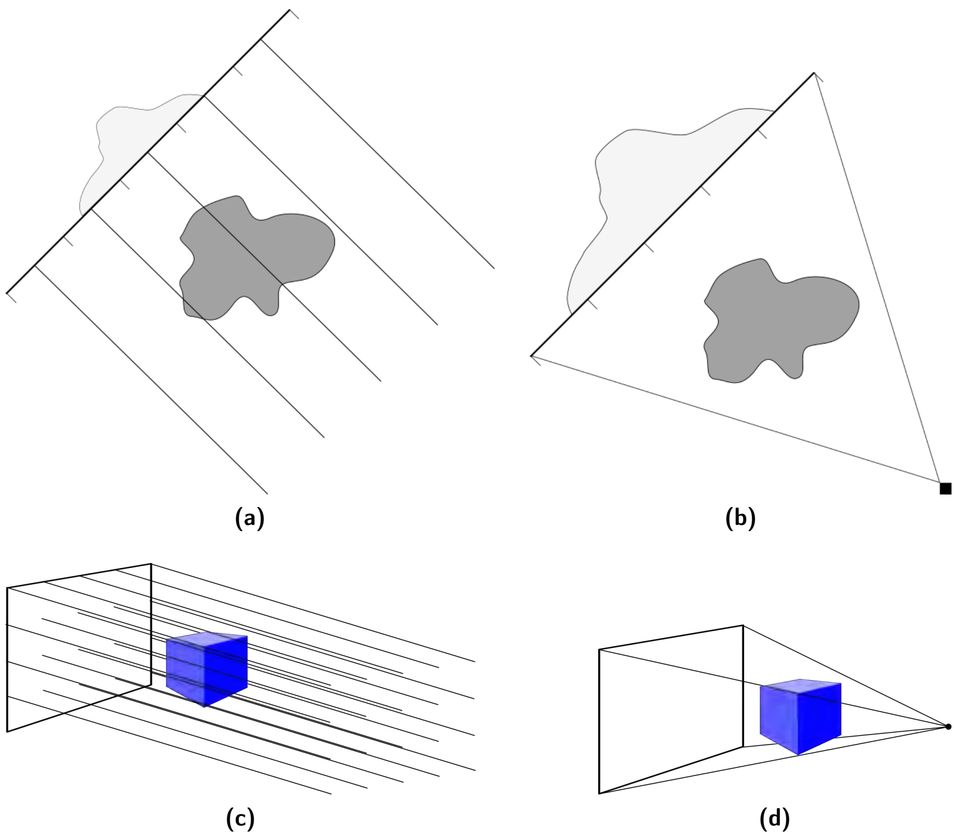

Figure 1.6: (a) 2D parallel beam projection geometry. (b) 2D fan beam projection geometry. (c) 3D parallel beam projection geometry. (d) 3D cone beam projection geometry.

(a) Medical scanner: Siemens Somatom

(b) Bio-medical scanner: Bruker micro-CT SkyScan 1276

(c) Micro-CT scanner: Bruker micro-CT SkyScan 1272

Figure 1.7: Examples of different types of CT scanners.

scanners (see Figure 1.7b) provide valuable information about the interior of small animals. On the other hand micro-CT scanners (see Figure 1.7c) can also be used to study materials with high resolution ($> 1\,\mu m$).

The projections acquired by these CT scanners are then entered into a reconstruction algorithm which recovers the spatial distribution of the attenuation coefficients. Reconstruction algorithms can be split up in three main groups: analytic (Section 1.2.1), algebraic (Section 1.2.2) and statistical (Section 1.2.3) reconstruction algorithms.

1.2.1 Analytical reconstruction algorithms

In the first section (Section 1.2.1.1) the Radon transform is introduced. This transform describes the 2D forward problem, in other words, it analytically approximates the acquisition process. Additionally, the 3D Radon transform is explained. While this transform does not directly model the forward problem in 3D, it is an important transform on which several analytic reconstruction algorithms are based. Furthermore, some 2D analytic reconstruction algorithms are explained in Section 1.2.1.2 and Section 1.2.1.3. Afterwards, some 3D analytic reconstruction algorithms will be discussed. Lastly, recent advancements in the field of analytic reconstruction techniques are mentioned.

1.2.1.1 Radon transform

The 2D Radon transform, introduced by Johann Radon in 1917, formalizes the projection process in a 2D parallel beam geometry. A line L in 2D space can be described with its signed distance r from the origin and an angle θ:

$$L = \{\boldsymbol{x} \in \mathbb{R}^2 | \boldsymbol{x} \cdot \boldsymbol{n}_\xi = r\}, \tag{1.4}$$

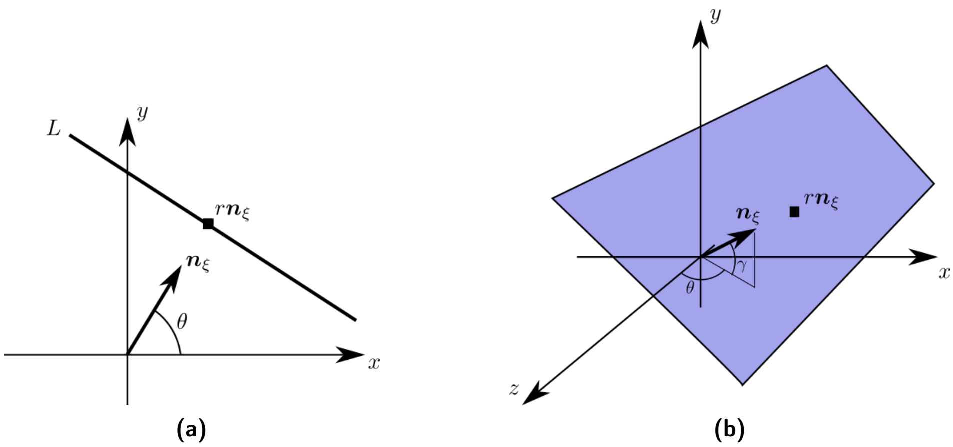

Figure 1.8: Schematic overview of the geometry of the (a) 2D Radon transform and (b) 3D Radon transform.

where $\boldsymbol{n}_\xi = [\cos(\theta), \sin(\theta)]^T$ (see Figure 1.8a).

The line integral over L of a 2D function $f(\boldsymbol{x})$ can be calculated with:

$$p_\theta(r) = \int_{L(r,\theta)} \mu(\boldsymbol{x})\,\mathrm{d}\boldsymbol{x}. \tag{1.5}$$

An analogue form of this formula that is often used is:

$$p_\theta(r) = \int_{\mathbb{R}^2} \mu(\boldsymbol{x})\delta\left(\boldsymbol{n}_\xi \cdot \boldsymbol{x} - r\right)\,\mathrm{d}\boldsymbol{x}, \tag{1.6}$$

where $\delta(.)$ is the Dirac delta function.

The Radon transform $\mathcal{R}_2$ is the transformation that maps the function $\mu(\boldsymbol{x})$ to the complete set of projection values [10, 11]:

$$\mu(\boldsymbol{x}) \overset{\mathcal{R}_2}{\leftrightarrow} \{p_\theta(r)|\theta \in [0, 2\pi[, r \in \mathbb{R}\} \tag{1.7}$$

This equation implies that $(\mathcal{R}_2\mu)(\theta, r) = p_\theta(r)$. To $p_\theta(r)$ is often referred to as the *sinogram* or the *projection data*. As an example, the Shepp-Logan phantom [12] and its sinogram is shown in Figure 1.9.

While the 2D Radon transform calculates the line integral of a 2D function, the 3D transform calculates integrals over planes. Similar to a line in 2D, a plane in 3D can be described with a unit normal vector $\boldsymbol{n}_\xi$ and the signed distance r to

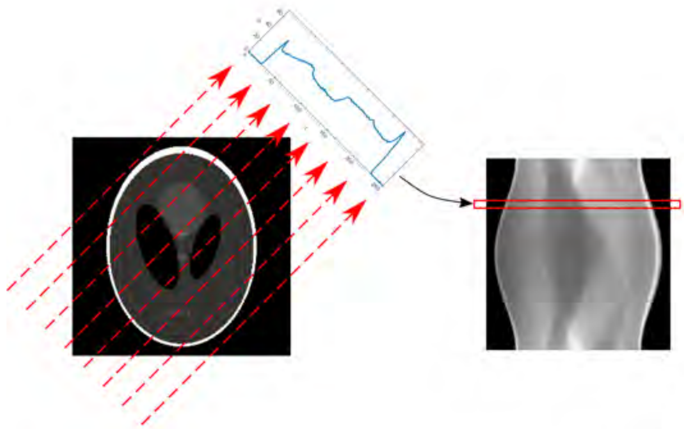

Figure 1.9: The Shepp-Logan phantom [12] (left) and its 2D Radon transform (right). Furthermore, the projection process for $\theta = 45^\circ$ is shown.

the origin:

$$A = \{\boldsymbol{x} \in \mathbb{R}^3 | \boldsymbol{x} \cdot \boldsymbol{n}_\xi = r\}, \tag{1.8}$$

where $\boldsymbol{n}_\xi = [\cos(\gamma)\sin(\theta),\, \sin(\gamma)\sin(\theta),\, \cos(\theta)]^T$ (see Figure 1.8b). Thus the 3D Radon transform $\mathcal{R}_3$ calculates the complete set of plane integrals of a function in $\mathbb{R}^3$

$$\mu(\boldsymbol{x}) \overset{\mathcal{R}_3}{\leftrightarrow} \{p_{\theta,\phi}(r) | \theta \in [0, 2\pi[, \phi \in [0, \pi], r \in \mathbb{R}\}, \tag{1.9}$$

with

$$p_{\theta,\gamma}(r) = \int_{A(r,\theta,\gamma)} \mu(\boldsymbol{x})\, \mathrm{d}\boldsymbol{x}. \tag{1.10}$$

Note that the 3D Radon transform does not integrate over line integrals in $\mathbb{R}^3$ and thus does not model the projection process in 3D. However, the 3D Radon transform is an important transform in CT and is the basis of several 3D reconstruction algorithms (see Section 1.2.1.4). Furthermore, the 3D Radon transform plays an important role in Chapter 3 since it can be used as the basis of a plane based consistency condition.

1.2.1.2 Back projection

While the 2D Radon transform is an important result, in practice the inverse problem has to be solved. Based on the projection images the spatially dependent attenuation coefficients $\mu(\boldsymbol{x})$ should be obtained. In order to obtain these a simple back projection can be performed. This procedures smears back the acquired

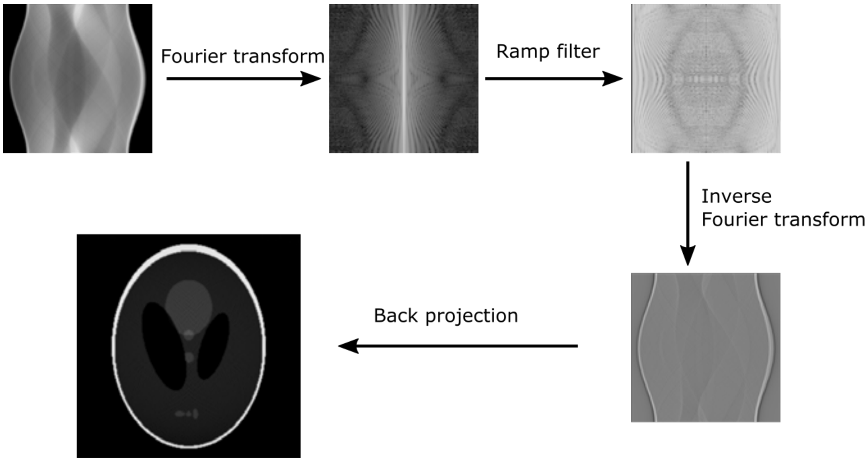

Figure 1.10: The different steps of the FBP algorithm.

projection values in the direction from which the radiation came. Mathematically, this process can be described as:

$$g(\boldsymbol{x}) = \int_0^\pi p_\theta(\boldsymbol{x} \cdot \boldsymbol{n}_\xi)\,\mathrm{d}\theta. \tag{1.11}$$

Although this simple formula seems to reverse the whole process, it results in a blurry reconstruction image. While the back projection is indeed not the inverse of the Radon transform, it is an important part of analytic (Section 1.2.1) as well as algebraic reconstruction algorithms (Section 1.2.2).

1.2.1.3 Filtered back projection

As mentioned in the previous section, a simple back projection does not result in a satisfying solution. However it can be proven, using the Fourier slice theorem, that one can achieve the correct result by first applying a high pass filter on the projection data. This method is called Filtered Back Projection (FBP). Mathematically, it is given by following formula:

$$f(\boldsymbol{x}) = \int_0^\pi \int_{-\infty}^\infty |q| P_\theta(q) e^{2\pi i q \boldsymbol{x} \cdot \boldsymbol{n}_\xi}\,\mathrm{d}q\,\mathrm{d}\theta, \tag{1.12}$$

where $P_\theta(q)$ is the Fourier transform of $p_\theta(r)$. Eq. 1.12 can be implemented as follows:

1. The Fourier transform of the acquired sinogram is calculated, resulting in

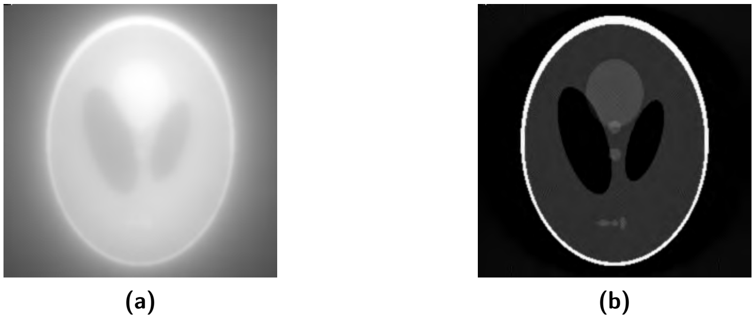

Figure 1.11: Reconstruction of the Shepp-Logan phantom (see Figure 1.9) with (a) simple back projection and (b) filtered back projection.

$P_\theta(q)$.

2. The Fourier transformed sinogram is multiplied with *the ramp filter*, $|q|$.
3. The inverse Fourier transform of $|q|P_\theta(q)$ is calculated, resulting in a high pass filtered sinogram.
4. A simple back projection (see Section 1.2.1.2) of the filtered sinogram is performed.

The different steps are also shown in Figure 1.10.

A comparison between the results of a simple back projection and a filtered back projection are shown in Figure 1.11. Clearly, the FBP reconstruction image is sharper than the simple back projection image.

The FBP algorithm has multiple advantages compared to other reconstruction algorithms: Firstly, the FBP algorithm is fast. This has contributed to the popularity of FBP-like reconstruction algorithms. Secondly, the algorithm is theoretically exact. However, the FBP algorithm is only exact if *all* the projection data is acquired. In practice this is never the case and especially with a low number of projections the algorithm falls short. Another drawback is that it is not very flexible. For example, adding prior knowledge to the algorithm is not straightforward. Additionally, the FBP algorithm is only valid for a parallel beam acquisition with a circular trajectory of the gantry. For other geometries an appropriate algorithm should be used or derived.

Datasets acquired with a fan beam geometry can thus not be entered directly into the FBP algorithm. In order to reconstruct these images, one can rebin the projections to parallel beam projections or use an analytic reconstruction algorithm that is specially adapted to the fan beam geometry [1, 2]

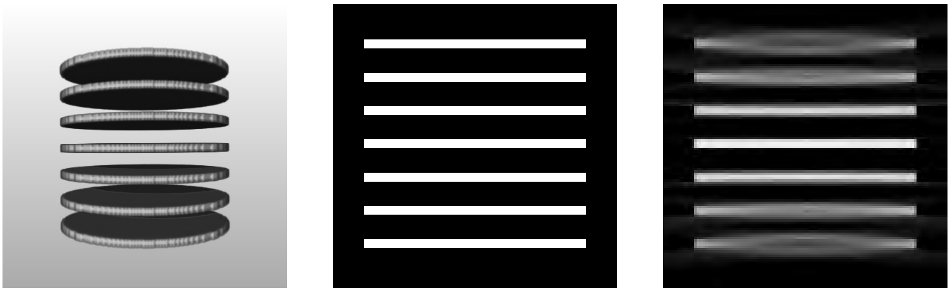

(a) (b) (c)

Figure 1.12: The Defrise phantom consists out of several horizontal disks and is designed to visualise cone beam artefacts. (a) Rendering of the Defrise phantom. (b) Vertical cross-section through the phantom. (c) Vertical cross-section through the FDK reconstruction calculated with cone beam projections acquired on a circular source trajectory.

1.2.1.4 3D analytic reconstruction methods

Reconstruction with 3D parallel beam data with a circular trajectory is a straight forward extension of the 2D case, since every cross-section can be described as a 2D reconstruction. However, cone beam projections complicate the reconstruction process. The Tuy-Smith sufficiency condition states that an exact cone beam reconstruction (see Section 1.1.4) can be calculated if all the planes intersecting the object intersect the X-ray source trajectory at least once [13]. If this is the case, reconstruction algorithms based on the general three-dimensional inverse Radon transform can be used such as the ones introduced by Gangreat and Defrise [14, 15]. However, if a cone beam dataset is acquired with a circular source trajectory the Tuy-Smith condition is not met. While this clearly means that an exact reconstruction cannot be obtained, good approximations can be calculated. The most frequently used method for this purpose is the *Feldkamp-Davis-Kress (FDK) algorithm* [16].

Since the reconstructions calculated with cone beam projections with a circular trajectory are not exact, they are susceptible to cone beam artefacts. These artefacts are most pronounced if a plane perpendicular to the rotation axis and far from the central slice is imaged. The Defrise phantom is especially designed to visualise the effect of these artefacts as shown in Figure 1.12. Here it can be clearly seen that the central disk is well reconstructed. However, disks further from the center are strongly blurred.

For datasets acquired with a spiral source trajectory, other reconstruction algorithms are available [17].

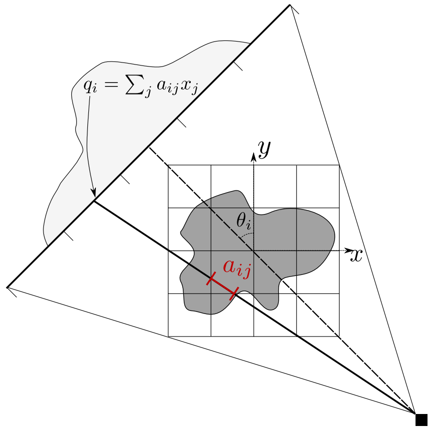

Figure 1.13: Schematic illustration of the algebraic model.

1.2.1.5 Other analytic reconstruction methods

As mentioned before, the analytic methods are quite hard to adapt to prior knowledge. However, recently some methods were published to include prior knowledge in the filter, for example, by training the filter with an artificial neural network [18?]. Another method is able to calculate a filter such that the resulting reconstruction images closely approximate the results of the SIRT algorithm (see Section 1.2.2) [19].

1.2.2 Algebraic reconstruction algorithms

In algebraic reconstruction methods, the acquisition process is modelled with a linear system of equations:

$$\boldsymbol{A}\boldsymbol{x} = \boldsymbol{q}, \tag{1.13}$$

where $\boldsymbol{x} = (x_i) \in \mathbb{R}^N$ is a vector representing a discretized version of the scanned object, $\boldsymbol{q} = (q_i) \in \mathbb{R}^M$ are the simulated projection values and $\boldsymbol{A} = (a_{ij}) \in \mathbb{R}^{M \times N}$ is a matrix of which the entries a_{ij} represent the contribution of voxel value x_j to the projection value q_i. This concept is schematically visualised in Figure 1.13.

In CT one wants to solve $\boldsymbol{A}\boldsymbol{x} = \boldsymbol{p}$ for $\boldsymbol{x}$, with $\boldsymbol{p} = (p_i) \in \mathbb{R}^M$. However, the inverse of $\boldsymbol{A}$ does in general not exist. Nevertheless, a closed form expression of the least-squares solution does exist:

$$\boldsymbol{x}_{LS} = \arg\min_{\boldsymbol{x}} \|\boldsymbol{A}\boldsymbol{x} - \boldsymbol{p}\|_2^2 = (\boldsymbol{A}^T\boldsymbol{A})^{-1}\boldsymbol{A}^T\boldsymbol{p}, \tag{1.14}$$

where $\|\boldsymbol{y}\|_2^2 = \boldsymbol{y}^T\boldsymbol{y}$ is the squared 2-norm. Unfortunately, this is infeasible to calculate on modern computers, even for moderate size reconstruction problems. Therefore, several iterative methods were developed to find approximate solutions of $\boldsymbol{Ax} = \boldsymbol{p}$, such as the Algebraic Reconstruction Technique (ART), Simultaneous Algebraic Reconstruction Technique (SART), Simultaneous Iterative Reconstruction Technique (SIRT), Krylov subspace methods and Conjugate Gradient Least Squares (CGLS) [2, 20, 21].

In Section 1.2.2.1 the SIRT algorithm will be discussed in more detail. Furthermore, some advanced algebraic reconstruction algorithms (Section 1.2.2.2) and the implementation of algebraic methods in this thesis (Section 1.2.2.3) will be discussed.

1.2.2.1 Simultaneous Iterative Reconstruction Technique

The SIRT algorithm solves the weighted least-squares optimization problem:

$$\arg\min_{\boldsymbol{x}} \|\boldsymbol{Ax} - \boldsymbol{p}\|_{\boldsymbol{R}}, \tag{1.15}$$

where $\|\boldsymbol{Ax} - \boldsymbol{p}\|_{\boldsymbol{R}} = (\boldsymbol{Ax} - \boldsymbol{p})^T \boldsymbol{R}(\boldsymbol{Ax} - \boldsymbol{p})$ and $\boldsymbol{R} = (r_{kl}) \in \mathbb{R}^{M \times M}$ is a diagonal matrix with $r_{kk} = \left(\sum_l a_{kl}\right)^{-1}$, the row sums of the matrix $\boldsymbol{A}$ [22]. The following iterative formula is known to converge to the weighted least-squares minimum:

$$\boldsymbol{x}^k = \boldsymbol{x}^{k-1} + \boldsymbol{C}\boldsymbol{A}^T \boldsymbol{R}(\boldsymbol{p} - \boldsymbol{A}\boldsymbol{x}^{k-1}), \tag{1.16}$$

where $\boldsymbol{C} = (c_{kl}) \in \mathbb{R}^{N \times N}$ is a diagonal matrix with $c_{ll} = \left(\sum_k a_{kl}\right)^{-1}$, the column sums of the matrix $\boldsymbol{A}$. The different steps of the SIRT algorithm are visualised in Figure 1.14. Firstly, projections of the current reconstruction image are simulated and compared to the acquired projections. This result is called the projection difference. Subsequently, the projection difference is weighted with the matrix $\boldsymbol{R}$, back projected and finally weighted with the matrix $\boldsymbol{C}$, resulting in the SIRT update that is added to the current reconstruction. These steps are repeated until a stopping criterion is fulfilled. In practice, this stopping criterion is most frequently a maximum number of iterations.

The SIRT algorithm can also be written explicitly for each component of $\boldsymbol{x}$:

$$x_j^k = x_j^{k-1} + \left(\sum_i a_{ij}\right)^{-1} \sum_i \left(\frac{a_{ij}(p_i - \sum_h a_{ih} x_h^{k-1})}{\sum_h a_{ih}}\right). \tag{1.17}$$

Note that, the SIRT algorithm can be interpreted as a maximum likelihood algorithm. If the projections are assumed to contain independent Gaussian noise,

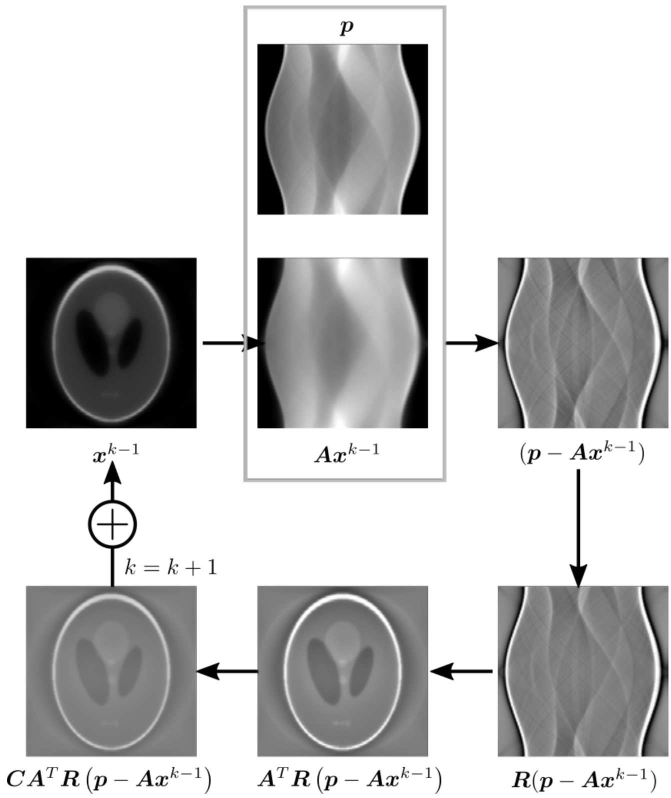

Figure 1.14: The different steps of the SIRT algorithm applied on the Shepp-Logan phantom.

the likelihood function can be formulated as follows:

$$P(\boldsymbol{x}) = Z^{-1} \prod_i e^{\frac{-\left(\sum_j a_{ij} x_j - p_i\right)^2}{2\sigma_i^2}}, \tag{1.18}$$

where Z is a normalization constant and σ_i the standard deviation of the i'th projection pixel. This results in following maximum log-likelihood problem:

$$\arg\max_{\boldsymbol{x}} \sum_i \frac{-\left(\sum_j a_{ij} x_j - p_i\right)^2}{2\sigma_i^2}. \tag{1.19}$$

This equation can easily be rewritten in following matrix form:

$$\arg\min_{\boldsymbol{x}} (\boldsymbol{Ax} - \boldsymbol{p})^T \boldsymbol{\Sigma} (\boldsymbol{Ax} - \boldsymbol{p}), \tag{1.20}$$

where $\Sigma \in \mathbb{R}^{M \times M}$ is a diagonal matrix where $(\Sigma)_{ii} = \sigma_i^{-2}$. Notice the resemblance between Eq. 1.20 and the SIRT objective function: $\|\boldsymbol{Ax} - \boldsymbol{p}\|_{\boldsymbol{R}}$, which are equivalent if we assume $\sigma_k^2 = \sum_l a_{kl}$. This result reveals that SIRT assumes that projections values are corrupted with independent Gaussian noise and that rays with a larger intersection with the reconstruction volume have a larger noise variation.

The exact solution of SIRT, $\arg\min_{\boldsymbol{x}} \|\boldsymbol{Ax} - \boldsymbol{p}\|_{\boldsymbol{R}}$, is known to be sensitive to noise. However, since the algebraic methods converge relatively fast to a good approximation, which is not as sensitive to noise, of the exact solution the number of iterations can be regarded as a regularizing parameter [23]. This phenomena, known as semi-convergence, clarifies why reconstructions with fewer iterations contain typically less noise (and small details) than an image reconstructed with a large number of SIRT iterations. This is illustrated in Figure 1.15 with the Shepp-Logan phantom.

1.2.2.2 Advanced algebraic reconstruction algorithms

Many algebraic reconstruction algorithms are tailored in such a way that they incorporate certain forms of prior knowledge. This can be accomplished by adding a regularization term R to the objective function and/or adding extra constraints on the solution:

$$x^* = \arg\min_{\boldsymbol{x} \in \mathcal{D}} \left(\|\boldsymbol{Ax} - \boldsymbol{p}\| + \lambda R(\boldsymbol{x})\right), \tag{1.21}$$

where $\lambda > 0$ is the regularization parameter that controls the strength of the regularization and $\mathcal{D} \subset \mathbb{R}^N$ a subset of all the solutions satisfying the extra constraints. The regularization term imposes certain types of prior knowledge on the solution

(a) (b)

Figure 1.15: SIRT reconstructions of the Shepp-Logan phantom (see Figure 1.9) with (a) with 200 iterations and (b) 2000 iterations. The projections were simulated with a photon count of 20000 photons.

such as total variation and smoothness priors [24]. A popular constraint on the solution is the non-negativity constraint: $\boldsymbol{x} \in \{\boldsymbol{x} \in \mathbb{R}^N | \forall i = 1, \ldots, N : x_i \geq 0\}$. Another example is discrete tomography (such as the DART and DART-PDM algorithm) where only solutions with a discrete number (l) of (predefined) grey levels are allowed [25, 26]: $\boldsymbol{x} \in \{\tau_1, \ldots, \tau_l\}^N$. If the studied object meets these requirements, the object can be reconstructed with significantly lower number of projections. Other algorithms assume a porous material [27] or partially discrete objects [28]. Another advantage of the algebraic reconstruction methods is that one can model the physical acquisition process more accurately. For example, one can model a continuously rotating gantry, instead of a step-and-shoot protocol [29].

1.2.2.3 Implementation

Algebraic reconstruction algorithms are known for their high computational and memory demands. Storing the full projection matrix $\boldsymbol{A}$ into memory is only feasible for small tomographic problems. For example, a typical dataset with 1000 projections acquired on a 1000×1000 pixel detector and reconstructed on a $1000 \times 1000 \times 1000$ voxel grid, results in an $\boldsymbol{A}$ matrix with dimensions $10^9 \times 10^9$. While this matrix is of course mainly sparse, it still is too big to be stored in memory. Therefore the elements are calculated on-the-fly with for example Joseph's method [30]. To keep computation times reasonable, a GPU implementation is indispensable. For this purpose all forward and back projections in this thesis were performed with th *ASTRA toolbox* [31, 32, 33]. This toolbox is the result of a collaboration between the Visionlab (University of Antwerp) and the CWI (Centrum Wiskunde & Informatica) in Amsterdam and is a well-established toolbox in the tomographic community.

1.2.3 Statistical reconstruction algorithms

In Section 1.2.2 the projections are modelled as line integrals. The statistical reconstruction methods takes an alternative route. These algorithms estimate statistically the solution which matches the projections the closest, taking into account the measurement statistics. The maximum likelihood method can, for example, model the noise in X-ray projections with the Poisson distribution [1, 34]. More advanced reconstruction algorithms, such as IMPACT, model the underlying X-ray physics even closer, resulting in more accurate reconstructions [35]. However, these algorithms require accurate prior knowledge, such as the used X-ray spectrum, which is often not available. Statistical reconstruction algorithms are also typically associated with long computation times.

1.3 Dynamic computed tomography

In dynamic computed tomography, the object under investigation is no longer assumed to be stationary. In Section 1.3.1 a tomographic model for dynamic CT is introduced. This results in two different classes of dynamic CT problems: 4D-CT and deformation compensation which are discussed in Section 1.3.2 and Section 1.3.3, respectively.

1.3.1 Dynamic tomographic model

The conventional algebraic tomography model described in Section 1.2.2 assumes the scanned object to remain stationary throughout the acquisition process. This assumption is no longer valid in dynamic CT. Therefore, the standard tomographic model has to be generalized to deal with these dynamics.

A dynamic object can be represented as a time series of images $\boldsymbol{x}_r \in \mathbb{R}^N$, where $r \in \{1, \ldots, R\}$ is the time index, with R the total number of time frames. The projections of subscan r are represented by $\boldsymbol{p}_r \in \mathbb{R}^{M_r}$. The sparse matrix $\boldsymbol{A}_r \in \mathbb{R}^{M_r \times N}$ is the corresponding forward projection matrix. If the object is assumed stationary during each time frame, the acquisition of the dynamic process can be modelled as follows:

$$\begin{bmatrix} \boldsymbol{A}_1 & 0 & \cdots & 0 \\ 0 & \boldsymbol{A}_2 & & 0 \\ \vdots & & \ddots & \vdots \\ 0 & 0 & \cdots & \boldsymbol{A}_R \end{bmatrix} \begin{bmatrix} \boldsymbol{x}_1 \\ \boldsymbol{x}_2 \\ \vdots \\ \boldsymbol{x}_R \end{bmatrix} = \tilde{\boldsymbol{A}}\tilde{\boldsymbol{x}} = \tilde{\boldsymbol{p}}, \tag{1.22}$$

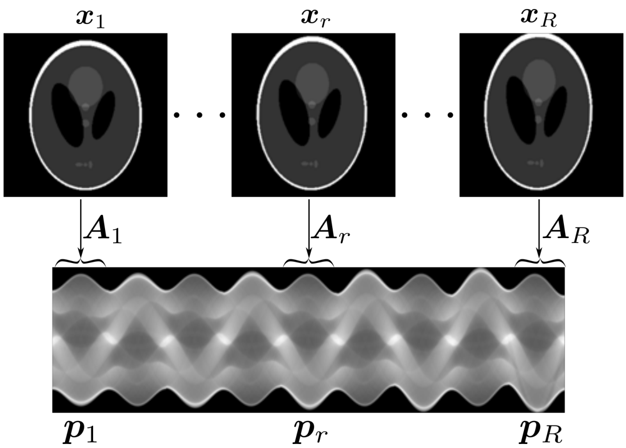

Figure 1.16: Conceptual image of the acquisition of a 4D-CT dataset. During the deformation of an object the gantry rotates continuously around the object while acquiring projection images. This results in the shown sinogram.

where $\tilde{\boldsymbol{A}}$ represents the block diagonal matrix consisting of blocks $\boldsymbol{A}_1, \ldots, \boldsymbol{A}_R$, $\tilde{\boldsymbol{x}} = (\boldsymbol{x}_1^T, \ldots, \boldsymbol{x}_R^T)^T \in \mathbb{R}^{RN}$ and $\tilde{\boldsymbol{p}} = (\boldsymbol{p}_1^T, \ldots, \boldsymbol{p}_R^T)^T \in \mathbb{R}^{\sum_{r=1}^{R} M_r}$ [36, 37].

Based on this model the dynamic tomographic problems can be split up into two categories. In the first category the time frames are CT datasets with multiple projections that cover at least an angular range of 180°, as such each time frame can theoretically be reconstructed. To this category we will refer to as *4D-CT* (see Section 1.3.2). Note that, for periodic deformation, gating methods can be applied to sort the projections in different time frames. In the second category, to which we will refer to as *deformation correction* (see Section 1.3.3), the time frames are individual projections. This means that the model allows motion in a single rotation of the gantry.

1.3.2 4D-CT

In 4D-CT we assume that motion or deformation during a single subscan (a subset of the projections with an angular range of 180° or 360°) is negligible, as discussed in Section 1.3.1.

However, due to the long acquisition time of conventional CT, two problems arise if a fast dynamic process is imaged. Firstly, the long acquisition time of a single time frame strongly limits the temporal resolution. Secondly, due the object deformation during the acquisition of a single time frame, the projections of this time frame are not consistent with each other. This results in blurry reconstructed images due to deformation artefacts. A straightforward method to avoid both problems is shortening the acquisition time of a single time frame. This can be achieved by reducing the integration time of a single projection or lowering the number of projections per time frame. A shorter integration time, however, reduces the signal-to-noise ratio (SNR) of the projection data, which in turn leads to a lower SNR in the reconstructed images. Lowering the number of projections, on the other hand, results in streaks in the reconstructed images. Mathematically this can be regarded as follows: minimizing $\|\tilde{\boldsymbol{A}}\tilde{\boldsymbol{x}} - \tilde{\boldsymbol{p}}\|$ for $\tilde{\boldsymbol{x}}$ is an ill-posed problem for a dataset with a low number of projections due to the large null space of the forward operator $\tilde{\boldsymbol{A}}$ and the noise present in the projection data. This results in reconstructions $\tilde{\boldsymbol{x}}$ which are dominated by streak artefacts and noise. As a result, the conventional workflow leads to a trade-off between the temporal resolution/deformation artefacts and low SNR/streaking artefacts in the reconstructed images.

Fortunately, the trade-off between the temporal resolution and SNR can be improved by exploiting data redundancy present in 4D-CT datasets. Since in every time frame the same, though slightly changed, object is scanned, it is beneficial to include information about other time frames into the reconstruction process [36]. This idea is the basis of the *Motion Vector-based Iterative Technique* which introduced in Chapter 3.

As explained in the previous paragraph, exploiting the connection between different time frames can be beneficial. In this framework the acquisition of redundant information should be avoided as much as possible. This can be accomplished by abandoning conventional acquisition schemes as described by Kaestner et al. [38], in particular, avoiding that the same acquisition angles are selected in every rotation. We will refer to these acquisition schemes as *interleaved projection protocols*. Two different protocols can be used: the *binary* and the *golden ratio decomposition*. In the binary decomposition, each time frame consists of a set of equidistant projections. However each time frame has a slightly shifted starting angle. As such neighbouring time frames do not acquire projections with the same projection angle. In the golden ratio acquisition scheme the source and detector rotate over a fixed angular step: $\Delta\theta = \pi\left(1+\sqrt{5}\right)/2$ radians. This acquisition scheme assures that a projection angle is never selected twice. Additionally, the golden ratio acquisition scheme is very flexible since it allows the user to select an arbitrary number of projections per time frame after the acquisition, while still using approximately equiangular projections for each time frame. As such the user can balance the temporal versus the spatial resolution after the acquisition. Unfortunately, due to the large angular step the time spent by rotating the source and detector is rather large compared to conventional acquisition schemes. This means that the golden ratio scheme is especially useful in acquisitions with long exposure times such as neutron tomography. Therefore, the golden ration scheme is hardly ever used in X-ray acquisitions.

1.3.3 Deformation correction

The assumption that the deformation in a single rotation is negligible is not always applicable. In order to deal with datasets that do not fulfil this assumption a less strict condition is imposed: the motion during a single projection should be negligible. While in the previous paragraph it was still possible to reconstruct the object with the projections of a single time frame without deformation artefacts, this is no longer possible. Since the object deforms during a single time frame the different projections will no longer be consistent with one another. As a result the reconstruction images are blurry and/or contain streak artefacts, these artefacts are referred to as motion artefacts or deformation artefacts. The process is visualised in Figure 1.17. Here the Shepp-Logan phantom undergoes an affine deformation during the acquisition.

Several analytic algorithms and algebraic reconstruction algorithms were developed to correct for known motion during the acquisition [39, 40]. S. Roux et al., for example, introduced a 2D exact reconstruction method for objects deforming in time by a known affine transformation [41]. These methods were generalised to a broader range of deformations [42, 43].

However, the problem in deformation correction is two-fold. While motion corrected reconstruction images can be computed, these algorithms require the deformation to be known. In practice, the exact deformation is unknown and has to be estimated. Markers and tracking systems can greatly facilitate motion estimation [44, 43] but suffer from inherent disadvantages. Firstly, marker placement is time consuming, since they have to be placed very carefully to avoid damaging the sample. Moreover, markers may shift during the acquisition. Secondly, a specialized and often costly tracking system is needed.

Alternatively, data-driven deformation estimation procedures can be used. These algorithms don't require the placement of markers and expensive tracking systems since they are completely software based. Despite these advantages, data driven motion estimation is not a trivial task. To this end an efficient deformation estimation and correction algorithm for cone beam CT data of an object undergoing affine deformation is introduced in Chapter 4.

1.3.4 Applications

Dynamic computed tomography is of great value in numerous applications. In the following a short, non-exhaustive, overview of different applications is given.

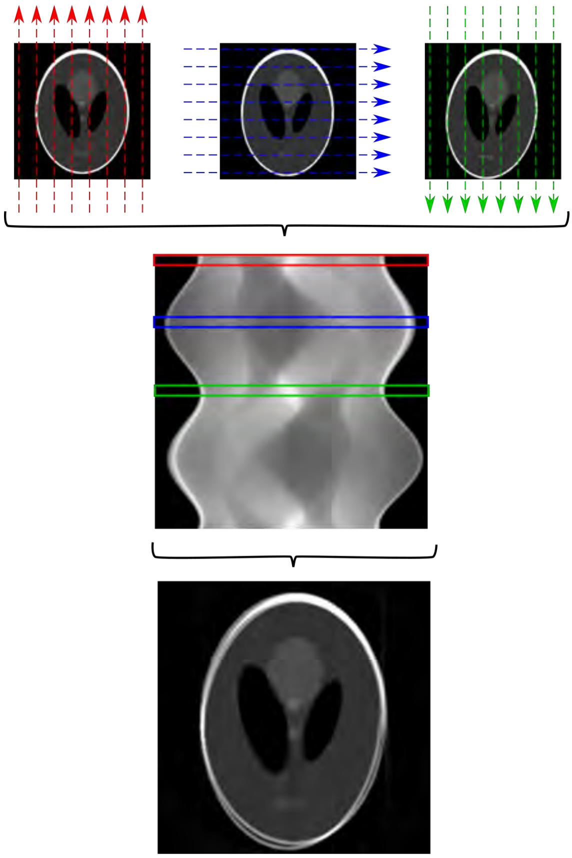

Figure 1.17: Top: The Shepp-Logan phantom (Figure 1.9) undergoing affine deformations. Middle: Sinogram of the deforming phantom. Bottom: SIRT reconstruction of the deformed sinogram.

Medical CT Medical CT is certainly the most well-known form of computed tomography. Since multiple dynamic processes take place in the body, such as cardiac and respiratory motion, it is not surprising that imaging these processes in 4D is of great interest [45, 46, 47, 48, 49, 50].

Biomedical CT Computed tomography is also of great value in biomedical research[51, 52]. To scan the small animals, such as mice and rats, special small animal scanners are available. For example, to study the animals pulmonary system and function dynamic tomography is needed [53].

Industrial CT In material science, CT is a very valuable tool to non-destructively test the properties of materials [54]. To analyse the dynamic properties of the materials dynamic CT is an important tool. These acquisitions allow to study the properties of a material (such as a foam) under compression [55, 56, 57, 58, 59] and the fluid flow inside porous materials [60, 61]. The latter is highly important for petroleum research, where the extraction of oil and gas out of tight reservoirs is closely linked with these processes [62].

Dynamic CT can even be used in the food industry, for example for imaging the leavening of pastry products [63].

References

[1] T. M. Buzug, *Computed Tomography: From Photon Statistics to Modern Cone-Beam CT*. Springer-Verlag, 2008.

[2] A. C. Kak and M. Slaney, *Principles of Computerized Tomographic imaging*. SIAM, 2001.

[3] D. E. Grideri, A. Wright, and P. Ausburn, "Electron bean melting in microfocus X-ray tubes," *J. Phys. D: Appl. Phys.*, vol. 19, pp. 2281–2992, 1986.

[4] O. Hemberg, M. Otendal, and H. M. Hertz, "Liquid-metal-jet anode electron-impact X-ray source," *Appl. Phys. Lett.*, vol. 83, pp. 1483–1485, 2003.

[5] R. Tucoulou, G. Martinez-Criado, P. Bleuet, I. Kieffer, P. Cloetens, S. Labouré, T. Martin, C. Guilloud, and J. Susini, "High-resolution angular beam stability monitoring at a nanofocusing beamline," *J. Synchrotron Radiat.*, vol. 15, pp. 392–398, 2008.

[6] M. Drakopoulos, T. Connolley, C. Reinhard, R. Atwood, O. Magdysyuk, N. Vo, M. Hart, L. Connor, B. Humphreys, G. Howell, S. Davies, T. Hill, G. Wilkin, U. Pedersen, A. Foster, N. De Maio, M. Basham, F. Yuan, and K. Wanelik, "I12: the joint engineering, environment and processing (JEEP) beamline at diamond light source," *J. Synchrotron Radiat.*, vol. 22, pp. 828–838, 2015.

[7] E. Van de Casteele, D. Van Dyck, J. Sijbers, and E. Raman, "An energy-based beam hardening model in tomography," *Phys. Med. Biol.*, vol. 47, pp. 4181–4190, 2002.

[8] M. Nikl, "Scintillation detectors for X-rays," *Meas. Sci. Techn.*, vol. 17, pp. 37–54, 2006.

[9] H. Graafsma and T. Martin, *Advanced tomographic methods in materials research and engineering*, ch. Detectors for synchrotron tomography., pp. 277–302. Oxforud University Press, 2008.

[10] J. Radon, "über die bestimmung von funktionen durch ihre integralwerte längs gewisser mannigfaltigkeiten," *Berichte über die Verhandlungen der Königlich-Sächsischen Akademie der Wissenschaften zu Leipzig, Mathematisch-Physische Klasse*, vol. 69, pp. 276–277, 1917.

[11] J. Radon, "On the determination of functions from their integral values along certain manifolds," *IEEE Trans. Med. Imag.*, vol. 5, pp. 170–176, 1986.

[12] L. A. Shepp and B. Logan, "The fourier reconstruction of a head section," *IEEE Trans. Nucl. Sci.*, vol. 21 (3), pp. 21–43, 1974.

[13] H. K. Tuy, "An inversion formula for cone-beam reconstruction," *SIAM J. Appl. Math.*, vol. 43 (3), p. 546Ũ552, 1981.

[14] P. Gangreat, *Mathematical Methods in Tomography*, ch. Mathematical framework of cone beam 3D reconstruction via the first derivative of the radon transform, pp. 66–97. Springer Berlin, 1991.

[15] M. Defrise and R. Clack, "A cone-beam reconstruction algorrithm using shift-variant filtering and cone-beam backprojection.," *IEEE trans. Med. Imag.*, vol. 13(1), pp. 186–195, 1994.

[16] L. A. Feldkamp, L. C. Davis, and J. W. Kress, "Practical cone-beam algorithm," *J. Opt. Soc. Am. A.*, vol. 1 (6), pp. 612–619, 1984.

[17] R. Proksa, T. Kohler, M. Grass, and J. Timmer, "The n-PI-method for helical cone-beam CT," *IEEE trans. Med. Imag.*, vol. 19 (9), pp. 848 – 863, 2000.

[18] D. Pelt and K. Batenburg, "Fast tomographic reconstruction from limited data using artificial neural networks.," *IEEE Trans. Image Process.*, vol. 22 (12), pp. 5238–5251, 2013.

[19] D. Pelt and K. Batenburg, "Accurately approximating algebraic tomographic reconstruction by filtered backprojection.," in *Proceedings of the 2015 International Meeting on Fully Three-Dimensional Image Reconstruction in Radiology and Nuclear Medicine.*, 2015.

[20] S. Gazzola and J. G. Nagy, "Generalized Arnoldi–Tikhonov method for sparse reconstruction," *SIAM Journal on Scientific Computing*, vol. 36, no. 2, pp. B225–B247, 2014.

[21] M. R. Hestenes and E. Stiefel, "Methods of conjugate gradients for solving linear systems," *J. Compt. Appl. Math.*, vol. 236(8), pp. 2167–2178, 2012.

[22] J. Gregor and T. Benson, "Computational analysis and improvement of SIRT.," *IEEE Trans. Med. Imaging*, vol. 27, pp. 918–924, Jan. 2008.

[23] T. Elfving, P. C. Hansen, and T. Nikazad, "Semi-convergence properties of kaczmarz's method," *Inverse Problems*, vol. 30 (5), pp. 16846–13114, 2014.

[24] A. Chambolle, "An algorithm for total variation minimization and applications," *J. Math. Imaging Vision*, vol. 20, pp. 89–97, 2004.

[25] K. J. Batenburg and J. Sijbers, "DART: A practical reconstruction algorithm for discrete tomography.," *IEEE trans. image process.*, vol. 20 (9), pp. 2542–2553, 2011.

[26] W. van Aarle, K. J. Batenburg, and J. Sijbers, "Automatic parameter estimation for the discrete algebraic reconstruction technique (DART)," *IEEE Trans. Image Process.*, vol. 21 (11), no. 11, pp. 4608–4621, 2012.

[27] G. Van Eyndhoven, M. Kurttepeli, C. J. Van Oers, P. Cool, S. Bals, K. J. Batenburg, and J. Sijbers, "Pore reconstruction and segmentation (PORES) method for improvedporosity quantization of nanoporous materials," *Ultramicroscopy*, vol. 148, pp. 10–19, 2015.

[28] T. Roelandts, K. J. Batenburg, E. Biermans, C. Kübel, S. Bals, and J. Sijbers, "Accurate segmentation of dense nanoparticles by partially discrete electron tomography.," *Ultramicroscopy*, vol. 114, pp. 96–105, Mar. 2012.

[29] J. Cant, W. J. Palenstijn, G. Behiels, and J. Sijbers, "Modeling blurring effects due to continuous gantry rotation: Application to region of interest tomography.," *Med. Phys.*, vol. 42 (5), pp. 2709–2717, 2015.

[30] P. M. Joseph, "An improved algorithm for reprojecting rays through pixel images," *IEEE trans. Med. Imag.*, vol. 1, pp. 192–196, 1982.

[31] W. J. Palenstijn, K. J. Batenburg, and J. Sijbers, "Performance improvements for iterative electron tomography reconstruction using graphics processing units (GPUs)," *J. Struct. Biol.*, vol. 176, pp. 250–253, Nov. 2011.

[32] W. Van Aarle, W. J. Palenstijn, J. De Beenhouwer, T. Altantzis, S. Bals, K. J. Batenburg, and J. Sijbers, "The ASTRA toolbox: A platform for advanced algorithm development in electron tomography," *Ultramicroscopy*, vol. 157, pp. 35–47, Oct. 2015.

[33] W. Van Aarle, W. J. Palenstijn, J. Cant, E. Janssens, F. Bleichrodt, A. Dabravolski, J. De Beenhouwer, and J. Sijbers, “Fast and flexible X-ray tomography using the ASTRA toolbox,” *Opt. Express*, vol. 24, no. 22, pp. 25129–25147, 2016.

[34] B. Andia, *Nonlinear backprojection.* PhD thesis, University of Notre Dame, Indiana, 2000.

[35] B. De Man, J. Nuyts, P. Dupont, G. Marchal, and P. Suetens, “An iterative maximum-likelihood polychromatic algorithm for CT,” *IEEE trans. Med. Imag.*, vol. 20 (10), pp. 999–1008, 2001.

[36] G. Van Eyndhoven, K. J. Batenburg, D. Kazantsev, V. Van Nieuwenhove, P. D. Lee, K. J. Dobson, and J. Sijbers, “An iterative CT reconstruction algorithm for fast fluid flow imaging,” *IEEE Trans. Image Process.*, vol. 24, no. 11, pp. 4446–4458, 2015.

[37] D. Kazantsev, W. M. Thompson, W. R. B. Lionheart, G. Van Eyndhoven, A. P. Kaestner, K. J. Dobson, P. J. Withers, and P. D. Lee, “4D-CT reconstruction with unified spatial-temporal patch-based regularization,” *Inverse Probl. Imag.*, vol. 9, pp. 447–467, May 2015.

[38] A. Kaestner, B. Münch, P. Trtik, and L. Butler, “Spatiotemporal computed tomography of dynamic processes,” *Opt. Eng.*, vol. 50, p. 123201, Dec. 2011.

[39] A. A. Isola, A. Ziegler, T. Koehler, W. J. Niessen, and M. Grass, “Motion-compensated iterative cone-beam CT image reconstruction with adapted blobs as basis functions.,” *Phys. Med. Biol.*, vol. 53, pp. 6777–97, Dec. 2008.

[40] S. Rit, D. Sarrut, and L. Desbat, “Comparison of analytic and algebraic methods for motion-compensated cone-beam CT reconstruction of the thorax.,” *IEEE Transactions on Medical Imaging*, vol. 28, pp. 1513–25, Oct. 2009.

[41] S. Roux, L. Desbat, A. Koenig, and P. Grangeat, “Exact reconstruction in 2D dynamic CT: compensation of time-dependent affine deformations,” *Phys. Med. Biol.*, vol. 49, pp. 2169–2182, Jun. 2004.

[42] L. Desbat and S. Roux, “Compensation of some time dependent deformations in tomography,” *IEEE T. Med. Imaging*, vol. 26, no. 2, pp. 261–269, 2007.

[43] B. N. Hahn, “Motion estimation and compensation strategies in dynamic computerized tomography,” *Sens. Imaging*, vol. 18 (10), 2017.

[44] J.-H. Kim, J. Nuyts, A. Kyme, Z. Kuncic, and R. Fulton, “A rigid motion correction method for helical computed tomography (CT),” *Phys. Med. Biol.*, vol. 60, pp. 2047–2073, Feb. 2015.

[45] M. Kachelrieß, S. Schaller, and W. A. Kalender, “Advanced single-slice rebinning in cone-beam spiral CT,” *Medical Physics*, vol. 27, no. 4, pp. 754–772, 2000.

[46] M. Grass, R. Manzke, T. Nielsen, P. Koken, R. Proksa, M. Natanzon, and G. Shechter, "Helical cardiac cone beam reconstruction using retrospective ECG gating," *Physics in medicine and biology*, vol. 48, no. 18, p. 3069, 2003.

[47] M. Kachelrieß, M. Knaup, and W. A. Kalender, "Extended parallel backprojection for standard three-dimensional and phase-correlated four-dimensional axial and spiral cone-beam CT with arbitrary pitch, arbitrary cone-angle, and 100% dose usage," *Medical Physics*, vol. 31, no. 6, pp. 1623–1641, 2004.

[48] T. Nielsen, R. Manzke, R. Proksa, and M. Grass, "Cardiac cone-beam CT volume reconstruction using ART," *Medical physics*, vol. 32, no. 4, pp. 851–860, 2005.

[49] P. Koken and M. Grass, "Aperture weighted cardiac reconstruction for cone-beam CT," *Physics in medicine and biology*, vol. 51, no. 14, p. 3433, 2006.

[50] R. Manzke, M. Grass, T. Nielsen, G. Shechter, and D. Hawkes, "Adaptive temporal resolution optimization in helical cardiac cone beam CT reconstruction," *Medical physics*, vol. 30, no. 12, pp. 3072–3080, 2003.

[51] C. T. Badea, B. Fubara, L. W. Hedlund, and G. A. Johnson, "4-D micro-CT of the mouse heart," *Molecular Imaging*, vol. 4, no. 2, p. 15353500200504187, 2005.

[52] J. Song, Q. H. Liu, G. A. Johnson, and C. T. Badea, "Sparseness prior based iterative image reconstruction for retrospectively gated cardiac micro-CT," *Medical physics*, vol. 34, no. 11, pp. 4476–4483, 2007.

[53] C. T. Badea, L. W. Hedlund, and G. A. Johnson, "Micro-CT with respiratory and cardiac gating," *Med. Phys.*, vol. 31 (12), pp. 3324–3329, 2004.

[54] V. Cnudde and M. Boone, "High-resolution X-ray computed tomography in geosciences: A review of the current technology and applications," *Earth-Science Reviews*, vol. 123, pp. 1–17, aug 2013.

[55] B. K. Bay, T. S. Smith, D. P. Fyhrie, and M. Saad, "Digital volume correlation: three-dimensional strain mapping using X-ray tomography," *Experimental mechanics*, vol. 39, no. 3, pp. 217–226, 1999.

[56] J. Elliott, A. Windle, and J. Hobdell, "In-situ deformation of an open-cell flexible polyurethane foam characterised by 3D computed microtomography," *Journal of materials*, vol. 7, pp. 1547–1555, 2002.

[57] N. Lenoir, M. Bornert, J. Desrues, P. Bésuelle, and G. Viggiani, "Volumetric digital image correlation applied to X-ray microtomography images from triaxial compression tests on argillaceous rock," *Strain*, vol. 43, no. 3, pp. 193–205, 2007.

[58] N. Watanabe, T. Ishibashi, Y. Ohsaki, Y. Tsuchiya, T. Tamagawa, N. Hirano, H. Okabe, and N. Tsuchiya, "X-ray CT based numerical analysis of fracture flow for core samples under various confining pressures.," *Engineering Geology*, vol. 123, no. 4, pp. 338–346, 2011.

[59] G. Viggiani, N. Lenoir, P. Bésuelle, M. Di Michiel, S. Marello, J. Desrues, and M. Kretzschmer, "X-ray microtomography for studying localized deformation in fine-grained geomaterials under triaxial compression," *Comptes rendus Mécanique*, vol. 332, no. 10, pp. 819–826, 2004.

[60] D. Wildenschild and A. P. Sheppard, "X-ray imaging and analysis techniques for quantifying pore-scale structure and processes in subsurface porous medium systems," *Advances in Water Resources*, vol. 51, pp. 217–246, 2013.

[61] D. Silin, L. Tomutsa, S. M. Benson, and T. W. Patzek, "Microtomography and pore-scale modeling of two-phase fluid distribution," *Transport in Porous Media*, vol. 86, no. 2, pp. 495–515, 2011.

[62] A. N. Golab, M. A. Knackstedt, H. Averdunk, T. Senden, A. R. Butcher, and P. Jaime, "3D porosity and mineralogy characterization in tight gas sandstones," *The Leading Edge*, vol. 29, no. 12, pp. 1476–1483, 2010.

[63] F. Koksel, S. Aritan, A. Strybulevych, J. H. Page, and M. G. Scanlon, "The bubble size distribution and its evolution in non-yeasted wheat flour doughs investigated by synchrotron X-ray microtomography," *Food Res. Int.*, vol. 80, pp. 12 – 18, 2016.

2

Dynamic intensity normalization

Contents

2.1 Introduction 34
2.2 Method 35
  2.2.1 Conventional flat field correction 35
  2.2.2 Dynamic flat field correction 36
2.3 Experiments 40
  2.3.1 Simulation study 40
  2.3.2 Experimental data 42
2.4 Results and discussion 43
  2.4.1 Simulation study 43
  2.4.2 Experimental data 45
  2.4.3 General remarks 50
2.5 Conclusion 52
References 52

This chapter has been published as:
V. Van Nieuwenhove, J. De Beenhouwer, F. De Carlo, L. Mancini, F. Marone and J. Sijbers, *"Dynamic intensity normalization using eigen flat fields in X-ray imaging"*, Optics Express, vol. 26, no. 3, pp. 1441-1451, 2017.

2.1 Introduction

In X-ray imaging, the acquired projection images generally suffer from fixed-pattern noise, which is one of the limiting factors of image quality. It may stem from beam inhomogeneity, gain variations of the detector response due to inhomogeneities in the photon conversion yield, losses in charge transport, charge trapping, or variations in the performance of the readout [1]. Also, the scintillator screen may accumulate dust and/or scratches on its surface and in the bulk, resulting in systematic patterns in every acquired X-ray projection image.

In X-ray Computed Tomography (CT), fixed-pattern noise is known to significantly degrade the achievable spatial resolution and generally leads to ring or band artifacts in the reconstructed images [2, 3, 4]. This, in turn, hampers quantitative analysis and complicates post processing such as noise reduction or segmentation [5]. If the pattern noise is truly stationary (i.e., exactly the same in each acquired projection image), substantial reduction of fixed pattern noise is easy.

The conventional method to reduce fixed-pattern noise is known as flat field correction (FFC) [6]. Projection images without sample are acquired with and without the X-ray beam turned on, which are referred to as flat fields and dark fields. The flat fields include the non-uniform sensitivity of the charge-coupled device (CCD) pixels, the non-uniform response of the scintillator screen, as well as the inhomogeneities of the incident X-ray beam. Based on the acquired flat and dark fields, the measured projection images with sample are then normalized.

While conventional FFC correction is an elegant and easy procedure that largely reduces fixed-pattern noise, it heavily relies on the stationarity of the beam, scintillator response and CCD sensitivity. In practice, however, this assumption is only approximately met. Indeed, detector elements are characterized by intensity dependent, nonlinear response functions and the incident beam often has time dependent non-uniformities [7], which renders conventional FFC inadequate. In synchrotron X-ray tomography, there is an even broader array of time dependent fluctuations. A range of components of the synchrotron cause beam variability: instability of the bending magnets of the synchrotron, temperature variations due to the water cooling in mirrors and the monochromator, or vibrations of the scintillator and other beamline components [8]. The latter is responsible for the biggest variations in the flat fields. The variation of the total incident X-ray intensity over time is another cause of flat field variation. Synchrotrons working in 'top-up' mode inject, at regular times, new electrons into the storage ring, resulting in a typical saw-tooth function of the X-ray flux over time [9]. As a result, after conventional FFC, often significant intensity variation remains in the sinogram, leading to ring artifacts in the reconstructed image as concentric arcs or half-circles with varying intensity.

Little work has been presented so far to deal with temporal fluctuations in the flat fields. In [8], an adaptive time-dependent intensity normalization was proposed in which the flat field is modelled by the product of a multiplicative function defined by dust or dirt on the surfaces of the scintillator and CCD camera, and a function describing a time dependent intensity profile of the X-ray beam incident on the sample. In [10], a FFC method together with an automated scanning mechanism was proposed in which the flat field images and projection data are acquired every view alternately. When acquiring the flat field image, the imaging sample is moved away from the field-of-view by a computer controlled linear positioning stage. While such a procedure allows view-by-view normalization, the mechanical set-up significantly lengthens the acquisition time. Moreover, it requires perfect repositioning of the sample, which is non-trivial.

In this chapter, we propose a general, fast and simple method to account for time dependent variations in the flat fields. It estimates the flat field at the acquisition time of the projection in order to normalize the projection individually. Firstly, the technique performs a Principal Component Analysis (PCA) of flat fields acquired prior, during and/or posterior to the X-ray tomographic experiment [11]. Afterwards, the weights of the most important PCA components are estimated for each projection, minimizing a total variation criterion [12]. The estimated flat field is then used to normalize the corresponding projection.

2.2 Method

In this section, we will revisit the conventional FFC method (subsection 2.2.1), which is the standard normalization technique in X-ray imaging. Next, in subsection 2.2.2, the proposed dynamic FFC algorithm is described, which deals with non-stationary flat fields.

2.2.1 Conventional flat field correction

The attenuation of a monochromatic X-ray beam is described by the Beer-Lambert law, stating that:

$$I = I_0 \cdot \exp\left(-\int \mu(l)\, dl\right), \tag{2.1}$$

with I the outgoing intensity, I_0 the incoming intensity, μ the attenuation coefficient of the object and l the coordinate along the X-ray path. The integral $\int \mu(l)\, dl$ is the total attenuation of the beam along a given ray.

Prior to the reconstruction of a cross section or volume, the projection data are normalized with respect to I_0:

$$\int \mu(l)\, dl = -\ln\left(\frac{I}{I_0}\right). \tag{2.2}$$

In practice, an estimate of p as well as I_0 can be obtained from projections with and without object, respectively. This normalization procedure is known as **flat field correction (FFC)**. Conventional FFC relies on a dark field, a flat field, and the projection image to be normalized:

Dark field : A dark field $\boldsymbol{d}$, often referred to as the offset field, is an image which is captured by the detector without X-ray illumination. The signal detected in the absence of X-rays from the X-ray source includes both the true dark current (which is proportional to the exposure time), and the digitization offset, which is independent of exposure time. Usually, the exposure time for the acquisition of dark field images is equal to that of the projection images.

Flat field : A flat field $\boldsymbol{f}$, often referred to as a white field or gain field, is acquired with X-ray illumination, but without the presence of the sample. It is used to measure and correct for inhomogeneities in the X-ray beam intensity profile and detector response.

Projection image : projection images $\{\boldsymbol{I}_j\}$ are acquired with X-ray illumination and the sample is positioned in the field of view of the detector. These images are acquired while the sample rotates, usually in regular angular intervals.

Based on these images, an intensity normalized image $\boldsymbol{n}_j$ is computed as follows:

$$\boldsymbol{n}_j = \frac{\boldsymbol{I}_j - \boldsymbol{d}}{\boldsymbol{f} - \boldsymbol{d}}. \tag{2.3}$$

Since $\boldsymbol{f}$ as well as $\boldsymbol{d}$ contain noise, the variance of the normalized image $\boldsymbol{n}_j$ is larger than the variance of $\boldsymbol{I}_j$, due to noise propagation. To limit this effect, $\boldsymbol{d}$ and $\boldsymbol{f}$ are replaced in practice by the average of a large number of dark and flat fields, $\bar{\boldsymbol{d}}$ and $\bar{\boldsymbol{f}}$, respectively [1].

2.2.2 Dynamic flat field correction

Conventional FFC as described in subsection 2.2.1 is only valid if the flat fields are stationary (i.e., do not change over time). If this is not the case, FFC based on a simple averaged flat field will introduce a bias in the normalized image.

We propose an advanced FFC method that accounts for higher order dynamics in the flat fields. Thereby, each projection is normalized individually with its corresponding flat field:

$$\boldsymbol{n}_j = \frac{\boldsymbol{I}_j - \bar{\boldsymbol{d}}}{\boldsymbol{f}_j - \bar{\boldsymbol{d}}}, \tag{2.4}$$

with $\boldsymbol{f}_j$ the flat field at the acquisition moment of projection $\boldsymbol{I}_j$. Since $\boldsymbol{f}_j$ is unknown, it has to be estimated. The main idea is to first capture the dynamics in the flat fields from a set of flat fields (acquired prior, during or after the experiment) and next exploit the dynamics to individually normalize each projection image. This will be explained in a more formal way in the following subsections.

2.2.2.1 Eigen flat fields

Let $\boldsymbol{f} \equiv \{f_n\} \in \mathbb{R}^N$ a column vector representing a flat field (i.e., a vector composed of concatenated columns of a 2D projection with N pixels). If M flat field images are acquired, these images can be stored in a flat field matrix $\boldsymbol{F} \equiv \{\boldsymbol{f}_m\} = (\boldsymbol{f}_1, ..., \boldsymbol{f}_M) \in \mathbb{R}^{N \times M}$. Let $\bar{\boldsymbol{f}}$ represent the mean flat field. Then, each flat field $\boldsymbol{f}_m$ can be represented in a low dimensional ($K \ll N$) space using PCA. That is, it can be well approximated by a linear combination of K eigen flat fields $\{\boldsymbol{u}_k\}$, the principal components, as follows:

$$\boldsymbol{f}_m \approx \bar{\boldsymbol{f}} + \sum_{k=1}^{K} w_{mk} \boldsymbol{u}_k. \tag{2.5}$$

Computation of eigen flat fields Turk and Pentland proposed an efficient procedure to compute the eigen images [13]: Given a set of M flat fields $\boldsymbol{F} = (\boldsymbol{f}_1, ..., \boldsymbol{f}_M)$, a centered flat field matrix $\boldsymbol{A} \in \mathbb{R}^{N \times M}$ is computed by subtracting the mean flat field $\bar{\boldsymbol{f}}$ from each individual flat field:

$$\boldsymbol{A} = (\boldsymbol{f}_1 - \bar{\boldsymbol{f}}, ..., \boldsymbol{f}_M - \bar{\boldsymbol{f}}). \tag{2.6}$$

The goal is then to find the eigen vectors and eigen values of the covariance matrix $\boldsymbol{C} = \boldsymbol{A}\boldsymbol{A}^T$. Since $\boldsymbol{C} \in \mathbb{R}^{N \times N}$ is a huge matrix, calculating its eigenvectors is computationally expensive. Fortunately, as shown by Turk and Pentland, this problem can be efficiently dealt with by computing the eigenvectors $\{\boldsymbol{v}_i\}$ and eigenvalues $\{\lambda_i\}$ of the $M \times M$ matrix $\boldsymbol{A}^T\boldsymbol{A}$. Then, $\{\boldsymbol{A}\boldsymbol{v}_i\} = \{\boldsymbol{u}_k\}$ and $\{\lambda_i\}$ are the eigenvectors, referred to as eigen flat fields (EFFs), and eigenvalues of $\boldsymbol{C}$, respectively.

Selection of the eigen flat fields Once the EFFs are computed, the most important EFFs (i.e., the EFFs describing most of the variation in the flat fields) have to be selected. Many criteria exist to select an optimal number of Principal

Components (EFFs), such as the Kaisers criterion, the cumulative percentage of total variation, or the scree test [14, 11]. Here, we opted for a statistically justified approach based on *parallel analysis* [15]. Parallel analysis selects only those components of which the eigenvalues are significantly larger than the corresponding eigen values of a dataset with the same variation but with independent variables. To this end, a large number (S) of matrices with the same dimensions as $\boldsymbol{A}$ are sampled from a multivariate normal distribution with a diagonal covariance matrix of which the elements are identical to those of the covariance matrix $\boldsymbol{C}$. Then, PCA is conducted on these matrices and the eigenvalues $\{\lambda_{i,s}\}_{s=1}^{S}$ are collected. If λ_i of $\boldsymbol{C}$ is larger than the 95^{th} percentile of the set $\{\lambda_{i,s}\}_{s=1}^{S}$ of the covariance matrix of the sampled matrices, the i^{th} EFF is retained.

Filtering of the eigen flat fields In the previous step, the EFFs were selected that describe most of the variation in the flat fields. Compared to the remaining EFFs, the signal-to-noise ratio (SNR) of the selected EFFs is much higher, but obviously not noiseless. To limit noise propagation in the dynamic FFC method proposed in section 2.2.2.2, the selected EFFs are filtered using a block matching filter [16].

2.2.2.2 Dynamic flat field estimation

Once the EFFs are computed from the set of flat fields acquired prior, during and/or posterior to the actual measurements, each measured projection is normalized with its corresponding flat field $\widehat{\boldsymbol{f}}_j$ (see Eq. 2.4). This flat field is generated by linearly combining K principal EFFs:

$$\widehat{\boldsymbol{f}}_j = \bar{\boldsymbol{f}} + \sum_{k=1}^{K} \hat{w}_{jk} \boldsymbol{u}_k, \tag{2.7}$$

where $\{\hat{w}_{jk}\}$ denote the estimates of the weights corresponding to the EFFs. The goal is then to find these weights such that the estimated flat field $\widehat{\boldsymbol{f}}_j$ approaches the true flat field $\boldsymbol{f}_j$. We assume that, if this is the case, the variation in the normalized projection $\boldsymbol{n}_j$ is minimal.

Total variation minimization Finding the optimal weights of the flat fields, $\{\hat{w}_{jk}\}$, is accomplished by searching for the linear combination that minimizes the total variation (TV) in each normalized projection $\boldsymbol{n}_j$. However, simply minimizing $\mathrm{TV}(\boldsymbol{n}_j)$ would lead to ever increasing weights $\{\hat{w}_{jk}\}$. Indeed, the TV of an image $\boldsymbol{i}$ is a homogeneous function of degree one for $a \in \mathbb{R}^+$, i.e. $\mathrm{TV}(a\,\boldsymbol{i}) = a\,\mathrm{TV}(\boldsymbol{i})$. Consequently, minimizing TV promotes images with a low mean. To prevent the algorithm favoring normalized projections with high valued flat fields, the TV is multiplied with $c(\{w_{jk}\})$, the mean of the applied flat field. This results in the following optimization problem:

$$\{\hat{w}_{jk}\} = \arg\min_{\{w_{jk}\}} c(\{w_{jk}\}) \cdot \sum_{n=1}^{N} \nabla \boldsymbol{n}_j(\{w_{jk}\})|_n| \tag{2.8}$$

with

$$\boldsymbol{n}_j(\{w_{jk}\}) = \left(\boldsymbol{I}_j - \bar{\boldsymbol{d}}\right) / \left(\bar{\boldsymbol{f}} + \sum_{k=1}^{K} w_{jk}\boldsymbol{u}_k - \bar{\boldsymbol{d}}\right) \tag{2.9}$$

and

$$c(\{w_{jk}\}) = \frac{1}{N}\sum_{n=1}^{N}\left(\bar{f}_n + \sum_{k=1}^{K} w_{jk}u_{k,n} - \bar{d}_n\right). \tag{2.10}$$

The factor $\sum_{n=1}^{N} |\nabla \boldsymbol{n}_j(\{w_{jk}\})|_n$ of the objective function, which is minimized in Eq. 2.8, denotes the TV of the normalized projection: $TV(\boldsymbol{n}_j)$.

The objective function is minimized using a quasi-Newton method[17]. This nonlinear optimization algorithm is an alternative to Newton's method in which the Hessian is approximated, reducing the computational cost of the algorithm. Two stopping criteria are used: a tolerance level of 10^{-6} and a maximum number of iterations (400). The weights $\{w_{jk}\}$ are estimated from down sampled projections and EFFs. This has two advantages: for one, the effect of noise on the TV is significantly reduced, resulting in a more robust estimation. Secondly, it substantially increases the speed of the algorithm.

Intensity rescaling The TV criterion is sensitive to structural changes but insensitive to image offsets. Hence, we propose a rescaling of the projections after normalization. This procedure is different for truncated and non-truncated projections. Truncated projections are rescaled such that they have the same mean as the conventional flat field corrected projections. For non-truncated parallel beam projections the first Helgason-Ludwig consistency condition is used [18], stating that the sum of all the attenuation coefficients should be the same in every projection. Each dynamic flat field corrected non-truncated projection is rescaled such that they have the same mean as that of the full conventional flat field corrected dataset.

An overview of the dynamic FFC algorithm is shown in Figure 2.1.

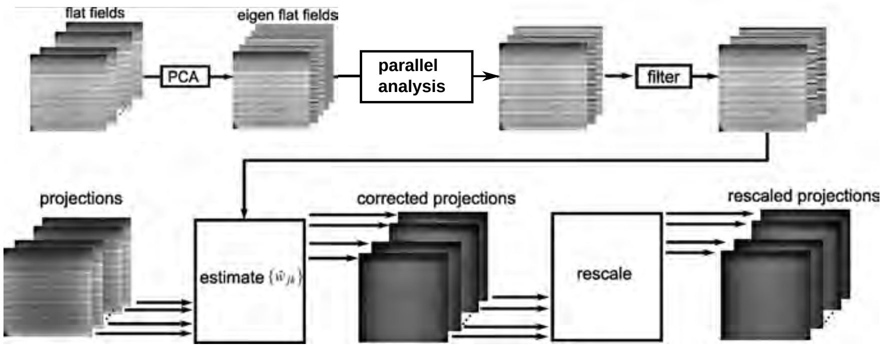

Figure 2.1: Overview of the dynamic FFC algorithm.

2.3 Experiments

To validate the dynamic FFC methodology, simulations (section 2.3.1) as well as real experiments (section 2.3.2) were performed. All reconstructions were computed using the ASTRA tomography toolbox [19, 20].

2.3.1 Simulation study

A 3D spatial resolution software phantom (see Figure 2.2) was generated on a 768×768×200 voxel grid. The Astra toolbox was used to simulate 500 log corrected projections with parallel beam geometry and an angular range 180 degrees [19]. A set of real flat fields of a foam imaging experiment (see section 2.3.2.2), 250 prior and 250 post flat fields, were applied on the simulated projections as described by the Beer-Lambert law (Eq. 2.1):

$$\boldsymbol{I}_{j,sim} = \boldsymbol{f}_j \cdot e^{-\boldsymbol{n}_j}, \tag{2.11}$$

with $\boldsymbol{n}_j$ the j'th simulated projection, $\boldsymbol{f}_j$ the j'th flat field of the foam dataset and $\boldsymbol{p}_{j,sim}$ the j'th projection with simulated dynamic flat fields. This procedure essentially simulates realistic dynamic flat fields. The remaining 50 prior and 50 post flat fields of the foam datasets were used to correct the projections with the conventional FFC as well as to compute the EFFs in the dynamic FFC. All flat fields were filtered with Non-Local Means to reduce noise [21].

In a first experiment, the number of flat fields and the number of EFFs were varied between 5 to 49 and 1 to 5, respectively. In a second experiment, the number of projections was varied from 5 to 500 in steps of 10, all with an angular range of 180 degrees. Two EFFs, calculated from a set of 100 flat fields, were used for

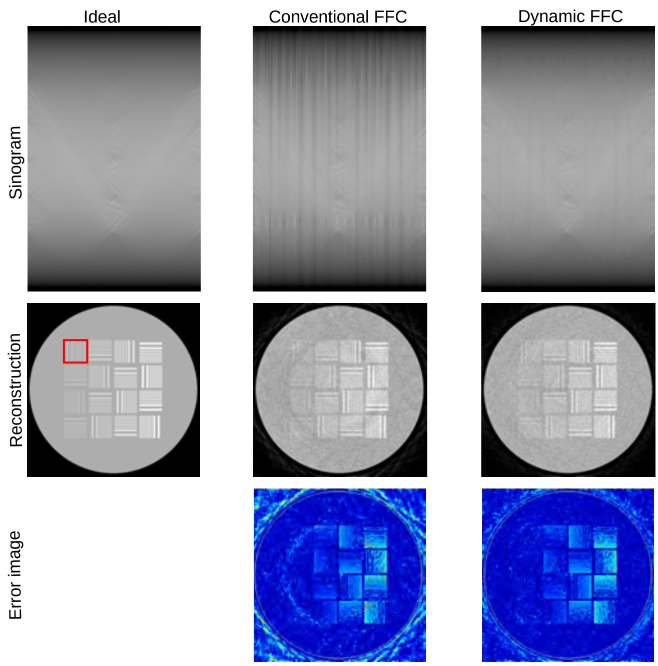

Figure 2.2: Sinograms, reconstructions and error images of slice 129 for conventional FFC and dynamic FFC are shown. For the dynamic FFC of the 500 projections, 2 EFFs, based on 100 flat fields, were calculated. The red square in the phantom images indicates the ROI in which the MSE was calculated.

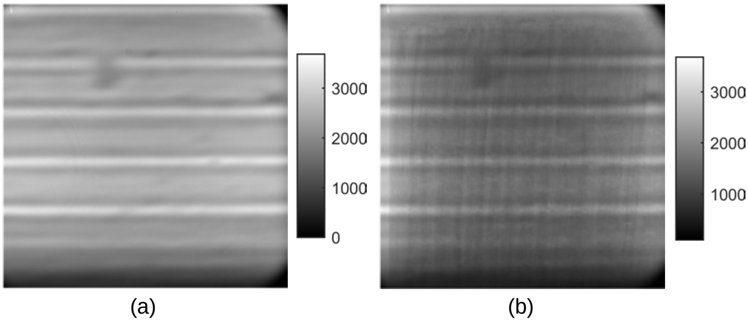

Figure 2.3: (a) Mean posterior flat field of the aluminum peroxide dataset. (b) The first projection of the aluminum peroxide dataset.

dynamic FFC. All reconstructions were made using SIRT with 300 iterations.

Both the normalized projections and corresponding SIRT reconstructions were assessed visually and quantitatively. To quantify the results, the Mean Squared Error (MSE) of the normalized projections as well as the MSE of the reconstructions was computed. The MSE in the projection domain was calculated on all projection data and the reconstruction MSE was calculated in a 100×100 region of interest (ROI) (see Figure 2.2).

2.3.2 Experimental data

The dynamic FFC algorithm was tested on two X-ray tomography datasets, each from a different synchrotron facility, and compared to conventional FFC.

2.3.2.1 Aluminum peroxide

At the Advanced Photon Source (APS) of the Argonne National Laboratory, a tomography dataset of an aluminum peroxide structure was acquired. The dataset consisted of 1 dark field, 100 posterior flat fields and 1500 equiangular projections, with an angular range of 180 degrees. Each of the projections (2048×2048 pixels) was acquired with an exposure time of 300 ms. The mean of the posterior flat fields and a projection are shown in Figure 2.3. The dataset was processed using conventional as well as dynamic FFC. The dynamic flat field weights $\{w_{jk}\}$ were estimated on 20 times down sampled projections and afterwards applied to the full scale projections. Due to the limited amount of truncation the dynamic FFC projections were rescaled using the first Helgason-Ludwig consistency condition [18]. Filtered Back Projection (FBP) reconstructions were made using the ASTRA toolbox [6, 19, 20].

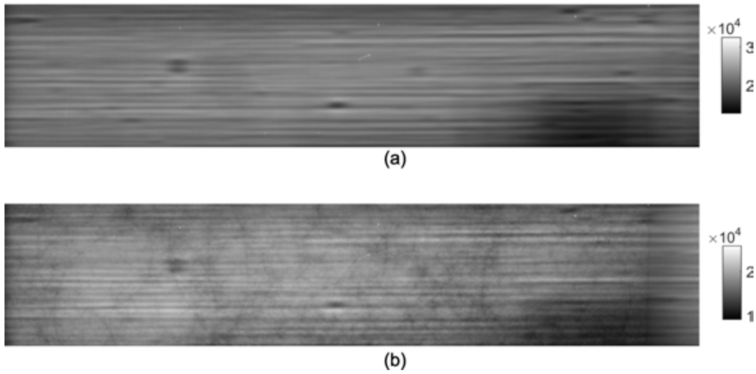

Figure 2.4: (a) Mean of the prior and posterior flat fields of the foam dataset. (b) The first projection of the foam dataset.

2.3.2.2 Foam

A ROI tomographic dataset of a foam structure was acquired at the Tomcat beamline of the Swiss Light Source (SLS) of the Paul Scherrer Institute (PSI). The dataset consisted of 20 dark fields, 300 prior flat fields, 251 projections and 300 posterior flat fields. Each projection (256×1248 pixels) was acquired with an exposure time of 30 ms. The mean flat field and a projection are shown in Figure 2.4. The dataset was processed using conventional FFC and dynamic FFC, with one up to five EFFs. The dynamic flat field weights $\{w_{jk}\}$ were estimated on 20 times down sampled projections and afterwards applied to the full scale projections. Cross sections of the dataset were reconstructed with 200 iterations of SIRT and with FBP.

2.4 Results and discussion

2.4.1 Simulation study

2.4.1.1 Number of EFFs and flat fields

Figure 2.2 shows the results of conventional and dynamic FFC (500 projections, 100 flat fields and 2 EFFs) on both the projections and the reconstructions. The projections with conventional FFC clearly suffer from vertical stripes in the sinogram due to flat field variations. These artifacts are almost completely removed with dynamic FFC. The effect of flat field variation manifests itself as broad ring artifacts in the reconstruction, which are also clearly visible in the error image.

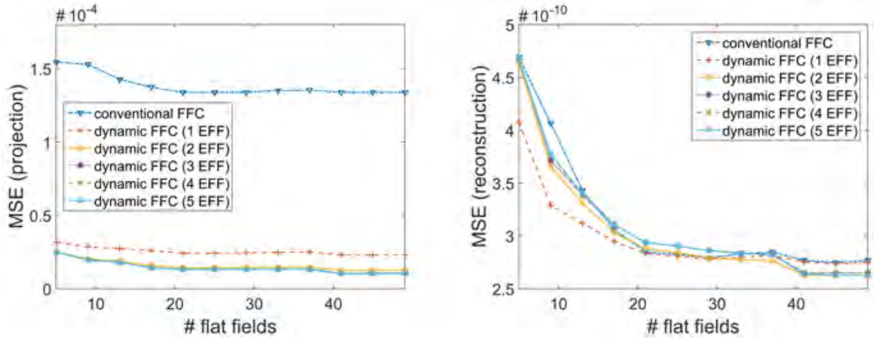

Figure 2.5: MSE of the projections (left) and the reconstructions (right) for both conventional FFC and dynamic FFC with 1 to 5 EFFs in function of the **number of flat fields**.

Both the reconstruction and error image based on dynamic FFC show a substantial reduction of these artifacts.

In Figure 2.5, the MSE of the projections and reconstructions is shown for conventional and dynamic FFC in function of the number of flat fields and EFFs. It can be observed that the MSE of the projections decreases slowly in function of the number of flat fields. Increasing the number of flat fields obviously improves the SNR of the EFFs and, as a result, improves the quality of the dynamic FFC projections. The MSE of the projections also decreases when more EFFs are used, although higher order (4th and 5th) EFFs only have a limited effect on the projection quality. This behavior was expected, as increasing the number of EFFs improves the description of the estimated flat fields as long as they contain sufficient structural information.

The MSE of the reconstructions shows a more complex behavior. In general, the reconstruction quality improves with an increasing number of flat fields, which is to be expected, mainly because the increase of SNR of the EFFs. For a rather small number of flat fields (< 30), dynamic FFC with only 1 EFF performs best in terms of MSE. If more flat fields are available, the SNR of the second EFF is sufficiently high, hence improving the normalization when taking the second EFF into account. The use of more flat fields results in less noisy high order EFFs that enable a better description of the actual structural variation. In practice, as many flat fields as possible should be acquired to obtain a high SNR of at least the low order EFFs. Parallel analysis (cfr. section 2.2.2) indeed suggests a similar number of EFFs: one EFF if less than 33 flat fields are acquired and two EFFs if 33 to 49 flat fields are used. It is clear that dynamic FFC outperforms conventional FFC in terms of projection MSE for all numbers of flat fields. Furthermore, dynamic FFC generally leads to improved reconstruction (quantified by the reconstruction

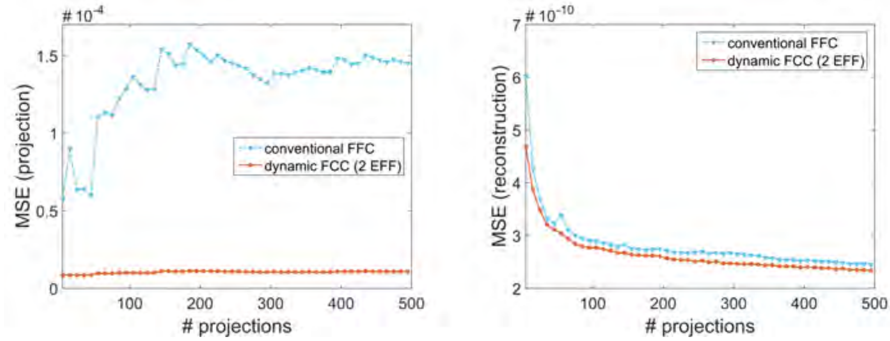

Figure 2.6: MSE of the projections (left) and the reconstructions (right) for both conventional FFC and dynamic FFC (100 flat fields, 2 EFFs) in function of the **number of projections**.

MSE).

2.4.1.2 Number of projections

Figure 2.6 shows the MSE in the projection (left) and reconstruction domain (right) for conventional and dynamic FFC in function of the number of projections. Clearly, the MSE of the projections decreases substantially if dynamic FFC is used instead of conventional FFC. After conventional FFC, one can observe large variation in MSE as a function of the number of projections. In contrast, after dynamic FFC, there is almost no variation of the MSE as a function of the projections, which indicates that even severely distorted projections are properly corrected. The MSE of the reconstructions is in all cases slightly lower for the dynamic FFC than for the conventional FFC. This difference decreases with increasing number of projections. This can be explained by the back projection during reconstruction in which the remaining errors after FFC are averaged out.

2.4.2 Experimental data

2.4.2.1 Aluminum peroxide

The aluminum peroxide EFF's structure consists mainly of horizontal stripes (see Figure 2.7), with decreasing intensity with increasing order of EFF. The EFFs clearly reveal structural variation in the flat fields as otherwise, only random noise would have been present in the EFFs, being the only source of variation.

A projection of the aluminum dataset, corrected with conventional and dynamic FFC with 1 to 5 EFFs is shown in Figure 2.8(a) and Figure 2.8(b-f), respectively. The majority of the projections that are processed with conventional FFC are

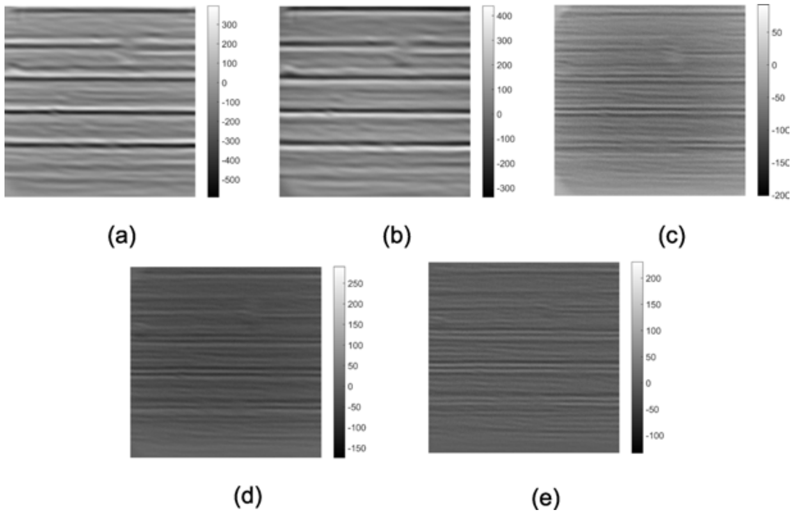

Figure 2.7: (a)-(e): EFF 1-5 of the aluminum peroxide dataset, respectively.

degraded by horizontal stripes over the whole width of the projection. In contrast, dynamic FFC is able to remove most of the flat field variation related artifacts if sufficient (i.e., two or more) EFFs are used to correct the projections. Parallel analysis of the dataset suggests the use of 3 EFFs.

Inspection of the conventional FFC corrected sinogram (see Figure 2.9 for a selection of the sinogram) reveals vertical stripes over the full width of the sinograms. The intensity of these stripes were observed to vary randomly between consecutive projections. This line pattern is completely removed using dynamic FFC. The difference (see Figure 2.9) between the two methods is up to 4% of the signal. On the FBP reconstructed slices, however, the difference between conventional and dynamic FFC is less obvious (see Figure 2.10). The variations resulting from conventional FFC are almost randomly distributed with respect to the projection angle. During the back projection these variations are averaged out (in each voxel). Hence, while there are often large errors in the projections cause by incorrect FFC, only a limited effect can be observed in the reconstructions due to the back projection averaging effect. If more than 3 EFFs are used, the reconstructions are corrupted by small ring artifacts. This result can be explained by the low SNR of high order EFFs, introducing systematic errors in the dynamic flat field corrected projections. Parallel analysis was able to exclude these noisy EFFs by selecting only 3 EFFs.

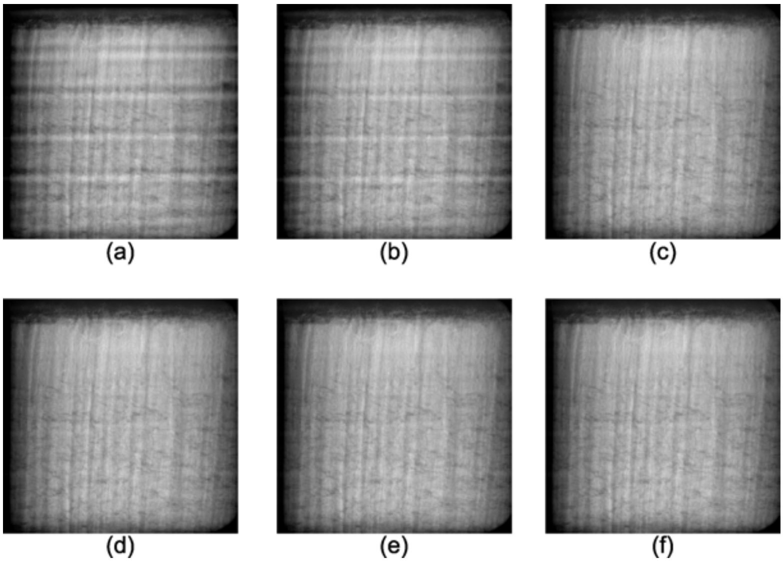

Figure 2.8: An FFC corrected projection from the aluminum peroxide dataset: (a) conventional FFC, (b)-(f) dynamic FFC with 1 to 5 EFFs, respectively.

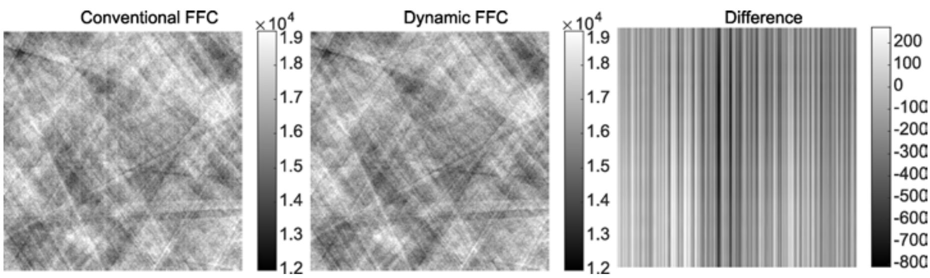

Figure 2.9: ROI of the aluminum peroxide sinogram: (a) conventional FFC, (b) dynamic FFC with 3 EFFs. (c) The difference between the conventional and dynamic flat field corrected sinogram.

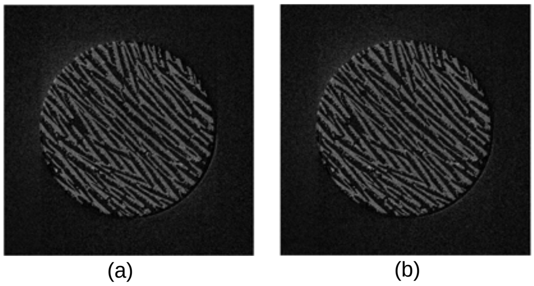

Figure 2.10: FBP reconstructed slice of the aluminum peroxide dataset with (a) conventional and (b) dynamic FFC with 3 EFFs.

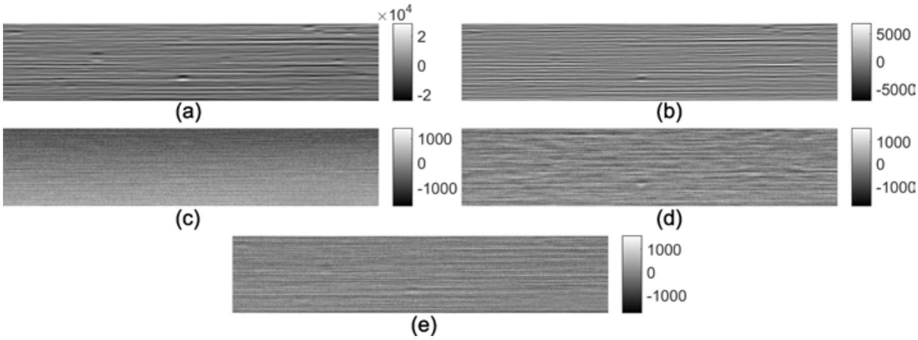

Figure 2.11: (a)-(e): The first five (principal) EFFs of the foam dataset.

2.4.2.2 Foam

Figure 2.11 shows the first five EFFs of the foam dataset. These EFFs show structural patterns and not only variation due to noise, as would be expected in the stationary flat field case. Accordingly, visual inspection of the flat fields reveals clear variation of the flat fields over time. An up and down motion of the flat field pattern is observed in an almost periodical manner. The period of this motion is only a few projections long, which is fast compared to the duration of the full scan. The structural patterns are mainly horizontal stripes originating from the up and down motion of the pattern as can be seen in the mean flat field (Figure 2.4). Higher order EFFs are highly degraded by noise, a consequence of the noise being responsible for a part of the variation of the flat fields.

A corrected projection with conventional and dynamic FFC (with 1 to 5 EFFs) is shown in Figure 2.12. Most projections in the dataset still show substantial artifacts after conventional FFC. In contrast, dynamic FFC greatly improves the projections. Using a single EFF has only a limited effect, but two or more EFFs

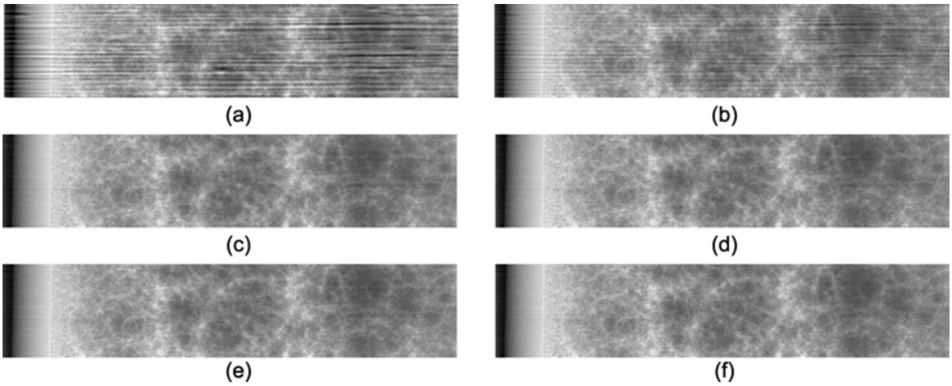

Figure 2.12: An FFC corrected projection from the foam dataset: (a) conventional FFC, (b)-(f) dynamic FFC with 1 to 5 EFFs, respectively.

reduce the patterns due to flat field variation almost completely. The difference between the two methods is up to 30% of the signal.

Figure 2.13(a) and Figure 2.13(b-f) show the sinogram of a slice with conventional and dynamic FFC, respectively. The conventionally corrected sinogram clearly shows remaining artifacts (indicated by the arrows). These artifacts are substantially reduced if sufficient, i.e. more than two EFFs, are taken into account. Parallel analysis of this dataset suggests that 5 EFFs should be used. Note that, although the estimation procedure is only dependent on the spatial TV, the smoothness of the sinogram indicates a decreased TV in the temporal direction.

Figure 2.14 and Figure 2.15 show a reconstructed slice with both conventional and dynamic flat field corrected projections. The images in 2.14 and Figure 2.15 are reconstructed with SIRT and FBP, respectively. Many of the SIRT reconstructed volume slices show only small changes, but some images that were reconstructed after conventional FFC are strongly degraded by broad ring artifacts caused by dynamic flat field variations. The positions of these ring artifacts correspond with the variable flat field induced artifacts in the sinograms, revealing that these ring artifacts are indeed a direct consequence of flat field variations. Dynamic FFC is able to remove these artifacts, resulting in a homogeneous background of the reconstructed slice. The FBP reconstructions in Figure 2.15 are more severely degraded with noise in comparison with the SIRT reconstructions. Nevertheless, the reconstructions show the same flat field related artifacts as the SIRT reconstructions. As both FBP and SIRT are characterized by a back projection step, which is responsible for the relatively small improvement in the reconstruction, the difference between these reconstruction algorithms is small. The attenuation of the foam is low in comparison to the attenuation of the aluminum peroxide sam-

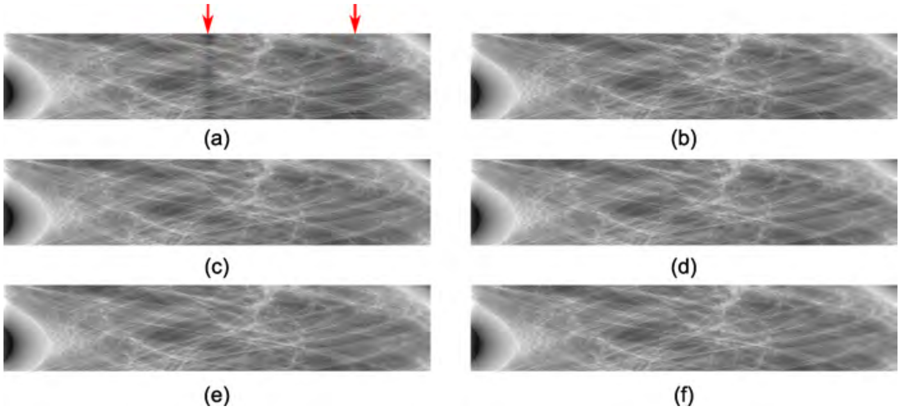

Figure 2.13: Sinogram of a slice of the foam dataset: (a) conventional FFC, (b)-(f) dynamic FFC with 1 to 5 EFFs, respectively. Bands containing artifacts are indicated with red arrows.

ple (section 2.4.2.1). Consequently, the flat field variations are bigger relative to the attenuation signal, causing more pronounced artifacts in the reconstructions. Therefore, it is to be expected that dynamic FFC will have the largest impact on low attenuating samples.

2.4.3 General remarks

In current X-ray imaging in which conventional FFC is employed, a set of flat fields is typically acquired prior to and/or after the object scan. Since our proposed dynamic FFC method captures the variability within a set of flat fields, it is indirectly assumed that the variation in flat fields during the object scan is well represented by the variation in the pre/post flat fields. Note that this is not a limitation of the method itself, since intermittent flat fields acquired during the scan may also be used. However, acquiring flat fields during the experiment involves removing the sample during the scan and placing it back at the exact same position after the flat field was acquired, which is technically very challenging. Moreover, this would substantially prolong the scan time and may also introduce motion artifacts. The number of flat fields that are typically acquired is also often limited to a few tens of images, mainly to increase the SNR of the (conventionally averaged) flat field. In the proposed dynamic FFC procedure, a small number of EFFs are used to normalize the projections. However, since the SNR of these components decreases with increasing order of the EFF, more flat fields are needed to yield a sufficient SNR compared to conventional FFC. Fortunately, the acquisition of more flat fields is typically not a time consuming procedure, certainly not at synchrotron facilities where short exposure times are used.

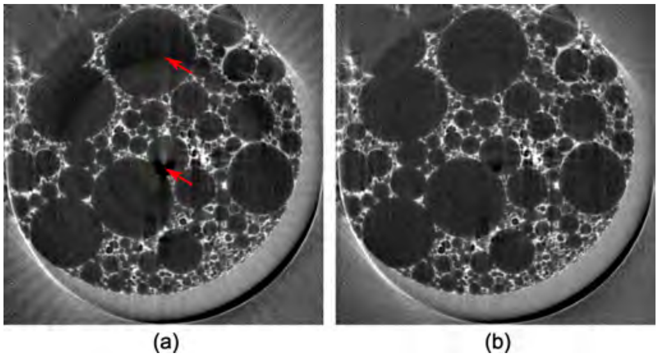

Figure 2.14: SIRT reconstruction of a slice (same slice as in Figure 2.13) of the foam dataset: (a) conventional FFC, (b) dynamic FFC with 5 EFFs. The broad ring artifacts are indicated with red arrows and correspond to the artifacts indicated on the sinograms (see Figure 2.13)

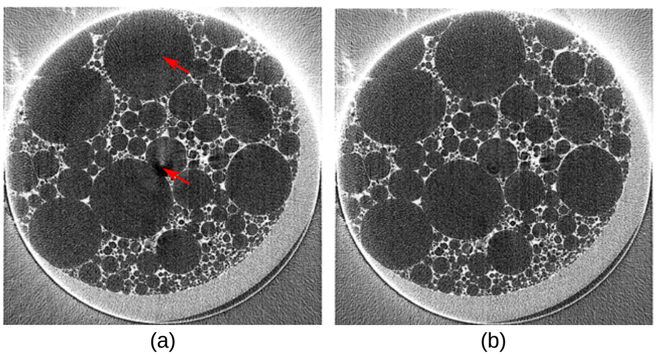

Figure 2.15: FBP reconstruction of a slice (same slice as in Figure 2.13) of the foam dataset: (a) conventional FFC, (b) dynamic FFC with 5 EFFs. The broad ring artifacts are indicated with red arrows and correspond to the artifacts indicated on the sinograms (see Figure 2.13)

The speed of the method mainly depends on the number of projections, the size of the projections and the number of used EFFs. Estimation of the EEF coefficients $\{\hat{w}_{jk}\}$ is the most time consuming part of our technique, due to the gradient which has to be calculated for each objective function evaluation. As an example, dynamic FFC of the aluminum peroxide dataset (See section 2.4.2.1) with 3 EFFs took around one second for every 2048×2048 projection.

2.5 Conclusion

Flat field variability is a wide spread phenomenon in X-ray imaging data acquired at synchrotron facilities. Conventional FFC does not account for temporal variations in the flat fields, resulting in systematic errors in the corrected projections. Dynamic FFC deals with this problem by estimation of a corresponding flat field for every projection. Validation of the technique on a software phantom showed that dynamic FFC improves both the projections and the reconstructions with respect to conventional FFC. Experiments on two different synchrotron datasets showed that the proposed method is able to estimate the flat fields and obtain normalized projections with strongly diminished or removed flat field variability related artifacts.

References

[1] L. Tlustos, M. Campbell, E. Heijne, and X. Llopart, "Signal variations in high-granularity Si pixel detectors," *IEEE Trans. Nucl. Sci*, vol. 51, pp. 3006–3012, Dec. 2004.

[2] J. Sijbers and A. Postnov, "Reduction of ring artefacts in high resolution micro-CT reconstructions.," *Phys. Med. Biol.*, vol. 49, no. 14, pp. N247–N253, 2004.

[3] M. Boin and A. Haibel, "Compensation of ring artefacts in synchrotron tomographic images.," *Opt. Express*, vol. 14, no. 25, pp. 12071–12075, 2006.

[4] B. Münch, P. Trtik, F. Marone, and M. Stampanoni, "Stripe and ring artifact removal with combined waveletâĂŤFourier filtering," *Opt. Express*, vol. 17, pp. 8567–8591, May 2009.

[5] J. Baek, B. De Man, D. Harrison, and N. J. Pelc, "Raw data normalization for a multi source inverse geometry CT system," *Opt. Express*, vol. 23, no. 6, pp. 7514–7526, 2015.

[6] S. R. Stock, *MicroComputed Tomography: Methodology and Applications.* CRC, 2008.

[7] R. Tucoulou, G. Martinez-Criado, P. Bleuet, I. Kieffer, P. Cloetens, S. Labouré, T. Martin, C. Guilloud, and J. Susini, "High-resolution angular beam stability monitoring at a nanofocusing beamline," *J. Synchrotron Radiat.*, vol. 15, pp. 392–398, 2008.

[8] V. Titarenko, S. Titarenko, P. J. Withers, F. De Carlo, and X. Xiao, "Improved tomographic reconstructions using adaptive time-dependent intensity normalization.," *J. Synchrotron Radiat.*, vol. 17, pp. 689–699, Sept. 2010.

[9] J. M. Bauer, J. C. Liu, A. A. Prinz, and S. H. Rokni, "Experiences from first top-off injection at the stanford synchrotron radiation lightsource," in *5th International Workshop on Radiation Safety at Synchrotron Radiation Sources*, 2009.

[10] S. E. Park, J. G. Kim, M. A. A. Hegazy, M. H. Cho, and S. Y. Lee, "A flat-field correction method for photon-counting-detector-based micro-CT," *Proc. SPIE Medical Imaging 9033, 90335*, 2014.

[11] I. Jolliffe, *Principal Component Analysis.* Springer, 2nd ed., 2002.

[12] L. I. Rudin, S. Osher, and E. Fatemi, "Nonlinear total variation based noise removal algorithms," *Phys. D*, vol. 60, pp. 259–268, Nov. 1992.

[13] M. Turk and A. Pentland, "Eigenfaces for recognition," *J. Cognitive Neurosci.*, vol. 3, pp. 71–86, 1991.

[14] R. B. Cattell, "The scree test for the number of factors," *Multivar. Behav. Res.*, vol. 1, pp. 245–276, 1966.

[15] S. B. Franklin, D. J. Gibson, P. A. Robertson, J. T. Pohlmann, and J. S. Fralish, "Parallel analysis: a method for determining significant principal components," *J. Veg. Sci.*, vol. 6, no. 1, pp. 99–106, 1995.

[16] K. Dabov and A. Foi, "Image denoising with block-matching and 3D filtering," *Proc. SPIE Electronic Imaging 6064, 6064A-30*, 2006.

[17] D. F. Shanno, "Conditioning of quasi-Newton methods for function minimization," *Math. Comput.*, vol. 24, no. 111, pp. 647–656, 1970.

[18] F. Natterer, *The Mathematics of Computerized Tomography.* Society for Industrial and Applied Mathematics, 2001.

[19] W. J. Palenstijn, K. J. Batenburg, and J. Sijbers, "Performance improvements for iterative electron tomography reconstruction using graphics processing units (GPUs)," *J. Struct. Biol.*, vol. 176, no. 2, pp. 250–253, 2011.

[20] W. van Aarle, W. J. Palenstijn, J. De Beenhouwer, T. Altantzis, S. Bals, K. J. Batenburg, and J. Sijbers, "The ASTRA toolbox: a platform for advanced algorithm development in electron tomography," *Ultramicroscopy*, vol. 157, pp. 35–47, 2015.

[21] A. Buades and B. Coll, "A non-local algorithm for image denoising," in *Computer vision and pattern recognition*, vol. 2, pp. 60–65, 2005.

3

Affine deformation estimation and correction in cone beam computed tomography

Contents

3.1 Introduction 56
3.2 Method 57
3.2.1 Definitions 57
3.2.2 Affine transformation and cone beam projections 58
3.2.3 Estimation of motion/deformation parameters 59
3.3 Experiments 65
3.3.1 Phantom study 65
3.3.2 Real data 68
3.4 Results and discussion 69
3.4.1 Phantom study 69
3.4.2 Real data 72
3.4.3 4D reconstructions 76
3.4.4 Medical applications 76
3.5 Conclusion 76
3.6 Appendix 77
References 78

This chapter has been published as:
V. Van Nieuwenhove, J. De Beenhouwer, T. De Schryver, L. Van Hoorebeke, and J. Sijbers, *"Data-Driven Affine Deformation Estimation and Correction in Cone Beam Computed Tomography"*, IEEE Transactions on Image Processing, vol. 26, no. 3, pp. 1441-1451, 2017.

3.1 Introduction

As mentioned in Section 1.3.3, an effective way to reduce motion artefacts in CT is to simply reduce the scan time to limit (the risk of) sample deformation during the acquisition [1, 2]. Faster scanning, however, inevitably leads to reduced signal-to-noise ratio (SNR) of the reconstructed images. Especially in micro-CT imaging, where the X-ray flux is much smaller compared to clinical CT, scan times of the order of hours are common to obtain sufficient SNR and spatial resolution. Hence, many micro-CT experiments suffer from a high risk of sample motion/deformation during the acquisition, which significantly reduces the spatial resolution of the reconstructed images. Hence, there is a clear need for reconstruction methods that can generate high quality images from motion corrupted scans.

In this chapter a data driven deformation correction (see Section 1.3.3) reconstruction algorithm for affine deformations is proposed. Data driven motion/deformation estimation methods that only rely on data acquired during a single gantry rotation have been proposed. Most of these techniques, however, assume 2D parallel or fan beam projections [3, 4]. For example, the effect of affine transformations on the 2D radon transform was studied in [5, 6, 7, 8]. Frysch et al. estimated rigid motion directly on cone beam projection images [9, 10]. A fan beam and cone beam motion correction without deformation model was proposed by Leng et al. [11]. It estimates a motion corrected version of the motion contaminated projections based on the rest of the projections. However, this method assumes that a large portion of the projections are not corrupted by motion.

In this chapter, we introduce a 3D estimation and correction algorithm for global affine deformation, which works directly on the cone beam projections. The correction of the affine deformation is achieved by exploiting the relationship between cone beam projections and affine transformations. To estimate the affine deformation parameters, a data driven approach is proposed that estimates the deformation parameters of each individual cone beam projection with respect to a fast reference scan. The estimation of the deformation parameters is performed directly in the projection domain, avoiding time consuming reconstructions. To achieve this, an inconsistency criterion, based on the exact reconstruction algorithm of Grangeat [12, 13], is minimized by a non-convex optimization procedure. A similar inconsistency criterion was recently introduced to compensate for rigid motion [9, 14, 15, 16, 17].

This chapter is organized as follows. Some definitions are introduced in Section 3.2.1. Section 3.2.2 describes the relation between the cone beam projections and affine transformations which allows to correct for affine deformations directly in the projection domain. Next, a method to estimate affine deformation parameters directly in the projection domain is proposed. Section 3.3 describes phantom and real data experiments, the results of which are presented in Section 3.4. Section 3.5 concludes the chapter.

3.2 Method

3.2.1 Definitions

3.2.1.1 Cone beam geometry

In X-ray CT, each acquired projection is associated with a projection geometry: the source position $\mathbf{s}$ and the position of the individual detector elements. The detector is assumed to be rectangular and flat with the detector center at position $\mathbf{d}_c$. The position $\mathbf{m}_{ij}$ of the detector element at detector coordinates (i, j) can then be described as: $\mathbf{m}_{ij} = \mathbf{d}_c + i \cdot \mathbf{d}_1 + j \cdot \mathbf{d}_2$, with $\mathbf{d}_1$ being the 3D vector from detector element (0,0) to (1,0), $\mathbf{d}_2$ the 3D vector from detector element (0,0) to (0,1), $i \in [-I/2, I/2]$ and $j \in [-J/2, J/2]$, where I and J are the number of detector pixels horizontally and vertically, respectively. The projection geometry of a single projection can thus be described with the following set of vectors $G = \{\mathbf{s}, \mathbf{d}_c, \mathbf{d}_1, \mathbf{d}_2\}$.

For each ray, two planes can be defined that both contain the vector $\mathbf{m}_{ij} - \mathbf{s}$ and are parallel to $\mathbf{d}_1$ or $\mathbf{d}_2$.

The normals to these planes, $\mathbf{n}_1(j)$ and $\mathbf{n}_2(i)$, are given by:

$$
\begin{aligned}
\mathbf{n}_1(j) &= \frac{(\mathbf{m}_{ij} - \mathbf{s}) \times \mathbf{d}_1}{\| (\mathbf{m}_{ij} - \mathbf{s}) \times \mathbf{d}_1 \|} \\
\mathbf{n}_2(i) &= \frac{(\mathbf{m}_{ij} - \mathbf{s}) \times \mathbf{d}_2}{\| (\mathbf{m}_{ij} - \mathbf{s}) \times \mathbf{d}_2 \|},
\end{aligned}
\tag{3.1}
$$

with $\|.\|$ denoting the Euclidean norm (2-norm). A cone beam projection of a function $f(\mathbf{x})$ ($\mathbf{x} \in \mathbb{R}^3$) can then be described as:

$$
C_G(f(\mathbf{x}), i, j) = \int f(\mathbf{x}) \delta \left(\mathbf{n}_1(j) \cdot (\mathbf{x} - \mathbf{s})\right) \delta \left(\mathbf{n}_2(i) \cdot (\mathbf{x} - \mathbf{s})\right) d\mathbf{x}. \tag{3.2}
$$

The overall geometry is visualized in Figure 3.1. During a CT acquisition, multiple projections are acquired, each corresponding to a specific source and detector position.

3.2.1.2 Affine transformation

An affine transformation is a combination of translations, rotations, differential scalings and shearings. An affine transformed volume $f_T(\mathbf{x})$ of $f(\mathbf{x})$ can be calcu-

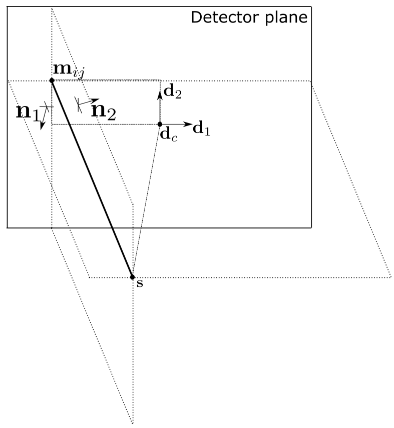

Figure 3.1: Schematic overview of the geometry of a cone beam projection.

lated as follows:

$$f_T(\mathbf{x}) = f(\mathbf{A}\mathbf{x} + \mathbf{u}), \tag{3.3}$$

where $\mathbf{A}$ is a 3×3 linear map and $\mathbf{u}$ a 3×1 vector describing translation.

3.2.2 Affine transformation and cone beam projections

The effect of an affine transformation on the 2D Radon transform has been well studied [5, 6, 7]. In this section, we will elaborate on the extension to cone beam projections.

Let $C_G(f_T(\mathbf{x}), i, j)$ be a cone beam projection of an affine transformed object $f_T(\mathbf{x})$ associated with the projection geometry G. Then, $C_G(f_T(\mathbf{x}), i, j)$ can be transformed to a cone beam projection of the non-deformed object $f(\mathbf{x})$, as follows (proof in Appendix):

$$C_{G'}(f(\mathbf{x}), i, j) = \frac{\|(\mathbf{A}^{-1})^T \mathbf{n}_1(j)\| \|(\mathbf{A}^{-1})^T \mathbf{n}_2(i)\|}{\det(\mathbf{A}^{-1})} C_G(f_T(\mathbf{x}), i, j), \tag{3.4}$$

associated with virtual projection geometry $G' = \{\mathbf{s}', \mathbf{d}'_c, \mathbf{d}'_1, \mathbf{d}'_2\}$, where:

$$\begin{cases} \mathbf{s}' & = \mathbf{A}\mathbf{s} + \mathbf{u} \\ \mathbf{d}'_c & = \mathbf{A}\mathbf{d}_c + \mathbf{u} \\ \mathbf{d}'_1 & = \mathbf{A}\mathbf{d}_1 \\ \mathbf{d}'_2 & = \mathbf{A}\mathbf{d}_2 \end{cases} \tag{3.5}$$

If all projections of a CT dataset are transformed to be consistent with projections of the non-deformed object, then a 3D image that is free of motion artefacts can be reconstructed.

3.2.3 Estimation of motion/deformation parameters

In Section II-B, a procedure was described to correct a cone beam projection of an affine transformed object, which requires knowledge of that affine transformation. In a real experiment, the deformation parameters are unknown and need to be estimated from the measured projection data. In this section, an approach to automatically estimate the affine deformation parameters is introduced.

The section starts with the general data acquisition and estimation strategy (section 3.2.3.1) followed by the concept of redundantly measured planes (section 3.2.3.2). Based on this concept, an objective function is derived in section 3.2.3.3. Finally, a strategy to optimize this objective function is introduced.

3.2.3.1 Estimation strategy

To ensure accurate deformation estimation, we propose the following acquisition protocol. The complete acquisition consists of two parts:

Main scan: Conventional scan with N projections.

Reference scan: A short 360° equiangular scan with N_{ref} projections ($N_{ref} \ll N$) that is acquired immediately before or after the main scan (see Figure 3.2a). Reference projections in multiple directions are required in order to estimate the deformation parameters of projections, of the main scan, in different directions. During the reference scan, the object is assumed to be motionless, which is a reasonable assumption since this scan is acquired in a very short time span. Reference scans have a limited extra cost and are often already implemented in commercial high resolution micro-CT scanners [18]. In practice, an angular step of 45° was observed to be sufficient.

For each projection of the main scan, an affine deformation has to be estimated with respect to the reference scan. Affine deformation parameters corresponding to a certain projection of the main scan can be estimated by minimizing a criterion that quantifies the inconsistency between that projection and all projections of the reference scan.

Unfortunately, not all affine parameters corresponding to a single projection can be accurately estimated. For example, a translation in the projection direction (i.e., parallel to $\mathbf{d}_c - \mathbf{s}$) will be almost indistinguishable from a scaling of the object. To overcome this problem, only parameters that describe deformations perpendicular to the projection direction will be estimated. To that end, we introduce a change of the coordinate system for the current projection. The coordinate system is rotated to align the projection direction $\mathbf{d}_c - \mathbf{s}$ with one of the coordinate axes. This is achieved by multiplying the vectors associated with projection geometry G with a rotation matrix $\mathbf{R}$. Here, without loss of generality, the projection direction is rotated such that it becomes parallel to the y-axis. Hence, $\mathbf{R}$ is written as:

$$\mathbf{R} = \mathbf{R}_x \mathbf{R}_z, \tag{3.6}$$

with $\mathbf{R}_x$ and $\mathbf{R}_z$ a rotation around the x-axis and z-axis, respectively:

$$\begin{aligned} \mathbf{R}_x &= \begin{bmatrix} 1 & 0 & 0 \\ 0 & \cos\theta & \sin\theta \\ 0 & -\sin\theta & \cos\theta \end{bmatrix} \\ \mathbf{R}_z &= \begin{bmatrix} \cos\phi & \sin\phi & 0 \\ -\sin\phi & \cos\phi & 0 \\ 0 & 0 & 1 \end{bmatrix}, \end{aligned} \tag{3.7}$$

where the angles θ and ϕ are given by (see Figure 3.2b):

$$\begin{aligned} \theta &= \operatorname{sgn}(d_{c,z} - s_z) \arccos\left(\frac{\sqrt{(d_{c,x} - s_x)^2 + (d_{c,y} - s_y)^2}}{\|\mathbf{d}_c - \mathbf{s}\|} \right) \\ \phi &= \arctan\left(\frac{d_{c,x} - s_x}{d_{c,y} - s_y} \right). \end{aligned} \tag{3.8}$$

with sgn the sign function, arctan the four-quadrant inverse tangent and $d_{c,\cdot}$ and $s_\cdot$ the components of the vector $\mathbf{d}_c$ and $\mathbf{s}$, respectively.

Hence, the projection geometry in the rotated coordinate system is given by:

$$G_\mathbf{R} = \{\mathbf{s}_\mathbf{R}, \mathbf{d}_{c,\mathbf{R}}, \mathbf{d}_{1,\mathbf{R}}, \mathbf{d}_{2,\mathbf{R}}\} = \{\mathbf{R}\mathbf{s}, \mathbf{R}\mathbf{d}_c, \mathbf{R}\mathbf{d}_1, \mathbf{R}\mathbf{d}_2\}. \tag{3.9}$$

The subscript $\cdot_\mathbf{R}$ denotes that the variable is expressed in the rotated coordinate system. The affine deformation in the rotated coordinate system is given by:

$$\{\mathbf{A}_\mathbf{R}, \mathbf{u}_\mathbf{R}\} = \{\mathbf{R}\mathbf{A}\mathbf{R}^{-1}, \mathbf{R}\mathbf{u}\}. \tag{3.10}$$

The rotation of the coordinate system allows extracting parameters that describe deformations perpendicular to the projection axis (i.e., the y-axis). Let $\mathbf{q}_k$ denote the set of parameters in the rotated coordinate system characterizing the deformation of projection k perpendicular to the y-axis:

$$\mathbf{q}_k = \begin{bmatrix} a_{\mathbf{R},x,x} & a_{\mathbf{R},x,z} & a_{\mathbf{R},z,x} & a_{\mathbf{R},z,z} & u_{\mathbf{R},x} & u_{\mathbf{R},z} \end{bmatrix}^T, \tag{3.11}$$

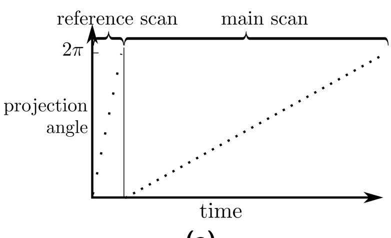

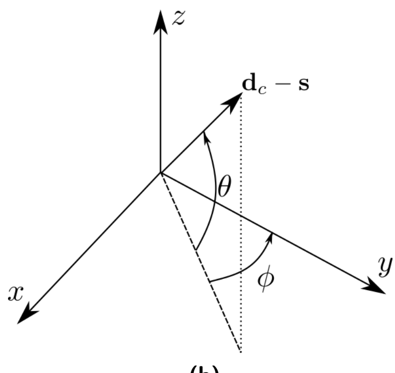

Figure 3.2: (a) Acquisition protocol: A short reference scan followed by the main scan. The order of both scans can be changed. (b) The angles θ and ϕ that define the rotation of the coordinate system.

with $a_{\mathbf{R},\cdot,\cdot}$ an element of the matrix $\mathbf{A_R}$ and $u_{\mathbf{R},\cdot}$ an element of the vector $\mathbf{u_R}$. For each projection k, the parameters of the vector $\mathbf{q}_k$ are estimated by minimizing an objective function F_k that quantifies the inconsistency of the k^{th} projection with respect to the reference scan:

$$\mathbf{q}_k^* = \arg\min_{\mathbf{q}_k} F_k(\mathbf{q}_k). \tag{3.12}$$

The proposed objective function will be derived in Section 3.2.3.3.

3.2.3.2 Redundantly measured planes

During the reference and the main scan, many planes are scanned twice. All planes that are sampled by the k^{th} ($k = 1, \ldots, N$) projection of the main scan and the l^{th} ($l = 1, \ldots, N_{ref}$) projection of the reference scan contain the source positions $\mathbf{s}_k$ and $\mathbf{s}_l$. These two points define a line $\mathbf{s}_l + \alpha(\mathbf{s}_k - \mathbf{s}_l)$ with $\alpha \in \mathbb{R}$ that defines the sheaf of all planes that are sampled by both projections.

The point $\mathbf{c}_{k,l} = \mathbf{d}_{c,k} + i_{k,l}\mathbf{d}_{1,k} + j_{k,l}\mathbf{d}_{2,k}$, where the line $\mathbf{s}_l + \alpha(\mathbf{s}_k - \mathbf{s}_l)$ intersects with the detector plane k, can be calculated by solving the following system of equations for $i_{k,l}$, $j_{k,l}$ and α_k:

$$\begin{bmatrix}\mathbf{d}_{1,k} & \mathbf{d}_{2,k} & (\mathbf{s}_k - \mathbf{s}_l)\end{bmatrix} \begin{bmatrix} i_{k,l} \\ j_{k,l} \\ -\alpha_k \end{bmatrix} = \mathbf{s}_l - \mathbf{d}_{c,k}, \tag{3.13}$$

with α_k the value of the parameter α where the line intersects with the detector

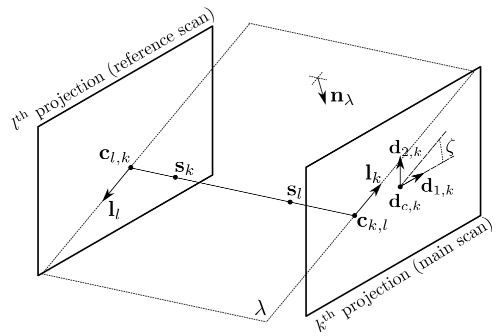

Figure 3.3: The parameters of a plane sampled by both the k^{th} main and the l^{th} reference projection.

plane. The same procedure can be repeated to calculate $\mathbf{c}_{l,k}$, the point where the line $\mathbf{s}_l + \alpha(\mathbf{s}_k - \mathbf{s}_l)$ intersects with the detector plane l.

Let λ be a plane sampled by both the k^{th} main projection and a reference projection. The projection of λ on the main projection then corresponds to a line defined by $\mathbf{c}_{k,l}$ and a unit vector $\mathbf{l}_k(\zeta) = \cos(\zeta)\frac{\mathbf{d}_{1,k}}{\|\mathbf{d}_{1,k}\|} + \sin(\zeta)\frac{\mathbf{d}_{2,k}}{\|\mathbf{d}_{2,k}\|}$ in the detector plane (with ζ the angle between $\mathbf{l}_k$ and $\mathbf{d}_{1,k}$).

As a result, any plane, sampled by both the main and the reference projection, is parametrized by the angle ζ.

The vector $\mathbf{l}_l$, describing the projection of the plane on the l^{th} reference detector, should lie in the same plane as $\mathbf{l}_k$. Hence, $\mathbf{l}_l$ can be determined as follows:

$$\mathbf{l}_l(\zeta) = \frac{1}{Z}\left((\mathbf{d}_{1,l} \times \mathbf{d}_{2,l}) \times \mathbf{n}_\lambda\right), \tag{3.14}$$

with $\mathbf{n}_\lambda(\zeta) = \frac{1}{Z'}\mathbf{l}_k(\zeta) \times (\mathbf{s}_l - \mathbf{s}_k)$, the normal to the plane and Z and Z' normalization constants. A graphical overview of the geometry of a plane sampled by the k^{th} projection of the main scan and the l^{th} projection of the reference scan is shown in Figure 3.3.

The angular range of ζ for which the corresponding planes have an actual intersection with the detector support of two projections is highly dependent on the direction of the projections. If two projections lie approximately opposite to each other, the point $\mathbf{c}_{k,l}$ lies on the detector. As a result, all planes, sampled by both the main and the reference projection, have an actual intersection with the detector support. On the other hand, if the directions of the two projections are approximately the same, only a small angular range of ζ will correspond to planes intersecting with the actual detector support. A more in depth discussion can be found in [17].

3.2.3.3 Objective function

To assess the consistency of a projection with the reference scan, a cone beam inconsistency criterion is defined that is based on redundantly measured planes (see Section 3.2.3.2). The inconsistency criterion is based on the exact cone beam reconstruction method of Grangeat and compares the derivative of the 3D Radon transform of redundantly measured planes in the reconstruction domain directly on the projections [12, 13]. As such, it avoids computationally intensive reconstructions to evaluate the estimated deformation parameters. The optimization of this criterion was proposed in several recent techniques to estimate rigid motion and geometric system parameters [14, 17, 9, 15, 19]. Although the criterion is theoretically restricted to non-truncated data, it has been successfully applied to truncated data as well [15, 19]. The connection with the epipolar geometry was established in [17, 16].

A plane λ, sampled by a projection associated with projection geometry G, containing the source position $\mathbf{s}$ and a point on the detector $\mathbf{m}_{ij}$ is projected as a line on the detector: $\mathbf{y}(v) = v\mathbf{l}(\zeta) + \mathbf{m}_{ij}$. From the data on this line, the value of the radial derivative of the 3D Radon transform corresponding to the plane λ can be calculated as follows:

1. In the first step, the projection undergoes an inverse cosine weighting, similar to the well-known Feldkamp, David and Kress (FDK) algorithm [13, 20]:

$$E(C_G, i, j) = \frac{C_G(f(\mathbf{x}), i, j)}{|\mathbf{w} \cdot \mathbf{t}(i, j)|}, \tag{3.15}$$

with $\mathbf{t}(i, j) = \frac{1}{Z}(\mathbf{m}_{ij} - \mathbf{s})$ the unit vector in the direction of the ray intersecting a detector element at position (i, j) on the projection with projection geometry G and $\mathbf{w} = \frac{1}{Z'}\mathbf{d}_1 \times \mathbf{d}_2$ the normal to the detector. Z and Z' are normalization constants.

2. In the second step, the cone beam projections are integrated along the projection of the plane ($\mathbf{y}(v) = v\mathbf{l}(\zeta) + \mathbf{m}_{ij}$):

$$L(C_G, i, j, \mathbf{l}) = \int_{-\infty}^{+\infty} E\left(C_G, i + v\mathbf{l} \cdot \mathbf{d}_1, j + v\mathbf{l} \cdot \mathbf{d}_2\right) dv. \tag{3.16}$$

3. Finally, a differentiation in the direction perpendicular to $\mathbf{l}$ is performed, resulting in the radial derivative of the 3D radon transform of the scanned object:

$$H(C_G, i, j, \mathbf{l}) = \nabla_{\mathbf{r}} L(C_G, i, j, \mathbf{l}), \tag{3.17}$$

with $\mathbf{r} = (\mathbf{w} \times \mathbf{l})/\|\mathbf{w} \times \mathbf{l}\|$. The radial derivative is approximated with the central difference method.

The domain of the radial derivative of the 3D radon transform can only partially be calculated since only a limited set of planes in the reconstruction domain is sampled; that is, only planes that are sampled by the cone beam, defined by projection geometry G, are sampled. Since the goal of the objective function is to compare planes that are sampled by the k^{th} projection of the main scan and l^{th} projection of the reference scan, only the planes containing the point $\mathbf{c}_{k,l}$ will be considered: $H(C_{G_k}, i_{k,l}, j_{k,l}, \mathbf{l}) = H(C_{G_k}, \mathbf{c}_{k,l}, \mathbf{l})$. The value of the derivative of the 3D radon transform corresponding to a plane calculated on two different projections should be the same. As a result, the difference between these derivatives should, theoretically, be zero. An intermediate inconsistency function $T_{k,l}$ is defined by repeating this procedure for different planes, which are all elements of the sheaf of planes defined by the line $\mathbf{s}_l + \alpha(\mathbf{s}_k - \mathbf{s}_l)$:

$$\begin{aligned} T_{k,l}(\mathbf{q}_k) = \sum_{\{\mathbf{l}_k(\zeta):\zeta\in[0,\pi)\}} & [H(C'_{G_{\mathbf{R},k}}(\mathbf{q}_k), \mathbf{c}_{k,l}(\mathbf{q}_k), \mathbf{l}_k) \\ & - H(C_{G_{\mathbf{R},l}}, \mathbf{c}_{l,k}(\mathbf{q}_k), \mathbf{l}_l(\mathbf{q}_k))]^2, \end{aligned} \tag{3.18}$$

with:

$$\begin{aligned} & C'_{G_{\mathbf{R},k}}(\mathbf{q}_k, i, j) = \\ & \frac{\|(\mathbf{A}(\mathbf{q_k})^{-1})^T \mathbf{n}_1(j)\| \|(\mathbf{A}(\mathbf{q_k})^{-1})^T \mathbf{n}_2(i)\|}{\det(\mathbf{A}(\mathbf{q_k})^{-1})} C_{G_{\mathbf{R},k}}(f_T(\mathbf{x}), i, j). \end{aligned} \tag{3.19}$$

The first term of the intermediate inconsistency function Eq. 3.18 is the derivative of the 3D radon transform corresponding to the plane, sampled by both projections, calculated on an affine deformation corrected projection of the main scan. The second term is the derivative of the 3D radon transform corresponding to the same plane calculated on a projection of the reference scan. The points $\mathbf{c}_{l,k}$ and $\mathbf{c}_{k,l}$ and the vector $\mathbf{l}_l$ are calculated with the geometries $G'_{\mathbf{R},k}$ and $G_{\mathbf{R},l}$. The sum in Eq. 3.18 runs over a set of unit vectors $\mathbf{l}_k(\zeta)$ with ζ equiangular sampled over $[0, \pi)$. The number of samples of ζ indicates how many planes are checked for consistency between every pair of projections.

To quantify the inconsistency, the deformation corrected projection is compared with all projections of the reference scan. This results in the following objective function:

$$F_k(\mathbf{q}_k) = \left(\Sigma_{l=1}^{N_{ref}} T_{k,l}(\mathbf{q}_k)\right)^{\frac{1}{2}}. \tag{3.20}$$

3.2.3.4 Optimization

The objective function in Eq. 3.20 is minimized using a non-linear optimization algorithm:

$$\mathbf{q}_k^* = \arg\min_{\mathbf{q}_k} F_k(\mathbf{q}_k). \tag{3.21}$$

Here, a Sequential Quadratic Programming (SQP) non-linear optimization algorithm was used [21]. This procedure is terminated when the number of iterations exceeds t_{max} or if the relative decrease ε of F_k between two consecutive iterations is below a fixed tolerance, ε_{min}. These stopping criteria were chosen to be: $\varepsilon_{min} = 10^{-4}$ and $t_{max} = 1000$. A schematic overview is shown in Figure 3.4. To avoid local minima, a multi scale approach was applied. To reduce the computational complexity of the algorithm, Eq. 3.4 was approximated as follows

$$C_{G'}(f(\mathbf{x}), i, j) \approx C_G(f_T(\mathbf{x}), i, j), \tag{3.22}$$

which is approximately valid for small affine deformations.

After the deformation estimation and correction of all projections, the volume is reconstructed at the time of the reference scan. The algorithm was implemented in Matlab, with major parts of the code computed on the Graphics Processing Unit (GPU) using the parallel computing toolbox.

3.3 Experiments

The proposed affine deformation estimation and correction technique was validated on both simulated and real data.

3.3.1 Phantom study

In a first experiment, 8 (256×256 pixels) equiangular projections ($360°$ scan) for the reference scan were generated from a dough software phantom ($512 \times 512 \times 512$ voxels, see Figure 3.5) with the ASTRA-toolbox [22, 23, 24]. A projection of the affinely deformed phantom was simulated with the following affine deformation parameters:

$$\begin{aligned}\mathbf{A} &= \begin{bmatrix} 1.03 & 0.01 & -0.01 \\ 0 & 0.97 & 0.01 \\ 0 & 0 & 1.05 \end{bmatrix} \\ \mathbf{u} &= [7, -10, -11]^T.\end{aligned} \tag{3.23}$$

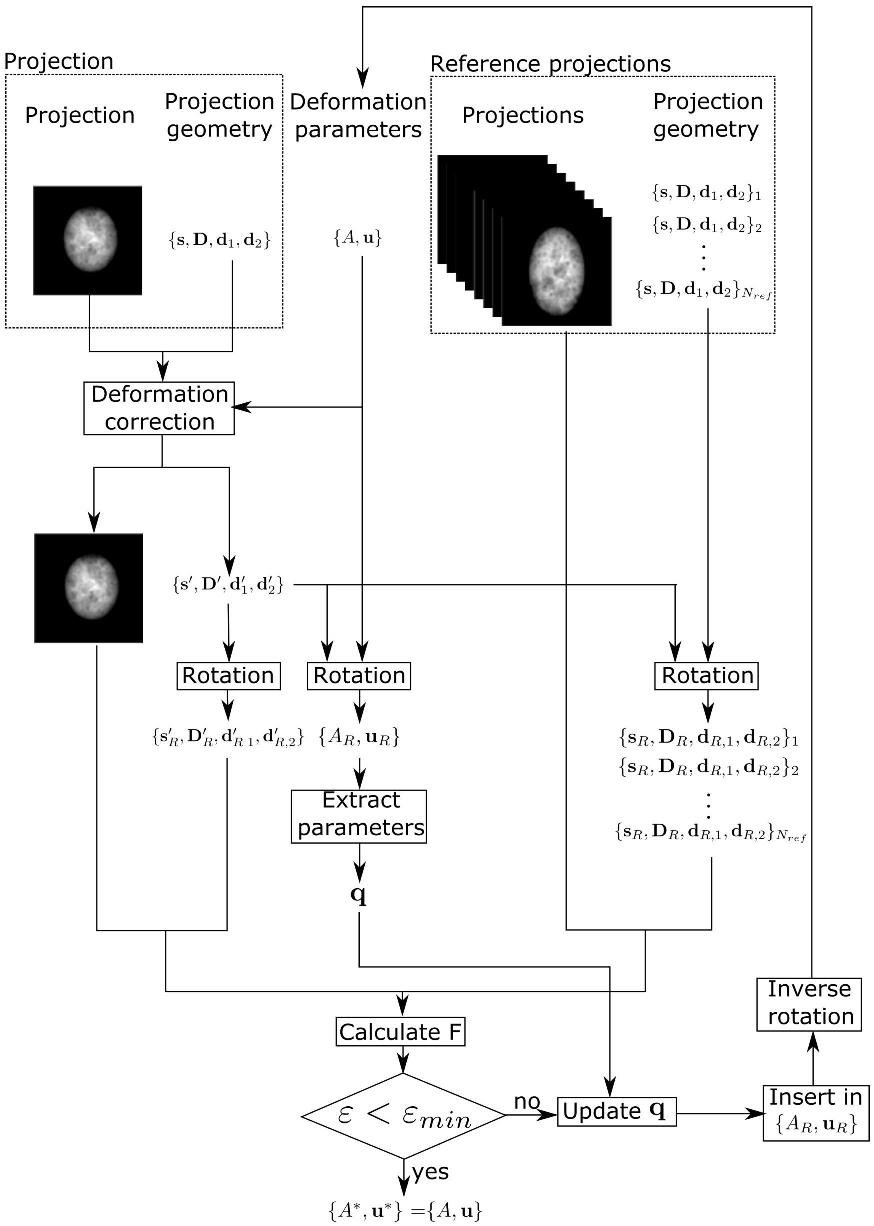

Figure 3.4: Schematic overview of the deformation estimation technique for a single projection.

(a) (b) (c)

Figure 3.5: Three orthogonal cross-sections of the dough phantom.

The performance of the affine deformation estimation method was studied in function of the SNR of the projections, the number of planes that are checked for consistency and the projection angle of the main projection (angle ϕ in Figure 3.2b). Poisson noise was applied to the projection data assuming 20000 photons in the incoming beam per detector pixel (the photon count). Each experiment was repeated 10 times. The estimated and ground truth parameters cannot be compared directly since the proposed technique only estimates deformations perpendicular to the projection direction. The estimated deformation parameters describing these deformations are influenced by deformations in the projection direction. To quantify the quality of the estimated deformation parameters, the mean square error (MSE) was calculated on the projections as follows:

$$\mathrm{MSE} = \frac{1}{M}\Sigma_i\Sigma_j \left(C_{\mathbf{q}_k^*}(f(\mathbf{x}),i,j) - C_{\mathbf{q}_{Id}}(f_T(\mathbf{x}),i,j)\right)^2, \tag{3.24}$$

with:

$$C_{\mathbf{q}_k}(f(\mathbf{x}),i,j) = \frac{\det(\mathbf{A}^{-1})}{\|(\mathbf{A}^{-1})^T\mathbf{n}_1(j)\|\|(\mathbf{A}^{-1})^T\mathbf{n}_2(i)\|}C_{G'}(f(\mathbf{x}),i,j). \tag{3.25}$$

In Eq. 3.24, M represents the number of pixels on the detector and $\mathbf{q}_{Id} = \begin{bmatrix}1 & 0 & 0 & 1 & 0 & 0\end{bmatrix}^T$ the parameters of the identity transformation. The MSE compares the noiseless projection of the affine transformed phantom with a projection of the undeformed phantom created with the virtual geometry. This measure reflects the consistency of the corrected projection with the object in the reference state. Since the projections used to calculate the MSE are noiseless, whereas the estimated deformation parameters are calculated on noisy projections, the MSE is a measure of the quality of the estimated deformation parameters.

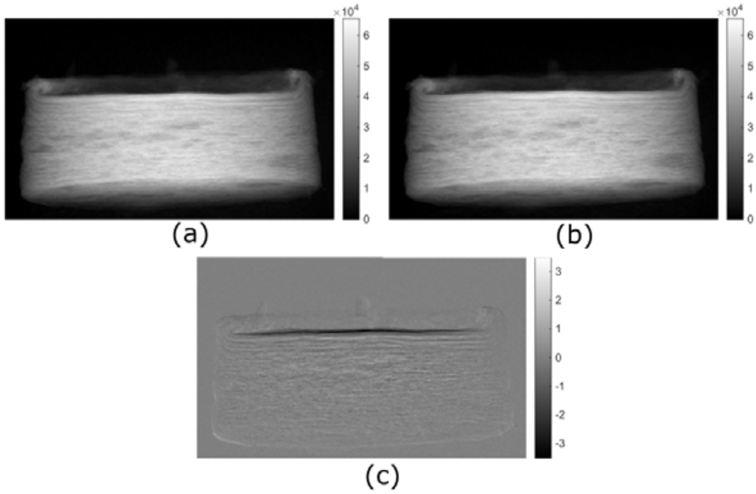

Figure 3.6: The first (a) and last projection (b) of the main scan of the puff pastry dataset, both acquired at the same angle. The difference between these projections is shown in (c).

For the second experiment, the same dough software phantom was used to generate 8 (256×256 pixels) equiangular projections ($360°$ scan) for the reference scan. The 250 projections of the main scan were generated from an affinely deformed phantom. The affine deformation parameters changed linearly with each projection, starting from the identity deformation and ending with the affine transformation given by Eq. 3.23. For each projection the deformation parameters were estimated. The result of the $(k-1)^{\text{th}}$ projection was used as an initialization of the k^{th} projection, resulting in a faster estimation. The experiment was repeated for different photon counts.

3.3.2 Real data

The proposed deformation estimation technique was tested on a CT scan of a leavening puff pastry, acquired with a micro-CT scanner with a horizontal gantry [25]. Throughout the leavening process the scanner acquired projections during 5 gantry rotations, with a total scan time of 20 minutes. Each gantry rotation consisted of 722 equiangular 401×656 projections. Each projection was acquired with a source voltage of 60kV, a target current of 200mA and an exposure time of 100ms. Reconstructions, with a voxel size of $12.5\mu m$, of each of the rotations were calculated with 300 SIRT iterations. Visual inspection of the reconstruction of the first gantry rotation revealed almost no deformation artefacts. Eight projections of the first gantry rotation, approximately $45°$ degrees apart, were selected as reference projections. The next 4 gantry rotations were used to construct the main scan with deformation. One fourth of the projections was selected as to mimic an interleaved scanning protocol (binary decomposition), ensuring maximum angular sampling of the object [26]. Truncation was not observed in the projections (except for the sample holder, which was made of a low attenuating foam). The difference between the first and last projection of the main scan is shown in Figure 3.6. The affine deformation parameters were estimated in a two step process. Firstly, only the z-translation and z-scaling were estimated, keeping the rest of the deformation parameters constant at the value of the identity transformation. These two parameters were expected to describe the majority of the deformation. Secondly, all the deformation parameters were estimated with the result of the first estimation as an initial starting point. This strategy guides the estimation in such a way that it avoids local minima in the objective function as much as possible. The original and deformation corrected projections (and projection geometries) were reconstructed on a $656 \times 656 \times 401$ voxel grid with 300 SIRT iterations on the distributed version of the ASTRA-toolbox[27, 28].

3.4 Results and discussion

3.4.1 Phantom study

Figure 3.7 shows the MSE of the proposed affine deformation correction algorithm in function of the SNR (in terms of the number of photons) (Figure 3.7a), the number of compared planes between projection pairs (Figure 3.7b), and the projection directions (Figure 3.7c). The grey areas represents the 95% confidence interval. Figure 3.7a reveals that the algorithm can substantially reduce motion artefacts in terms of the MSE even for very low (as low as 100 photons per detector pixel) photon counts.

In Figure 3.7b, the MSE as a function of the number of compared planes between every projection pair is shown. The MSE of the projection without deformation correction is 5.83×10^{11}, which is significantly higher than all cases with deformation correction. The quality of the estimation improves with the number of compared planes but levels out if more than 200 planes are compared. In general, the optimal number of planes will increase with the number of pixels in the detector.

Figure 3.7c shows the MSE for different projection directions with and without deformation estimation. For all projection angles, a clear decrease of the MSE is observed after affine deformation correction. No difference was observed between projections that have an opposing reference projection and projections without opposing reference projection.

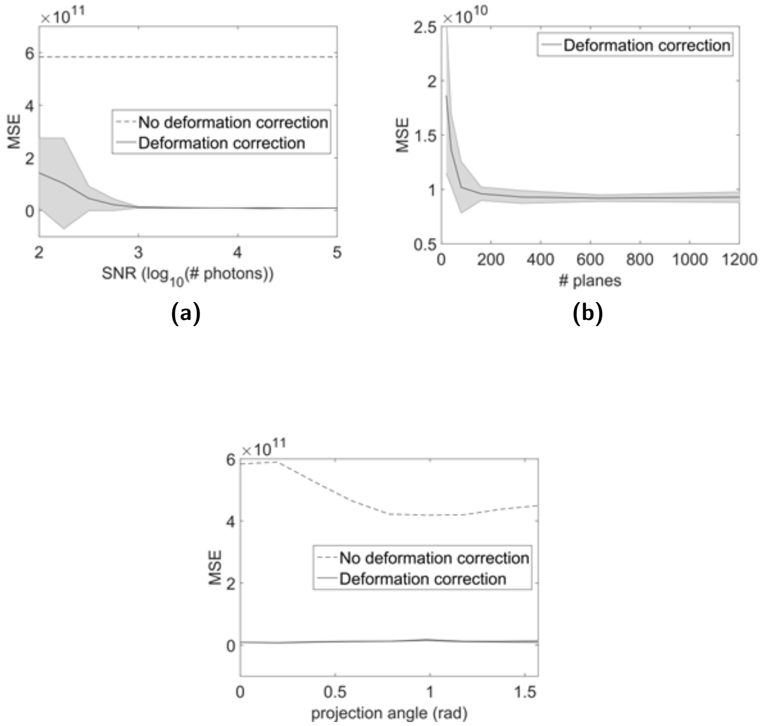

(a) (b) (c)

Figure 3.7: MSE values for the dough phantom experiments as a function of (a) the SNR (in terms of photon count), (b) the number of planes compared in every projection pair (the MSE of the projection without deformation correction is 5.83×10^{11}) and (c) the direction of the main projection. The grey areas represent the 95% confidence interval.

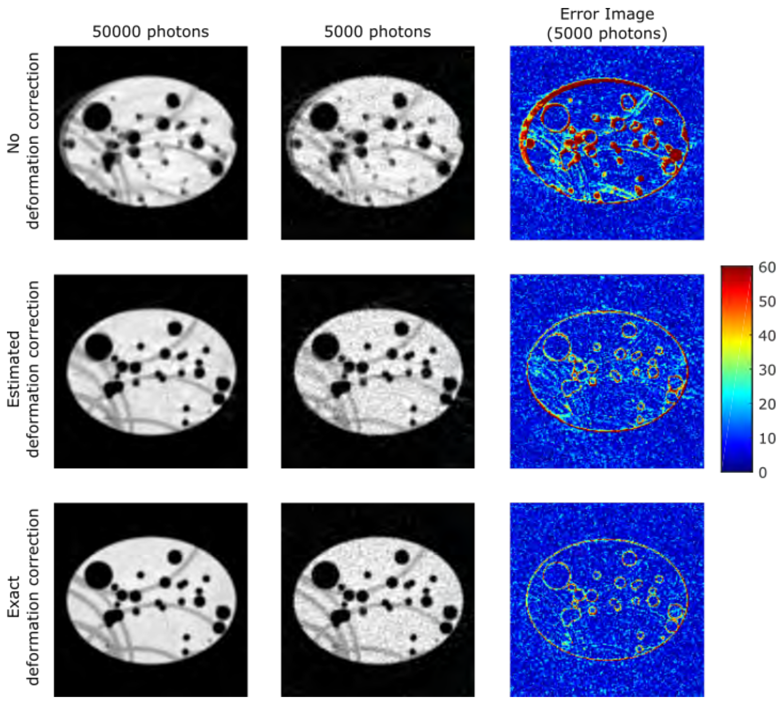

Figure 3.8: Reconstructions of a horizontal cross-section (perpendicular to rotation axis) of the dough phantom undergoing affine deformation. The cross-sections were motion corrected with different techniques: without deformation correction (top row), with deformation corrected with estimated deformation parameters (estimated deformation correction) (middle row) and with deformation correction with the exact deformation parameters (bottom row). Left column: high photon count (50000 photons per detector pixel). Middle column: low photon count (5000 photons per detector pixel). The images are scaled between 0 and 120. Right column: Absolute difference of the reconstructions (5000 photons per pixel) with the ground truth.

In Figure 3.8, the reconstructions of the dough phantom simulation experiments are shown for high (left column) and a low (middle column) photon counts. For the low photon count reconstructions, a comparison with the ground truth is provided in Figure 3.8 (right column).

Figure 3.8 (top row) shows the reconstructions without deformation correction. The motion artefacts are clearly observable: the borders of the dough and holes are doubled and many structures are substantially blurred. Large deviations from the ground truth are visible in the error image. Figure 3.8 (middle row) shows the reconstructions with the proposed affine deformation correction method in which the deformation parameters are estimated from the cone beam projections. As can be observed from these figures, motion artefacts are significantly reduced compared to the reconstructions without deformation correction (top row). In the error image, a close resemblance to the ground truth can be observed. For reference, Figure 3.8 (bottom row) also shows the reconstructions after correcting for affine deformation using the (in practice unknown) ground truth deformation parameters. As can be expected, the error image of deformation corrected reconstruction with the ground truth deformation parameters shows the smallest errors.

Because of its short acquisition time, the reference scan provides a set of projections in multiple directions of the (almost undeformed) object. Other strategies could avoid the reference scan and use only the first projection as a reference and optimize the affine deformation parameters in such a way that all projections are consistent. Such a strategy is however flawed in practice. Projections with a projection direction perpendicular to that of the reference projection have only limited redundantly measured data with this reference projection. As a result, the reconstruction can deform in the reference projections projection direction without significantly violation the optimization criterion. The addition of the reference scan solves this problem.

3.4.2 Real data

Figure 3.9 shows the results of the puff pastry experiment: horizontal and vertical cross-sections are shown in the left and right column, respectively. The reconstructions of the first gantry rotation (Figure 3.9 top row) are almost deformation free: a clear separation between the dough layers can be observed and the holes have sharp edges. Figure 3.9 (middle row) shows the reconstruction of the main scan without affine deformation correction. This reconstruction is corrupted by motion artefacts. The top of the object is not well reconstructed since this part undergoes the biggest deformation. As a result, gradual transitions between the dough layers can be observed and the borders of the holes are not as sharp as in the first gantry rotation. Figure 3.9 (bottom row) shows the reconstructed images of the same dataset with the proposed affine deformation estimation and correc-

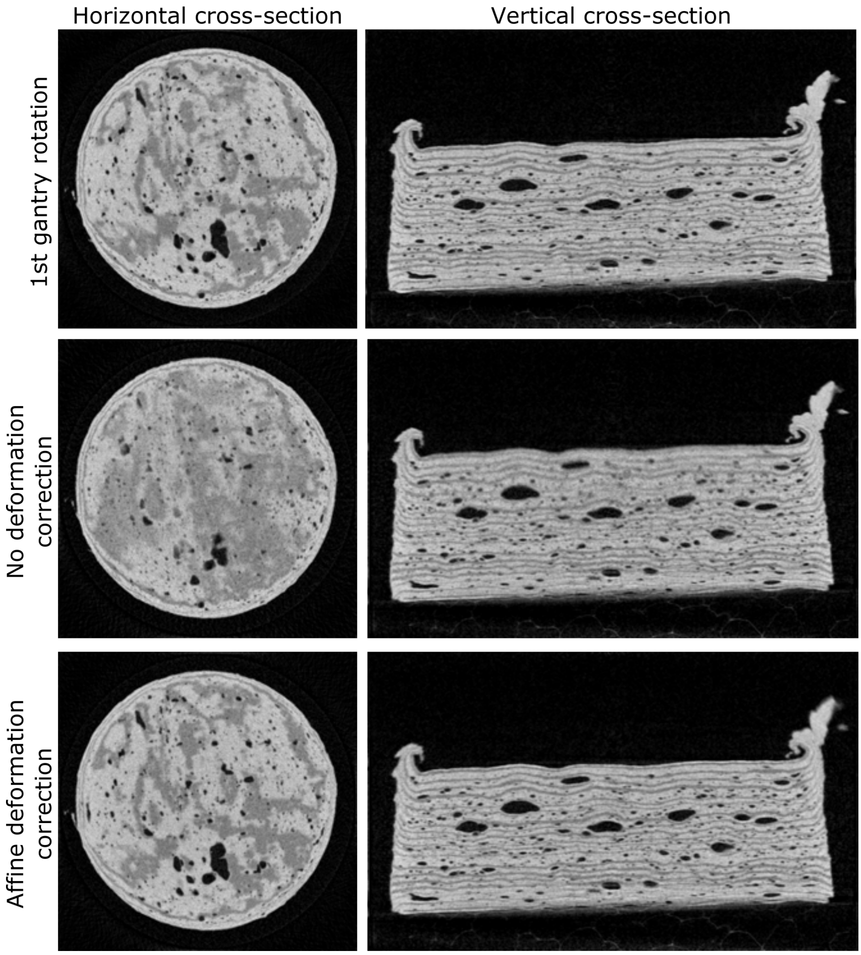

Figure 3.9: SIRT reconstructions of the first gantry rotation and reconstructions of the main scan without deformation correction and with deformation correction. Left column: horizontal cross-section (top of object). Right column: vertical cross-section (middle of object).

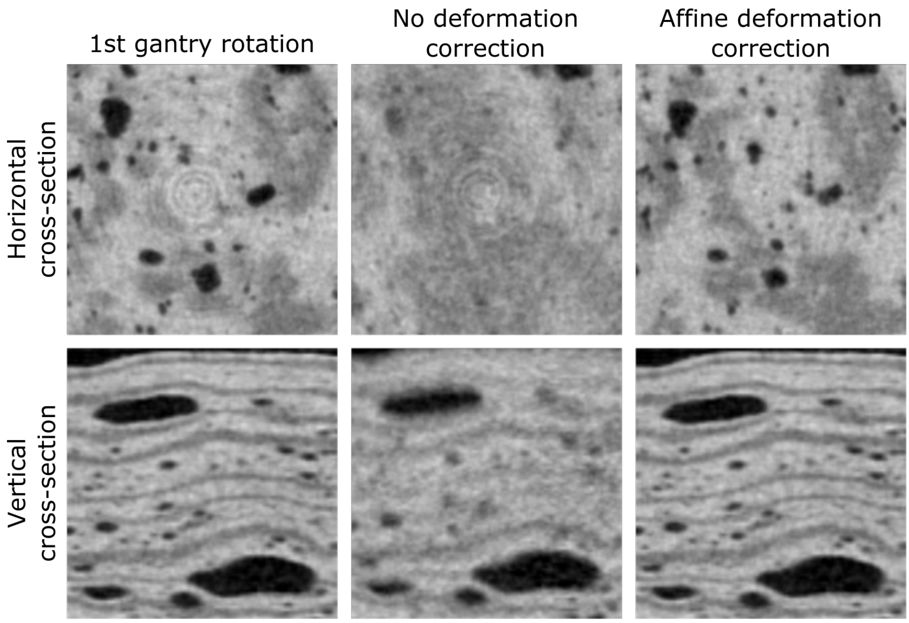

Figure 3.10: Zoomed in reconstructions of the first gantry rotation (left column) and reconstructions of the main scan without deformation correction (middle column) and with deformation correction (right column). Top row: horizontal cross-section (Horizontally: top of object. Vertically: middle of object). Bottom row: vertical cross-section (Horizontally: top of object. Vertically: middle of object).

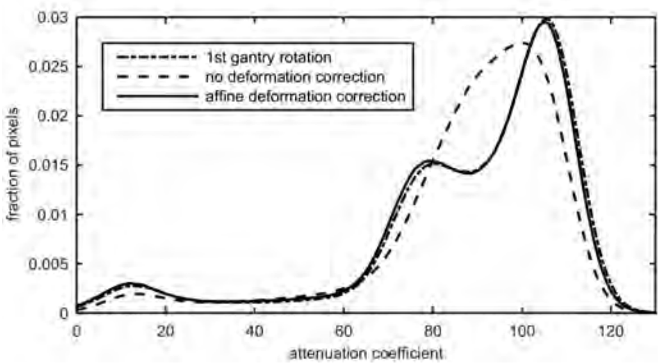

Figure 3.11: Histogram of a region of interest (almost the whole puff pastry) of the puff pastry reconstructions.

tion technique. The reconstruction has a high spatial resolution, similar to the reconstruction of the first gantry rotation, though with a much higher SNR. There are clear delineations between the dough layers and the holes have sharp borders. The only part of the reconstruction where motion artefacts are noticeable is at the top right of the vertical cross-section (Figure 3.9: third row, right column), where slight blurring of the protruding part can be observed. Figure 3.10 shows zoomed images of the reconstructions shown in Figure 3.9. Nevertheless, the results of this experiment clearly show that the proposed affine deformation estimation and correction technique performs well in generating almost motion artefact free images. We were able to show that the motion artefacts can be substantially reduced and a better reconstruction quality, with a higher signal to noise ratio, than that achieved by the first gantry rotation.

Motion artefacts have a large effect on the histogram of the reconstruction. Figure 3.11 shows the histogram of a region of interest (almost the whole puff pastry without background) in the reconstructions. In the histogram of the first gantry rotation and the deformation corrected reconstruction of the main scan, three modes can be distinguished: a mode corresponding to the holes and two modes corresponding to the different layers in the dough (fat and dough). The histogram of the reconstruction of the main scan without deformation correction shows only two modes. While the holes are still distinguishable in the puff pastry image, the two different dough layers are merged into one broad peak in the histogram. Since the histogram is often used in image post processing, such as determining the thresholds for a segmentation, it is clear that the presence of motion artefacts may significantly influence the results of further analysis.

An interesting (positive) side effect of the proposed motion correction technique is ring artefact reduction, which can be noticed in the reconstructions (see left column Figure 3.10). While the horizontal cross-sections of the first gantry rotation and the reconstruction without deformation correction are degraded by ring artefacts, the affine deformation corrected reconstruction shows no ring artefacts at all. This effect is not surprising since the origin of these ring artefacts is a combination of a deviating pixel response and the circular trajectory of the gantry [29]. By estimating a virtual projection geometry the source trajectory will no longer be circular and the reconstruction algorithm will no longer produce ring artefacts.

With respect to computational load, the proposed method is efficient in the sense that it does not involve a reconstruction step. The average computation time to estimate the affine deformation of a single projection was only 6.3s on a computer with an Intel Core i7-3930K CPU and a NVIDIA GeForce GTX 660 GPU.

3.4.3 4D reconstructions

The proposed technique is able to correct for affine deformations during the acquisition and results in a reconstruction at the time point of the reference scan. Often, researchers are interested in 4D reconstructions (3 spatial dimensions and 1 time dimension) of the object and want to visualize the deformation in time. Since an affine deformation is estimated at each projection, a reconstruction at the time point of each projection can be calculated with Eq. 3.3. Nevertheless, the estimated affine deformations are only accurate in the direction orthogonal to the projection direction and, as a result, the visualized deformation may not be in accordance to the real deformation.

This issue can be solved with multiple source-detector pairs. For example, in a scanner with two source-detector pairs, positioned perpendicular with respect to each other, all affine deformation parameters can be estimated, enabling an accurate 4D reconstruction. Alternatively, the deformation parameters corresponding to the projection direction might be estimated by interpolation between the deformation parameters of projections that are as non-parallel as possible and in temporal proximity.

3.4.4 Medical applications

The proposed method has numerous applications in micro-CT. In addition, Cone Beam CT (CBCT) is also an important imaging tool in (bio)medical practice. Since the geometry of these acquisitions is equivalent to the geometry in micro-CT, the method can as well be applied in medical CBCT. The affine correction framework can be used for rigid as well as affine motion correction. In applications with only rigid motion (e.g. head motion), the affine parameters corresponding to scaling and shearing are kept constant, while only estimating translation and rotation. Furthermore, our method can even be used as a first order approximation of non-affine motion correction (e.g., respiration), if a reference scan without motion can be acquired.

3.5 Conclusion

In this chapter, an affine deformation estimation and correction technique for cone beam computed tomography was proposed. The proposed method works completely in the projection domain, hence avoiding computationally intensive reconstructions. To correct affine deformations, a relationship between cone beam projections and affine transformations was proven. Estimation of the affine deformation parameters for each projection is achieved by minimizing an inconsistency condition with respect to a fast reference scan consisting of only a few projections.

Experiments on simulated and real data showed that the proposed affine deformation correction method is able to remove or alleviate motion artefacts in non-truncated cone beam projections. Moreover, it reduces ring artefacts as a positive side-effect.

3.6 Appendix

In the following section we will proof Eq. 3.4 and Eq. 3.5.

Proof.

$$\begin{aligned} C_G(f_T(\mathbf{x}), i, j) &= \int f_T(\mathbf{x}) \delta\left(\mathbf{n}_1(j) \cdot (\mathbf{x} - \mathbf{s})\right) \delta\left(\mathbf{n}_2(i) \cdot (\mathbf{x} - \mathbf{s})\right) d\mathbf{x} \\ &= \int f(\mathbf{A}\mathbf{x} + \mathbf{u}) \delta\left(\mathbf{n}_1(j) \cdot (\mathbf{x} - \mathbf{s})\right) \delta\left(\mathbf{n}_2(i) \cdot (\mathbf{x} - \mathbf{s})\right) d\mathbf{x} \end{aligned} \tag{3.26}$$

Change of variables $\mathbf{y} = \mathbf{A}\mathbf{x} + \mathbf{u}$:

$$\begin{aligned} C_G(f_T(\mathbf{x}), i, j) = \det(\mathbf{A}^{-1}) \int f(\mathbf{y}) \delta\left(\mathbf{n}_1(j) \cdot (\mathbf{A}^{-1}(\mathbf{y} - \mathbf{u}) - \mathbf{s})\right) \\ \delta\left(\mathbf{n}_2(i) \cdot (\mathbf{A}^{-1}(\mathbf{y} - \mathbf{u}) - \mathbf{s})\right) d\mathbf{y} \end{aligned} \tag{3.27}$$

Since $\mathbf{A}\mathbf{x} \cdot \mathbf{y} = \mathbf{x} \cdot \mathbf{A}^T \mathbf{y}$ and $\delta(x) = |a|\delta(ax)$, we have:

$$\begin{aligned} C_G(f_T(\mathbf{x}), i, j) = & \frac{\det(\mathbf{A}^{-1})}{\|(\mathbf{A}^{-1})^T \mathbf{n}_1(j)\| \|(\mathbf{A}^{-1})^T \mathbf{n}_2(i)\|} \\ & \int f(\mathbf{y}) \delta\left(\frac{(\mathbf{A}^{-1})^T \mathbf{n}_1(j)}{\|(\mathbf{A}^{-1})^T \mathbf{n}_1(j)\|} \cdot (\mathbf{y} - \mathbf{u} - \mathbf{A}\mathbf{s})\right) \\ & \delta\left(\frac{(\mathbf{A}^{-1})^T \mathbf{n}_2(i)}{\|(\mathbf{A}^{-1})^T \mathbf{n}_2(i)\|} \cdot (\mathbf{y} - \mathbf{u} - \mathbf{A}\mathbf{s})\right) d\mathbf{y}. \end{aligned} \tag{3.28}$$

Next, a virtual geometry is defined as:

$$\begin{cases} \mathbf{s}' &= \mathbf{A}\mathbf{s} + \mathbf{u} \\ \mathbf{d}'_c &= \mathbf{A}\mathbf{d}_c + \mathbf{u} \\ \mathbf{d}'_1 &= \mathbf{A}\mathbf{d}_1 \\ \mathbf{d}'_2 &= \mathbf{A}\mathbf{d}_2 \end{cases} \tag{3.29}$$

$$C_G(f_T(\mathbf{x}), i, j) = \frac{\det(\mathbf{A}^{-1})}{\|(\mathbf{A}^{-1})^T \mathbf{n}_1\| \|(\mathbf{A}^{-1})^T \mathbf{n}_2\|} \int f(\mathbf{y}) \\ \delta\left(\frac{(\mathbf{A}^{-1})^T \mathbf{n}_1(j)}{\|(\mathbf{A}^{-1})^T \mathbf{n}_1(j)\|} \cdot (\mathbf{y} - \mathbf{s}')\right) \\ \delta\left(\frac{(\mathbf{A}^{-1})^T \mathbf{n}_2(i)}{\|(\mathbf{A}^{-1})^T \mathbf{n}_2(i)\|} \cdot (\mathbf{y} - \mathbf{s}')\right) d\mathbf{y}. \quad (3.30)$$

We will now show that $\frac{(\mathbf{A}^{-1})^T \mathbf{n}_1(j)}{\|(\mathbf{A}^{-1})^T \mathbf{n}_1(j)\|} = \mathbf{n}'_1(j)$:

$$\begin{aligned} \frac{(\mathbf{A}^{-1})^T \mathbf{n}_1(j)}{\|(\mathbf{A}^{-1})^T \mathbf{n}_1(j)\|} &= \frac{1}{Z} (\mathbf{A}^{-1})^T \left[(\mathbf{m}_{ij} - \mathbf{s}) \times \mathbf{d}_1\right] \\ &= \frac{\det(\mathbf{A})}{Z} \left[\mathbf{A}\left(\mathbf{d}_c + j\mathbf{d}_2 - \mathbf{s}\right) \times \mathbf{A}\mathbf{d}_1\right] \\ &= \frac{1}{Z'} \left[(\mathbf{d}'_c + j\mathbf{d}'_2 - \mathbf{s}') \times \mathbf{d}'_1\right] \\ &= \mathbf{n}'_1(j). \end{aligned} \quad (3.31)$$

Here we used the property: $\mathbf{A}(\mathbf{x} \times \mathbf{y}) = \det(\mathbf{A}^{-1}) \left[(\mathbf{A}^{-1})^T \mathbf{x} \times (\mathbf{A}^{-1})^T \mathbf{y}\right]$. Z and Z' are normalization constants. We can prove equivalently that $\frac{(\mathbf{A}^{-1})^T \mathbf{n}_2(i)}{\|(\mathbf{A}^{-1})^T \mathbf{n}_2(i)\|} = \mathbf{n}'_2(i)$. Substituting these relations in (3.30), we have:

$$C_G(f_T(\mathbf{x}), i, j) = \\ \frac{\det(\mathbf{A}^{-1})}{\|(\mathbf{A}^{-1})^T \mathbf{n}_1(j)\| \|(\mathbf{A}^{-1})^T \mathbf{n}_2(i)\|} \int f(\mathbf{y}) \delta\left(\mathbf{n}'_1(j) \cdot (\mathbf{y} - \mathbf{s}')\right) \\ \delta\left(\mathbf{n}'_2(i) \cdot (\mathbf{y} - \mathbf{s}')\right) d\mathbf{y}. \quad (3.32)$$

If we compare (3.32) with (3.2), we can write:

$$C_G(f_T(\mathbf{x}), i, j) = \frac{\det(\mathbf{A}^{-1})}{\|(\mathbf{A}^{-1})^T \mathbf{n}_1(j)\| \|(\mathbf{A}^{-1})^T \mathbf{n}_2(i)\|} C_{G'}(f(\mathbf{x}), i, j), \quad (3.33)$$

with $G' = \{\mathbf{s}', \mathbf{d}'_c, \mathbf{d}'_1, \mathbf{d}'_2\}$. □

References

[1] C. J. Ritchie, J. D. Godwin, C. R. Crawford, W. Stanford, H. Anno, and Y. Kim, "Minimum scan speeds for suppression of motion artifacts in CT," *Radiology*, vol. 185(1), pp. 37–42, 1992.

[2] G. Van Eyndhoven, K. J. Batenburg, D. Kazantsev, V. Van Nieuwenhove, P. D. Lee, K. J. Dobson, and J. Sijbers, "An iterative CT reconstruction algorithm for fast fluid flow imaging," *IEEE Trans. Image Process.*, vol. 24, no. 11, pp. 4446–4458, 2015.

[3] R. Clackdoyle and L. Desbat, "Data consistency conditions for truncated fanbeam and parallel projections," *Med. Phys.*, vol. 42, pp. 831–845, Feb. 2015.

[4] M. Negahdar and A. A. Amini, "Estimation of affine motion from projection data using a mass conservation model.," in *33rd Annu. Int. Conf. IEEE EMBS.*, pp. 8041–8044, Jan. 2011.

[5] R. Mooser, F. Forsberg, E. Hack, G. Székely, and U. Sennhauser, "Estimation of affine transformations directly from tomographic projections in two and three dimensions," *Mach. Vision Appl.*, vol. 24, pp. 419–434, Oct. 2011.

[6] S. R. Deans, *The Radon transform and some of its applications.* Courier Corporation, 2007.

[7] S. Roux, L. Desbat, A. Koenig, and P. Grangeat, "Exact reconstruction in 2D dynamic CT: compensation of time-dependent affine deformations," *Phys. Med. Biol.*, vol. 49, pp. 2169–2182, Jun. 2004.

[8] X. Xiong and K. Qin, "Linearly estimating all parameters of affine motion using Radon transform," *IEEE T. Image Process.*, vol. 23, pp. 4311–4321, Oct. 2014.

[9] R. Frysch and G. Rose, "Rigid motion compensation in interventional C-arm CT using consistency measure on projection data," in *Proc. 2015 MICCAI*, vol. 9349, pp. 298–306, Springer.

[10] W. Wein and A. Ladikos, "Towards general motion recovery in cone-beam computed tomography," in *Fully Three-Dimensional Image Reconstruction Radiology and Nuclear Medicine: Proc.*, pp. 54–57, Jun. 2013.

[11] S. Leng, B. Nett, M. Speidel, and G. Chen, "Motion artifact reduction in fan-beam and cone-beam computed tomography via the fan-beam data consistency condition (FDCC)," in *Proc. SPIE 6510, Medical Imaging 2007: Physics of Medical Imaging.*

[12] P. Grangeat, "Mathematical framework of cone beam 3D reconstruction via the first derivative of the Radon transform," in *Mathematical Methods in Tomography*, vol. 1497, pp. 66–97, 1990.

[13] M. Defrise and R. Clack, "A cone-beam reconstruction algorithm using shift-variant filtering and cone-beam backprojection," *IEEE T. Med. Imaging*, vol. 13, pp. 186–195, Jan. 1994.

[14] C. Debbeler, N. Maass, M. Elter, F. Dennerlein, and T. Buzug, "A new CT raw data redundancy measure applied to automated misalignment correction," in *Fully Three-Dimensional Image Reconstruction Radiology and Nuclear Medicine: Proc.*, pp. 264–267, 2013.

[15] M. Elter, N. Maass, and P. Koch, "Suitability of a new alignment correction method for industrial CT," in *Proc.: Conf. Industrial Computed Tomography*, pp. 245–252, Feb. 2014.

[16] A. Aichert, N. Maass, Y. Deuerling-Zheng, M. Berger, M. Manhart, J. Hornegger, A. K. Maier, and A. Doerfler, "Redundancies in X-ray images due to the epipolar geometry for transmission imaging," in *3th Int. Conf. image formation X-ray computed tomography*, pp. 333–337, 2015.

[17] A. Aichert, M. Berger, J. Wang, N. Maass, A. Doerfler, J. Hornegger, A. K. Maier, and A. O. Lines, "Epipolar consistency in transmission imaging," *IEEE T. Med. Imaging*, vol. 34, pp. 2205–2219, Nov. 2015.

[18] P. L. Salmon, X. Liu, and A. Sasov, "A post-scan method for correcting artefacts of slow geometry changes during micro-tomographic scans," *J. X-ray Sci. Technol.*, vol. 17, pp. 161–174, Feb. 2009.

[19] T. Grulich, W. Holub, U. Haßler, A. Aichert, and A. Maier, "Geometric adjustment of X-ray tomosynthesis," in *Fully Three-Dimensional Image Reconstruction Radiology and Nuclear Medicine: Proc.*, pp. 468–471, Jun. 2015.

[20] L. A. Feldkamp, L. C. Davis, and J. W. Kress, "Practical cone-beam algorithm," *J. Opt. Soc. Am. A*, vol. 1, pp. 612–619, Jun. 1984.

[21] J. Nocedal and S. J. Wright., *Numerical Optimization*. Springer Series in Operations Research, Springer Verlag, 2006.

[22] W. J. Palenstijn, K. J. Batenburg, and J. Sijbers, "Performance improvements for iterative electron tomography reconstruction using graphics processing units (GPUs)," *J. Struct. Biol.*, vol. 176, pp. 250–253, Nov. 2011.

[23] W. Van Aarle, W. J. Palenstijn, J. De Beenhouwer, T. Altantzis, S. Bals, K. J. Batenburg, and J. Sijbers, "The ASTRA toolbox: A platform for advanced algorithm development in electron tomography," *Ultramicroscopy*, vol. 157, pp. 35–47, Oct. 2015.

[24] W. Van Aarle, W. J. Palenstijn, J. Cant, E. Janssens, F. Bleichrodt, A. Dabravolski, J. De Beenhouwer, K. J. Batenburg, and J. Sijbers, "Fast and flexible X-ray tomography using the ASTRA toolbox," *Opt. Express*, vol. 24, no. 22, pp. 25129–25147, 2016.

[25] M. Dierick, D. Van Loo, B. Masschaele, J. Van den Bulcke, J. Van Acker, V. Cnudde, and L. Van Hoorebeke, "Recent micro-CT scanner developments at UGCT," *Nucl. Instr. Meth. Phys. Res., B*, vol. 324, pp. 35–40, Apr. 2014.

[26] A. Kaestner, B. Münch, P. Trtik, and L. Butler, "Spatiotemporal computed tomography of dynamic processes," *Opt. Eng.*, vol. 50, p. 123201, Dec. 2011.

[27] J. Gregor and T. Benson, “Computational analysis and improvement of SIRT,” *IEEE T. Med. Imaging*, vol. 27, pp. 918–924, Jan. 2008.

[28] W. J. Palenstijn, J. Bédorf, and K. J. Batenburg, “A distributed SIRT implementation for the ASTRA toolbox,” in *Fully Three-Dimensional Image Reconstruction Radiology and Nuclear Medicine: Proc.*, pp. 166–169, Jun. 2015.

[29] J. Sijbers and A. Postnov, “Reduction of ring artefacts in high resolution micro-CT reconstructions,” *Phys. Med. Biol.*, vol. 49, pp. 247–253, Jul. 2004.

4

MoVIT: A tomographic reconstruction framework for 4D-CT

Contents

4.1 Introduction 84
4.2 Method 85
4.2.1 Stationary algebraic tomography 85
4.2.2 Dynamic tomographic model 86
4.2.3 MotionVector-based Iterative Technique 87
4.2.4 Deformation estimation 89
4.3 Experiments and results 90
4.3.1 Reconstruction methods 90
4.3.2 Figures of merit 91
4.3.3 Numerical simulations 91
4.3.4 Polyurethane dataset 92
4.4 Discussion 100
4.4.1 Numerical simulations 100
4.4.2 Polyurethane dataset 100
4.5 Conclusion 101
References 101

This chapter has been published as:
V. Van Nieuwenhove, J. De Beenhouwer, J. Vlassenbroeck, M. Brennan and J. Sijbers, *"MoVIT: A tomographic reconstruction framework for 4D-CT"*, Optics Express, vol. 25, no. 16, pp. 19236-19250, 2017.

4.1 Introduction

In 4D-CT it is highly beneficial to include other time frames in the reconstruction of a certain time frame, as discussed in Section 1.3.2. Previously proposed 4D-CT reconstruction methods exploiting this strategy can be split up into different classes. A first class assumes structural changes to be local. For example, rSIRT assumes that only a well-defined area undergoes deformation and the rest of the reconstruction domain is static [1]. A fluid motion model can also be incorporated in the reconstruction algorithms as demonstrated in [2, 3]. In perfusion CT the time curve in the artery pixels can be modelled more accurately with gamma variate basis function, resulting in a reduced radiation dose [4]. Such algorithms either rely on an a priori high quality reconstruction or assume that the location of structural changes is known [3, 5, 2]. A second class regularises both the spatial and temporal domain of the reconstructions with, for example, Markov random fields [6, 7]. While these algorithms do not depend on a particular deformation model they often suffer from long computation times and a large number of tunable parameters.

The last class of methods assumes the deformation to be described as a diffeomorphic deformation vector field (DVF) that is included into the reconstruction algorithm. This vector field describes the displacement of every voxel between two time frames. Since the deformation is a priori unknown, it has to be estimated. Some reconstruction methods include volume registration to improve reconstructions with deformation artefacts due to respiratory and cardiac motion [8, 9, 10, 11]. These methods exploit the periodicity of the motion [8], assume that a prior deformation free scan is available [10], assume multiple quiescent motion time frames [9], or have a high number of tunable parameters [11]. These properties prevent the use of these algorithms in the context of micro-CT where a wide range of samples and dynamics has to be studied.

In this chapter, we propose the MotionVector-based Iterative Technique (MoVIT). It incorporates the deformation fields directly into the reconstruction process and, as such, exploits information from projections of other time frames into the reconstruction of the image at a particular time frame. In order to estimate the deformation field map, non-rigid volume registrations are performed on conventionally reconstructed volumes of the different time frames.

The chapter is structured as follows. In section 4.2, the proposed reconstruction algorithm and deformation estimation strategy, MoVIT, is explained. Next, in section 4.3, MoVIT is compared to common reconstruction algorithms in a numerical way as well as on an experimental dataset, the results of which are discussed in section 4.4.

4.2 Method

In subsection 4.2.1, an overview of the stationary tomographic model will be given and generalised (in subsection 4.2.2) to the dynamic case. Next, in subsection 4.2.3, the MoVIT reconstruction algorithm is described, which incorporates a deformation field into an algebraic reconstruction method (ARM) that is assumed to be known a priori. This restriction is then abrogated in subsection 4.2.4, where an estimation method for the deformation vector field is introduced.

4.2.1 Stationary algebraic tomography

Let $\boldsymbol{x} = (x_i) \in \mathbb{R}^N$ be a vector of unknown volume elements representing the scanned object. The log-corrected projection values for all projection angles $\boldsymbol{\theta} = (\theta_i) \in [0, 2\pi[^M$ are denoted by $\boldsymbol{p} = (p_i) \in \mathbb{R}^M$. The projection process can be simulated as $\boldsymbol{q} = \boldsymbol{A}\boldsymbol{x}$, where $\boldsymbol{A} = (a_{ij}) \in \mathbb{R}^{M \times N}$ is a matrix of which the entries a_{ij} represent the contribution of pixel value x_j to projection value q_i (see Figure 4.1).

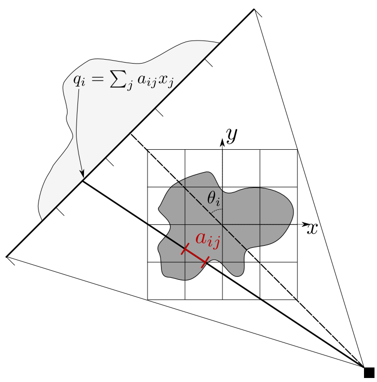

Figure 4.1: Illustration of the projection process. The contribution a_{ij} of pixel x_j to the projection value q_i is represented as the ray-intersection length of projection line i with pixel j.

The system of linear equations $\boldsymbol{A}\boldsymbol{x} = \boldsymbol{p}$ cannot be solved directly since $\boldsymbol{A}$ is generally not invertible. A closed form expression for the (regularized) least-squares solution can be derived. However, due to the size of the problem, the direct calculation of this solution is infeasible on modern computers. Therefore, algebraic reconstruction methods such as ART, SART or SIRT, start with an initial guess $\boldsymbol{x} = \boldsymbol{x}^0$ and iteratively compute new estimates $\boldsymbol{x}^k$ $(k = 1, 2, \ldots)$. This is repeated until an *approximate* solution of $\boldsymbol{A}\boldsymbol{x} = \boldsymbol{p}$ is found. For example, the simultaneous iterative reconstruction technique (SIRT) algorithm solves the weighted least-squares optimization problem $argmin_{\boldsymbol{x}} \|\boldsymbol{A}\boldsymbol{x} - \boldsymbol{p}\|_{\boldsymbol{R}}$, where $\|\boldsymbol{A}\boldsymbol{x} - \boldsymbol{p}\|_{\boldsymbol{R}} = (\boldsymbol{A}\boldsymbol{x} - \boldsymbol{p})^T \boldsymbol{R}(\boldsymbol{A}\boldsymbol{x} - \boldsymbol{p})$ and $\boldsymbol{R} = (r_{kl}) \in \mathbb{R}^{M \times M}$ is a diagonal matrix with $r_{kk} = \left(\sum_l a_{kl}\right)^{-1}$ [12]. The following iterative formula is known to converge to the weighted least-squares minimum:

$$\boldsymbol{x}^k = \boldsymbol{x}^{k-1} + \boldsymbol{C}\boldsymbol{A}^T \boldsymbol{R}(\boldsymbol{p} - \boldsymbol{A}\boldsymbol{x}^{k-1}), \tag{4.1}$$

where $\boldsymbol{C} = (c_{kl}) \in \mathbb{R}^{N \times N}$ is a diagonal matrix with $c_{ll} = \left(\sum_k a_{kl}\right)^{-1}$.

4.2.2 Dynamic tomographic model

The conventional algebraic tomography model described in section 4.2.1 assumes the scanned object to remain stationary throughout the acquisition process. This assumption is no longer valid in dynamic CT. Therefore, the standard model has to be generalized to deal with dynamic objects.

A dynamic object can be represented as a time series of images $\boldsymbol{x}_r \in \mathbb{R}^N$, where $r \in \{1, \ldots, R\}$ is the time index, with R the total number of time frames. During the acquisition, the gantry rotates multiple times around the object while acquiring projections. The projections of subscan r are represented by $\boldsymbol{p}_r \in \mathbb{R}^{M_r}$. The sparse matrix $\boldsymbol{A}_r \in \mathbb{R}^{M_r \times N}$ is the corresponding forward projection matrix. If the object is assumed stationary during each time frame, the acquisition of the dynamic process can be modelled as follows:

$$\begin{bmatrix} \boldsymbol{A}_1 & 0 & \cdots & 0 \\ 0 & \boldsymbol{A}_2 & & 0 \\ \vdots & & \ddots & \vdots \\ 0 & 0 & \cdots & \boldsymbol{A}_R \end{bmatrix} \begin{bmatrix} \boldsymbol{x}_1 \\ \boldsymbol{x}_2 \\ \vdots \\ \boldsymbol{x}_R \end{bmatrix} = \tilde{\boldsymbol{A}}\tilde{\boldsymbol{x}} = \tilde{\boldsymbol{p}}, \tag{4.2}$$

where $\tilde{\boldsymbol{A}}$ represents the block diagonal matrix consisting of blocks $\boldsymbol{A}_1, \ldots, \boldsymbol{A}_R$, $\tilde{\boldsymbol{x}} = (\boldsymbol{x}_1^T, \ldots, \boldsymbol{x}_R^T)^T \in \mathbb{R}^{RN}$ and $\tilde{\boldsymbol{p}} = (\boldsymbol{p}_1^T, \ldots, \boldsymbol{p}_R^T)^T \in \mathbb{R}^{\sum_{r=1}^R M_r}$ [2, 6]. Notice that the dynamic computed tomography model does not take deformation during a single time frame into account. As a result, deformation artefacts will occur if excessive motion takes place during a single time frame (more than a single voxel). To remedy this, the acquisition time of a single time frame can be reduced.

The dynamic model Eq. 4.2, however, does not include the dependencies of the object between different time frames. The temporal dependencies between the subsequent images $\boldsymbol{x}_r$ can be modelled as follows. Each image $\boldsymbol{x}_r$ is regarded as a discretisation of $f_r(\boldsymbol{y})$ ($\boldsymbol{y} \in \mathbb{R}^3$). A deformation between two time points can be described as; $f_r(\boldsymbol{y}) = f_{r'}(\boldsymbol{y} + \boldsymbol{v}_{r'r}(\boldsymbol{y}))$ with $\boldsymbol{v}_{r'r}(\boldsymbol{y})$ the DVF from time point r' to

r. The discretized version of the previous equation comes down to interpolation:

$$\boldsymbol{x}_r = \boldsymbol{\tau}_{r'r}\boldsymbol{x}_{r'}, \tag{4.3}$$

with the operator $\boldsymbol{\tau}_{r'r} : \mathbb{R}^N \to \mathbb{R}^N$ transforming the image of the object at time frame r' to its state at time frame r. For many interpolation methods (e.g., nearest neighbour, linear or cubic interpolation), the operator $\boldsymbol{\tau}_{r'r}$ is actually a linear operator and thus $\boldsymbol{\tau}_{r'r} \in \mathbb{R}^{N\times N}$.

The transformations $\boldsymbol{\tau}_{..}$ can be included in the tomographic model:

$$\tilde{\boldsymbol{A}}\tilde{\boldsymbol{x}} = \tilde{\boldsymbol{A}} \begin{bmatrix} \boldsymbol{x}_1 \\ \vdots \\ \boldsymbol{x}_R \end{bmatrix} = \tilde{\boldsymbol{A}} \begin{bmatrix} \boldsymbol{\tau}_{r1} \\ \vdots \\ \boldsymbol{\tau}_{rR} \end{bmatrix} \boldsymbol{x}_r \tag{4.4}$$

and thus,

$$\mathcal{A}_r \boldsymbol{x}_r = \tilde{\boldsymbol{p}}, \tag{4.5}$$

with

$$\mathcal{A}_r = \begin{bmatrix} \boldsymbol{A}_1\boldsymbol{\tau}_{r1} \\ \vdots \\ \boldsymbol{A}_R\boldsymbol{\tau}_{rR} \end{bmatrix}, \tag{4.6}$$

the operator transforming the object at time frame r to the projections $\tilde{\boldsymbol{p}}$, which are acquired over the whole experiment (or a subset of the time frames). Notice that in Eq. 4.5 the time dependency is modelled by the operator $\mathcal{A}_r$, in contrast with Eq. 4.2. As a result, the number of unknowns is reduced from RN to N with the same number of equations.

Note that modelling the temporal dependencies with DVFs allows for an accurate description if the deformation is a diffeomorphism. In other words, the DVFs are differentiable and have a differentiable inverse, such as elastic deformations. Unfortunately, fluid flow and structural changes such as the formation of cracks cannot be accurately described with these models. For fluid flow specialised reconstruction algorithms do exist [5,11]. In future research these algorithms could be combined with the proposed MoVIT framework to take both kinds of deformations into account.

4.2.3 MotionVector-based Iterative Technique

Assuming that the deformation of the object during the acquisition is known, an approximation of the solution of Eq. 4.5 can be found with the MoVIT algorithm. The basic steps of MoVIT are shown in Algorithm 1. In iteration k, the current reconstruction of time frame r, $\boldsymbol{x}_r^k$, is transformed to each of the other time frames $r' \in \mathcal{N}_r$ with the deformation operator $\boldsymbol{\tau}_{rr'}$ and $\mathcal{N}_r$ the set of neighbouring time frames of time frame r. With this transformed reconstruction and the projections of that particular time frame, an ARM (e.g., ART, SART, SIRT, ...) update $\boldsymbol{q}$ is calculated. These ARM updates are then transformed back to the time frame r using $\boldsymbol{\tau}_{rr'}^{-1}$ with weight $w_{rr'}$. The weights $w_{rr'}$ are normalized such that $\sum_{r' \in \mathcal{N}_r} w_{rr'} = 1$. The proposed calculation of the weights will be explained in Section 4.2.4. Afterwards, the transformed updates added to the MoVIT update $\boldsymbol{u}$. This MoVIT update is then added to the current reconstruction, resulting in $\boldsymbol{x}_r^{k+1}$. This scheme is repeated until the stop criterion is met or a maximum number of MoVIT iteration is reached.

Algorithm 1: Basic steps of the MoVIT algorithm.

```
Calculate initial reconstruction x_r^0
k = 0
while stop criterion is not met do
    u = 0
    for r' ∈ N_r do
        s = τ_rr' x_r^k ;              ▷ Transform reconstruction to r'
        z = ARM(s, p_r') ;             ▷ Calculate ARM update
        l = τ_rr'^-1 z ;               ▷ Inverse transform ARM update to r
        u = u + w_rr' l ;              ▷ weight and add to total update
    end
    x_r^{k+1} = x_r^k + u
    k = k + 1
end
```

The MoVIT framework can be implemented with any algebraic reconstruction method such as ART, SART, or SIRT. In the rest of this work, SIRT will be the method underlying MoVIT[12]. To reconstruct the object at time frame r, the framework results in following algorithm:

$$\boldsymbol{x}_r^{k+1} = \boldsymbol{x}_r^k + \sum_{r' \in \mathcal{N}_r} w_{rr'} \boldsymbol{\tau}_{rr'}^{-1} \boldsymbol{C}_{r'} \boldsymbol{A}_{r'}^T \boldsymbol{R}_{r'} (\boldsymbol{p}_{r'} - \boldsymbol{A}_{r'} \boldsymbol{\tau}_{rr'} \boldsymbol{x}_r^k), \tag{4.7}$$

where $\boldsymbol{C}_r = (c_{r,kl}) \in \mathbb{R}^{N \times N}$ is a diagonal matrix with $c_{r,ll} = (\sum_k a_{kl})^{-1}$ and $\boldsymbol{R}_r = (r_{r,kl}) \in \mathbb{R}^{M_r \times M_r}$ is a diagonal matrix with $r_{r,kk} = (\sum_l a_{kl})^{-1}$. An overview of a single MoVIT iteration is given in Figure 4.2.

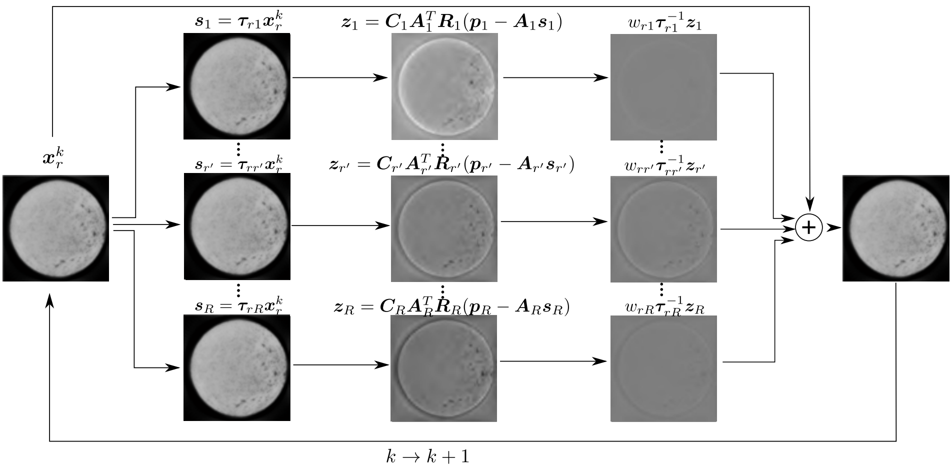

Figure 4.2: Schematic representation of a single iteration of the MoVIT algorithm implemented with SIRT updates.

4.2.4 Deformation estimation

The deformation operators $\boldsymbol{\tau}_{rr'}$ and their inverse (see Algorithm 1) are unknown and have to be estimated. To this end, each time frame is first conventionally reconstructed, for example with SIRT, using only the projections corresponding to that time frame. Afterwards, these conventional reconstructions $(\boldsymbol{c}_1, \boldsymbol{c}_2, \ldots, \boldsymbol{c}_R)$ are pairwise registered with each other, resulting in DVFs. In this work, the registration needed to estimate the parameters $\boldsymbol{\mu}_{rr'}$ of a b-spline deformation model was performed with Elastix [13]. The metric of the image registration algorithm is the mean squared difference (MSD) and thus the registration algorithm solves:

$$\boldsymbol{\mu}_{rr'} = \operatorname{argmin}_{\boldsymbol{\mu}} \left(\frac{1}{N} \sum_{i=1}^{N} \left(c_{r',i} - (\boldsymbol{\tau}(\boldsymbol{\mu})\boldsymbol{c}_r)_i\right)^2 \right), \tag{4.8}$$

where $c_{r',i}$ is the i^{th} element of $\boldsymbol{c}_{r'}$ and $(\boldsymbol{\tau}(\boldsymbol{\mu})\boldsymbol{c}_r)_i$ is the i^{th} element of $\boldsymbol{\tau}(\boldsymbol{\mu})\boldsymbol{c}_r$. The transform $\boldsymbol{\tau}_{r'r}$ is in theory also the inverse of $\boldsymbol{\tau}_{rr'}$. However, the exact solution of non-rigid image registration is often non-unique or nonexistent. Therefore, it is crucial to determine the direct inverse deformation field of the obtained DVF. This inverse DVF can be calculated with the method described in Chen et al. [14]. Evidently, it is unnecessary to determine the transform $\boldsymbol{\tau}_{rr}$ and its inverse as they are the identity transform. Note that other image registration algorithms, such as optical flow algorithms and digital volume correlation methods, are compatible as well with the MoVIT frame work [15]. The weights $w_{rr'}$ reflect the accuracy of the corresponding DVFs and are calculated as follows:

$$w_{rr'} = \frac{\exp(-(k_{rr'}/b)^2)}{\sum_{l \in \mathcal{N}_r} \exp(-(k_{rl}/b)^2)}, \tag{4.9}$$

where $k_{rr'} = N^{-1} \sum_i \left(c_{r,i} - (\boldsymbol{\tau}(\boldsymbol{\mu}_{rr'})\boldsymbol{c}'_r)_i\right)^2$ corresponds to the MSD between the reconstructed time frame and the transformed reconstruction of the time frame r'. The parameter b regulates the magnitude of the weights. If the MSD of a time frame equals b, the weight of that time frame will be exp(1) times smaller than the weight of the reconstructed time frame. The proposed method was implemented in Matlab, and the forward and back projections were performed with the ASTRA toolbox [16, 17, 18]. An overview of the complete framework is shown in Figure 4.3.

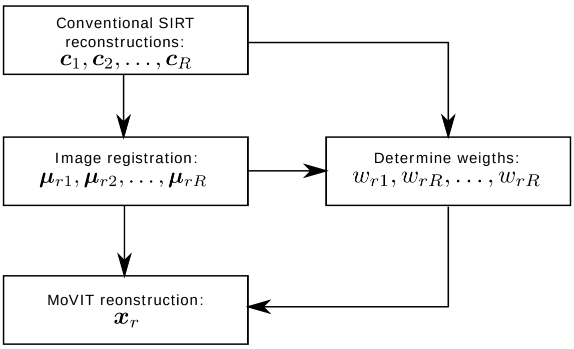

Figure 4.3: Schematic representation of the full MoVIT reconstruction pipeline.

4.3 Experiments and results

In subsection 4.3.1, the reconstruction methods, employed in the experiments, are explained. The MoVIT method is compared to conventional reconstruction methods in numerical simulations (subsection 4.3.3) and on an experimental dataset of polyurethane foam under compression (subsection 4.3.4). The results of these experiments are discussed in section 4.4.

4.3.1 Reconstruction methods

The proposed MoVIT algorithm was compared against two conventional reconstruction algorithms which are independently applied on each time frame. The first conventional algorithm is the Feldkamp-David-Kress (**FDK**) algorithm, resulting in the reconstructions $\boldsymbol{f}_1, \boldsymbol{f}_2, \ldots, \boldsymbol{f}_R$, where $\boldsymbol{f}_r \in \mathbb{R}^N$ [19]. The second algorithm is the **SIRT** algorithm (see Section 4.2.1) which results in the reconstructions $\boldsymbol{c}_1, \boldsymbol{c}_2, \ldots, \boldsymbol{c}_R$.

Furthermore, the MoVIT algorithm was compared to straightforward extensions of FDK and SIRT. In the following, the method is demonstrated with FDK reconstructions. An equivalent strategy was also used for the SIRT reconstructions. In a first step, the conventional FDK reconstructions are registered to each other:

$$\boldsymbol{\alpha}_{rr'} = \operatorname{argmin}_{\boldsymbol{\alpha}} \left(\frac{1}{N} \sum_{i=1}^{N} \left(f_{r',i} - (\boldsymbol{\tau}(\boldsymbol{\alpha}) \boldsymbol{f}_r)_i \right)^2 \right), \tag{4.10}$$

where $\alpha_{rr'}$ are the b-spline parameters describing the deformation from time frame r to time frame r'. Subsequently, the mean reconstructions $\boldsymbol{f}_{m,1}, \boldsymbol{f}_{m,2}, \ldots, \boldsymbol{f}_{m,R}$ are then calculated as follows: $\boldsymbol{f}_{mr'} = \sum_{r \in \mathcal{N}_r} z_{rr'} \boldsymbol{\tau}(\boldsymbol{\alpha}_{rr'}) \boldsymbol{f}_r$, where $z_{rr'} = \exp\left[-(k_{rr'}/b)^2\right] \left(\sum_{l \in \mathcal{N}_r} \exp\left[-(k_{rl}/b)^2\right] \right)^{-1}$ and $k_{rr'} = N^{-1} \sum_{i=1}^{N} (f_{r',i} - (\boldsymbol{\tau}(\boldsymbol{\alpha}_{rr'}) \boldsymbol{f}_r)_i)^2$. This technique combined with SIRT or FDK will be referred to as **SIRTmean** and **FDKmean**, respectively.

Lastly, the **MoVIT** method, as described in section 4.2, with the result of SIRTmean $\boldsymbol{c}_{mr}$ as initialisation will be used.

4.3.2 Figures of merit

The methods were evaluated using three figures of merit: mean squared error (MSE), the structural similarity index (SSIM) and feature similarity index (FSIM).

MSE: The MSE can be calculated with $N^{-1} \sum_{n=1}^{N} (\boldsymbol{s}_n - \boldsymbol{t}_n)^2$, where $\boldsymbol{s}$ is the calculated reconstruction and $\boldsymbol{t}$ is the ground truth.

SSIM: While MSE is a method which calculates absolute errors, SSIM quantifies the similarity of images as perceived by the human visual system [20]. The SSIM of a reconstruction is calculated as described in Wang et al. [20]. Since SSIM is a similarity measure, a *perfect* reconstruction has a SSIM of 1, the worst reconstruction a SSIM of 0.

FSIM: Similar to SSIM, FSIM is a method quantifying the perceived similarity of pictures [21]. In contrast to SSIM, it takes mainly the phase congruency and gradient magnitude into account.

4.3.3 Numerical simulations

Several numerical experiments were performed on a numerical phantom of a viscoelastic, open cell PU foam under compression. These models were provided by Huntsman (Everberg, Belgium) and are based on finite element simulations of different stages in the compression process. Four models were voxelised on an isotropic voxel grid of $400 \times 400 \times 400$ from which projections of size 100×100 were generated, in order to avoid the inverse crime of generating the data with the same model as the one used in the reconstruction [22]. The projections were simulated in an interleaved scanning protocol with 20 projections per time frame, where each time frame has an angular range of 180 degrees [23]. Poisson distributed noise was applied on the data, assuming an incoming beam intensity of 10^4 (photon count). During each time frame, the foam was compressed another 1.75% of the original sample height. The sample was reconstructed with a range of different reconstruction techniques as described in subsection 4.3.1.

The volume registration was performed with a b-spline deformation model with a control point spacing of 8 voxels. The b-spline parameters were optimized by minimizing the MSD in a multi-resolution framework. The SIRT and MoVIT algorithms were iterated until the lowest MSE was achieved. The optimal value of the parameter b, in terms of the MSE of the reconstructions, was 0.8 and was selected in this experiment. Renderings of the different reconstructions are shown in Figure 4.4.

Both the SSIM, FSIM and the MSE of the reconstructions were calculated in function of the photon count (I_0) and the number of projections per time frame (proj/time frame). These results are shown in Figure 4.5 and Figure 4.6, respectively.

4.3.4 Polyurethane dataset

A dynamic X-ray CT dataset was acquired by Inside Matters with a gantry-based high-resolution scanner [24]. A viscoelastic, open cell PU sample (provided by Huntsman) of 11 mm high was loaded in a compression stage which was mounted in the scanner. Each dataset (= time frame) consisted out of 2000 equiangular projections (1316×1312 pixels, pixel size $0.1\,mm$, tube voltage $65\,kV$, exposure time $35\,ms$) acquired over an angular range of 360 degrees. Between these scans, the sample was compressed $l \times 0.5\,mm$, where $l = 0, .., L-1$ is the time frame number. All reconstructions were calculated on a $1316 \times 1316 \times 401$ isotropic voxel grid with a voxel size of $16\,\mu m$. Each time frame was reconstructed with four different methods: 1) conventional SIRT with 2000 projections/time frame, 2) conventional SIRT with 1000 projections/time frame, 3) SIRTmean with 1000 projections/time frame and, 4) MoVIT with 1000 projections/time frame. MoVIT and SIRTmean estimate the deformation and includes the projections of a single neighbouring time frame (time frame $r+1$, except for the last time frame which uses time frame $r-1$) to the reconstruction of a particular time frame. The SIRT reconstruction with 2000 projections has thus the best possible quality that the MoVIT reconstruction can achieve by incorporating the projections of a single neighbouring time frame.

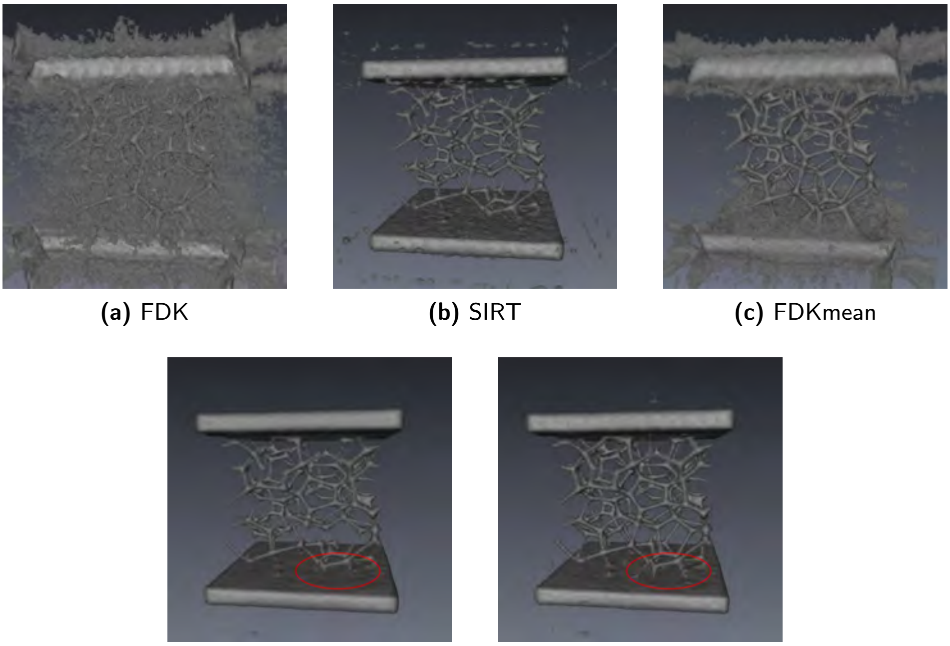

(a) FDK **(b)** SIRT **(c)** FDKmean

(d) SIRTmean **(e)** MoVIT

Figure 4.4: Renderings of the simulated reconstruction of the compression of a foam sample with different (a) FDK, (b) SIRT, (c) FDKmean, (d) SIRTmean, and (e) MoVIT. The red circles indicate example areas where the struts that are better reconstructed in the MoVIT reconstructions in comparison with the SIRTmean reconstruction.

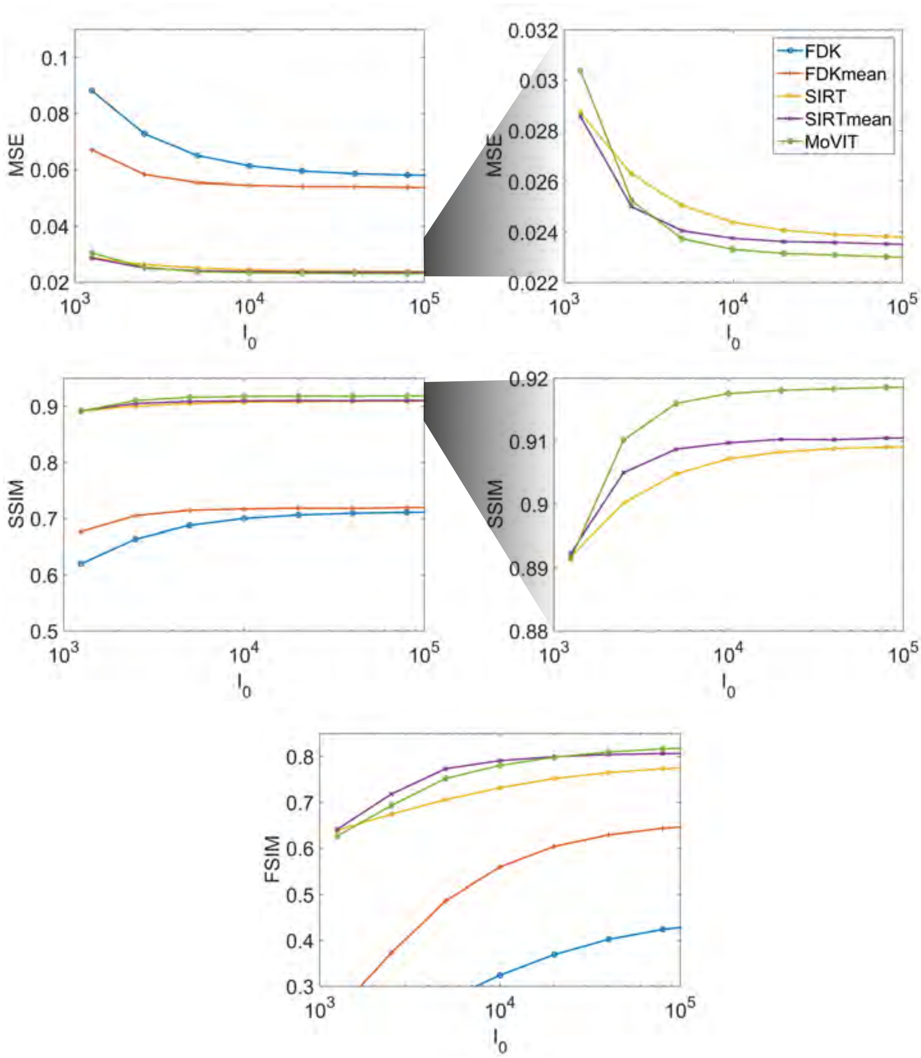

Figure 4.5: MSE, SSIM and FSIM of the reconstructions of the numerical phantoms (see Section 4.3.3) in function of the photon count I_0 and with 20 projections per time frame.

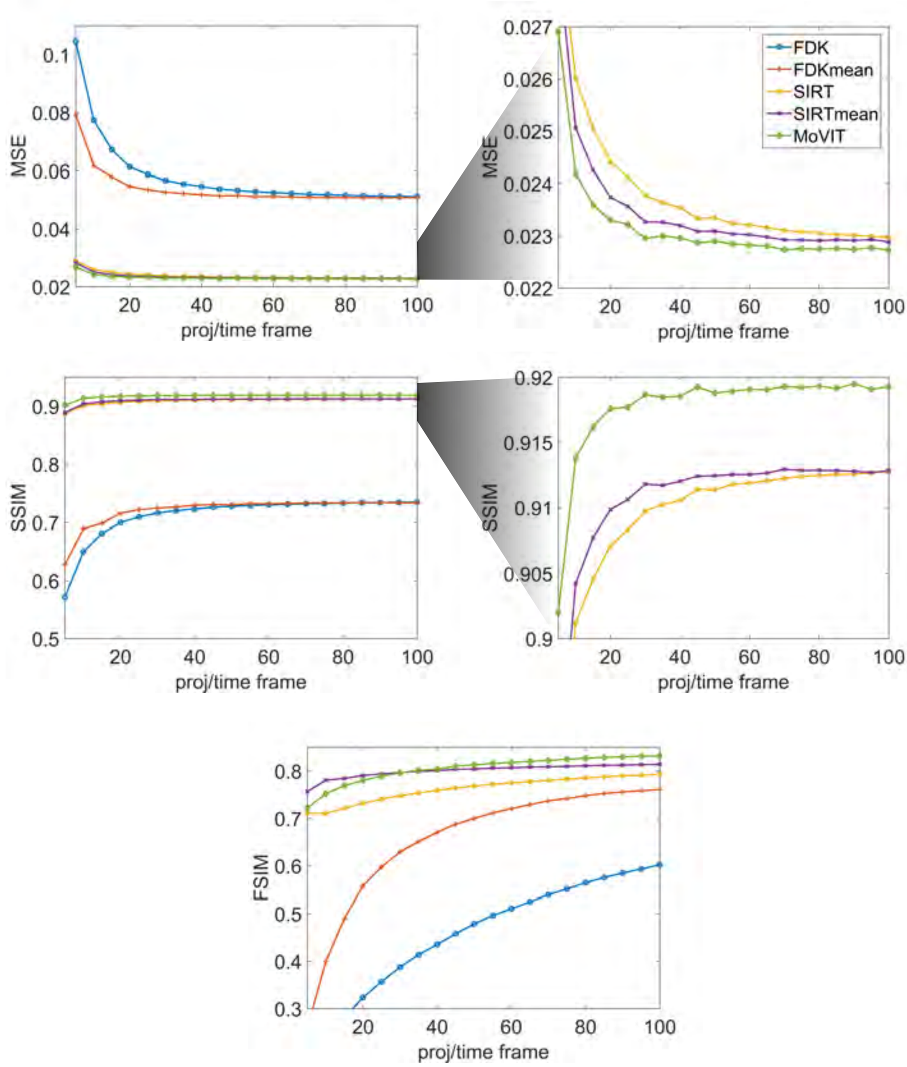

Figure 4.6: MSE, SSIM and FSIM of the reconstructions of the numerical phantoms (see Section 4.3.3) in function of the projections per time frame and a photon count of 10^4.

method	proj/time frame	noise standard deviation
SIRT	2000	$1,22 \times 10^{-5}$
SIRT	1000	$2,41 \times 10^{-5}$
SIRTmean (2 time frames)	1000	$1,63 \times 10^{-5}$
MoVIT (2 time frames)	1000	$1,47 \times 10^{-5}$
MoVIT (3 time frames)	1000	$1,19 \times 10^{-5}$

Table 4.1: The standard deviation of the noise of the different reconstructions at the third time frame of the polyurethane dataset. The standard deviation was measured in a large pore of the sample.

Reconstructions with only 1000 projections were performed with projections with projection numbers $1 + (r \bmod 2), 3 + (r \bmod 2), \ldots, M$, where r is the time frame number and M the total number of acquired projections/time frame. As such neighbouring time frames have interleaved projections. The volume registration was performed with a b-spline deformation model with a control point spacing of 8 voxels. The b-spline parameters were optimized by minimizing the MSD in a multi-resolution framework. Based on emperical evaluation the parameter b was chosen to be 0.6, which gave reasonable results. The MoVIT reconstruction was initialized with the SIRTmean reconstruction, after which 50 MoVIT iterations were performed. In Figure 4.7, the horizontal cross sections of the SIRT (1000 projections/time frame), SIRTmean and MoVIT reconstructions (2 time frames) are compared with the SIRT reconstruction with 2000 projections/time frame, which serves as the ground truth, with three different metrics (MSE, SSIM and FSIM). The standard deviation of the metrics was determined by calculating the metrics on 100 horizontal cross sections. Furthermore, Figure 4.7(d) shows the histogram of the region showed in Figure 4.9 for the different reconstructions of the third time frame. In Figure 4.8 and Figure 4.9, a vertical and horizontal cross section, reconstructed with SIRT, SIRTmean, MoVIT with one additional neighbouring time frame and MoVIT with two additional neighbouring time frames (time frame $r - 1$ and $r + 1$), of the third time frame are shown, respectively. To the last two reconstructions we will respectively refer to as MoVIT (2 time frames) and MoVIT (3 time frames). In Table 4.1, the standard deviation of the noise at the third time frame is reported for the described methods. This standard deviation was measured selecting a region (16106 voxels) inside of a big pore.

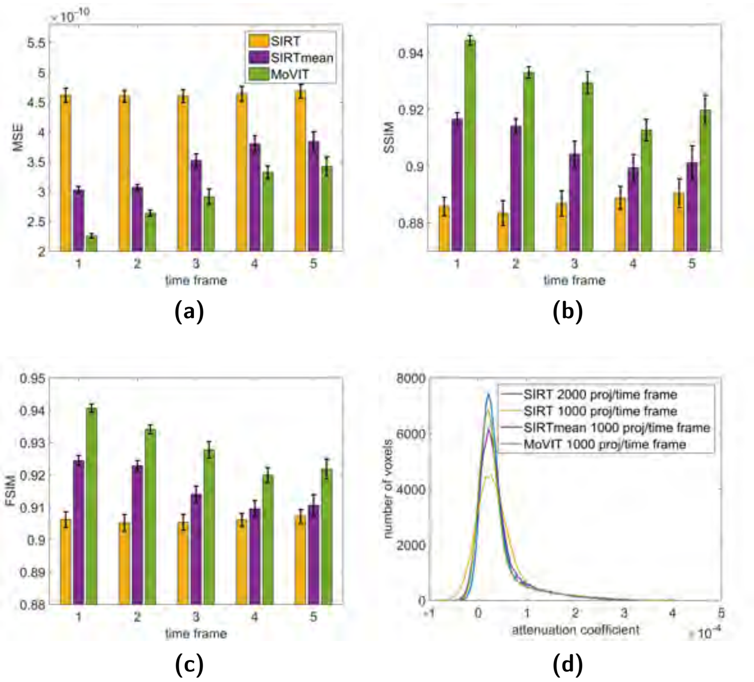

Figure 4.7: The mean MSE (a), SSIM (b) and FSIM (c) for the SIRT (yellow), SIRTmean (purple) and MoVIT with 2 time frames (green) reconstruction with 1000 proj/time frame (compared with the SIRT reconstruction with 2000 proj/time frame) for each time frame. The standard deviation of the metrics was determined by calculating the metrics on 100 horizontal cross sections. (d) shows the histogram of the region displayed in Figure 4.9 for the different reconstructions of the third time frame.

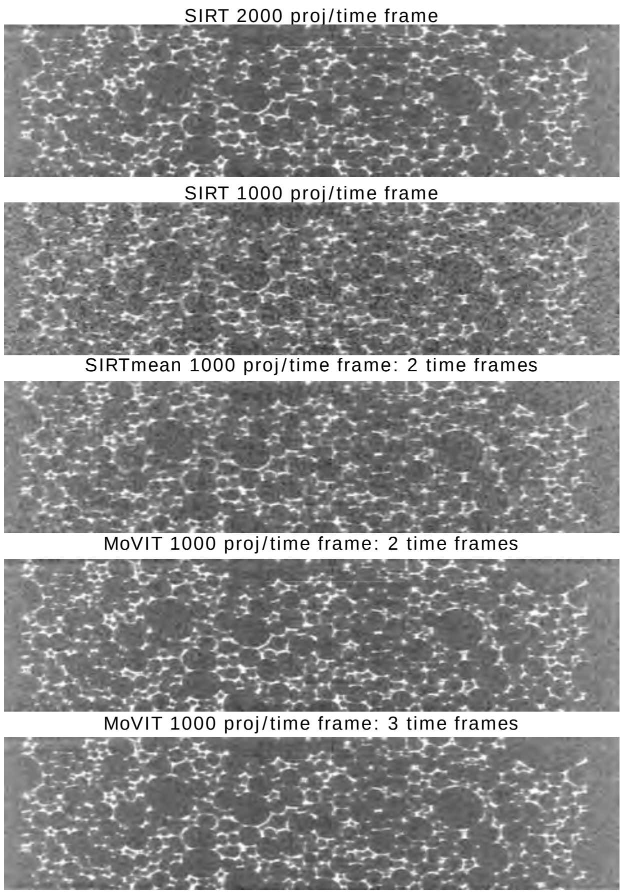

Figure 4.8: Vertical cross section through the third time frame of the polyurethane dataset.

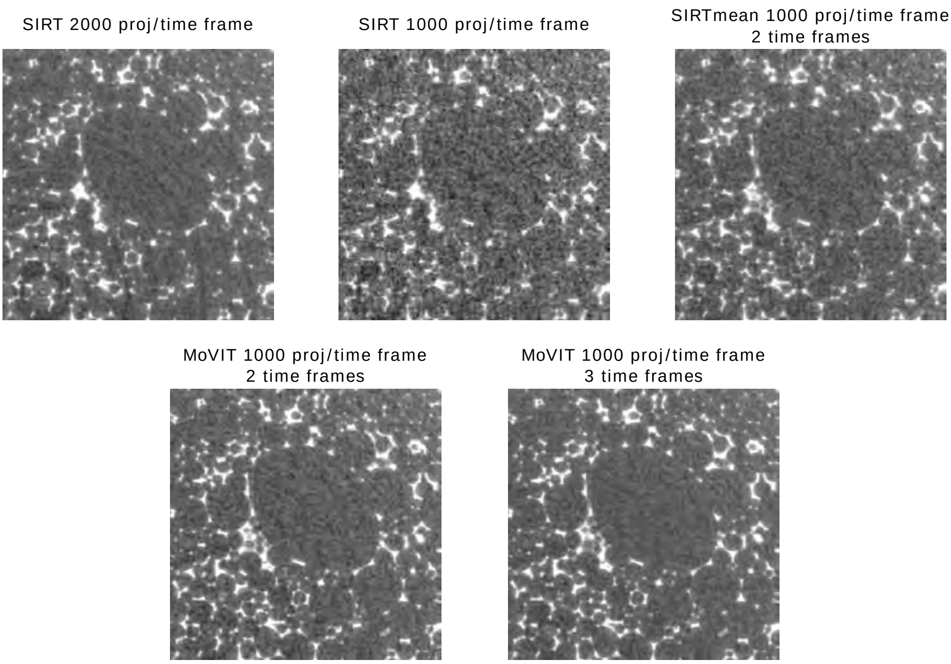

Figure 4.9: Zoomed horizontal cross section through the third time frame of the polyurethane dataset.

4.4 Discussion

4.4.1 Numerical simulations

Figure 4.4 shows renderings of the second time frame of the compressed foam sample computed with FDK (a), SIRT (b), SIRTmean (c), FDKmean (d) and MoVIT (e). FDK produces the worst results: the reconstruction is very noisy and the foam structures are very hard to differentiate from their surroundings. The FDKmean algorithm improves this reconstruction significantly, however high levels of noise are still present around the pressure plates due to cone beam artefacts. The SIRT and SIRTmean reconstructions show the foam structure nicely, however some struts of the foam are missing in the neighbourhood of the pressure plates. The MoVIT reconstruction shows the foam structure clearly and is able to reconstruct the struts close to the pressure plate better than the SIRT and SIRTmean reconstructions (see red circles in Figure 4.4 for example regions). In Figure 4.5, the MSE, SSIM, and FSIM are shown in function of the photon count. With respect to the MSE and SSIM, the MoVIT reconstruction performs best. This is also the case for the FSIM metric at high ($> 10^4$) photon counts or a high (> 30) number of projections per time frame. The SIRTmean method provides slightly worse reconstruction in terms of MSE and SSIM, but is an improvement over the conventional SIRT reconstructions. For low photon counts and low number of projections per time point, the FSIM of the SIRTmean are slightly better than the MoVIT reconstruction. Only at very low noise levels the MoVIT method results in a slightly worse reconstruction quality compared to the SIRT methods, which is caused by inaccurate deformation estimations on the very low SNR initial SIRT reconstructions. From Figure 4.6, similar conclusions can be drawn. Here the MoVIT method provides the best results with respect to the MSE and SSIM.

4.4.2 Polyurethane dataset

The results of the polyurethane foam dataset are shown in Figure 4.8 and Figure 4.9. The metrics of the different reconstructions in comparison with the SIRT reconstruction with 2000 proj/time frame are shown in Figure 4.7. The SIRT reconstruction with 2000 projections/time frame shows the foam structures very clearly. The SNR is sufficiently high to observe small foam structures. As can be expected, the noise of the SIRT reconstruction with only 1000 projections/time frame has a higher standard deviation than the SIRT reconstruction with 2000 projections/time frame and image details are obscured by the noise. The noise in the SIRTmean reconstruction (1000 projections/time frame) has a larger standard deviation as the SIRT reconstruction with 2000 projections/time frame, however it is considerably lower than that of the SIRT reconstruction with 1000 projections/-

time frame. The MoVIT method is able to lower the standard deviation of the noise even further. This is also reflected by the histograms in Figure 4.7(d), which show a narrower background peak for the methods with a smaller standard deviation. By taking an extra time frame into account the results of the MoVIT algorithm improve even further. The standard deviation of the noise is even lower of that of the SIRT reconstruction with 2000 projections/time frame. Additionally the MSE, SSIM and FSIM metrics (see Figure 4.7) reveal that the MoVIT reconstruction is more similar to the SIRT reconstruction with 2000 projections/time frame than the SIRTmean reconstruction. These results indicate that the improvement of MoVIT algorithm is not simply an averaging effect which improves the reconstruction. Indeed, incorporating more projections into the MoVIT reconstruction process not only improves the SNR but also improves the spatial resolution.

4.5 Conclusion

In this chapter, we have presented the MoVIT framework which aims to reconstruct dynamic CT datasets with high temporal resolution and spatial resolution. The MoVIT framework estimates the deformation between different time frames and enables including the projections of these time frames in the reconstruction of a certain time frame without introducing deformation artefacts. The method was validated on numerical simulations and a real dataset of polyurethane foam under compression. Both experiments showed an increase of reconstruction quality with respect to conventional reconstruction algorithms. The performed experiments show that the MoVIT algorithm is able to successfully exploit the data redundancy present in 4D-CT datasets. It allows lowering the acquisition time of a single time frame without compromising the SNR of the reconstructed images.

References

[1] G. Van Eyndhoven, K. J. Batenburg, and J. Sijbers, "Region-based iterative reconstruction of structurally changing objects in CT," *IEEE Trans. Image Process.*, vol. 23, pp. 909–919, 2014.

[2] G. Van Eyndhoven, K. J. Batenburg, D. Kazantsev, V. Van Nieuwenhove, P. D. Lee, K. J. Dobson, and J. Sijbers, "An iterative CT reconstruction algorithm for fast fluid flow imaging," *IEEE Trans. Image Process.*, vol. 24, no. 11, pp. 4446–4458, 2015.

[3] G. Myers, A. Kingston, T. Varslot, M. Turner, and A. P. Sheppard, "Dynamic tomography with a priori information," *Appl. Opt.*, vol. 50, pp. 2685–3690, 2011.

[4] V. Van Nieuwenhove, G. Van Eyndhoven, K. J. Batenburg, N. Buls, J. Vandemeulebroucke, J. De Beenhouwer, and J. Sijbers, "Local attenuation curve optimization

(LACO) framework for high quality low-dose cerebral perfusion CT," *Med. Phys.*, vol. 43(12), pp. 6429–6438, 2016.

[5] G. Van Eyndhoven, K. J. Batenburg, and J. Sijbers, "Region-based iterative reconstruction of structurally changing objects in CT," *IEEE Trans. Image Process.*, vol. 23, no. 2, pp. 909–919, 2014.

[6] D. Kazantsev, W. M. Thompson, W. R. B. Lionheart, G. Van Eyndhoven, A. P. Kaestner, K. J. Dobson, P. J. Withers, and P. D. Lee, "4D-CT reconstruction with unified spatial-temporal patch-based regularization," *Inverse Probl. Imag.*, vol. 9, pp. 447–467, May 2015.

[7] K. A. Mohan, S. V. Venkatakrishnan, J. W. Gibbs, E. B. Gulsoy, X. Xiao, M. De Graef, P. W. Voorhees, and C. A. Bouman, "TIMBIR: a method for time-space reconstruction from interlaced view," *IEEE Trans. Comp. Imaging*, vol. 1, pp. 96–111, 2015.

[8] M. Brehm, P. Paysan, M. Oelhafen, P. Kunz, and M. Kachelrieß, "Self-adapting cyclic registration for motion-compensated cone-beam CT in image-guided radiation therapy," *Med. Phys.*, vol. 39, no. 12, pp. 7603–7618, 2012.

[9] A. A. Isola, M. Grass, and W. J. Niessen, "Fully automatic nonrigid registration-based local motion estimation for motion-corrected iterative cardiac CT reconstruction," *Med. Phys.*, vol. 37, pp. 1093–1109, Mar. 2010.

[10] H. Yan, X. Zhen, M. Folkerts, Y. Li, T. Pan, L. Cervino, S. B. Jiang, and X. Jia, "A hybrid reconstruction algorithm for fast and accurate 4D cone-beam CT imaging.," *Med. Phys.*, vol. 41, p. 071903, Jul. 2014.

[11] C. P. V. Christoffersen, D. Hansen, P. Poulsen, and T. S. Sorensen, "Registration-based reconstruction of four-dimensional cone beam computed tomography.," *IEEE Trans. Med. Imaging*, vol. 32, pp. 2064–2077, Nov. 2013.

[12] J. Gregor and T. Benson, "Computational analysis and improvement of SIRT.," *IEEE Trans. Med. Imaging*, vol. 27, pp. 918–924, Jan. 2008.

[13] D. Rueckert, L. I. Sonoda, C. Hayes, D. L. G. Hill, M. O. Leach, and D. J. Hawkes, "Nonrigid registration using free-form deformations: application to breast MR images," *IEEE Trans. Med. Imaging*, vol. 18, no. 8, pp. 712–721, 1999.

[14] M. Chen, W. Lu, Q. Chen, K. J. Ruchala, and G. H. Olivera, "A simple fixed-point approach to invert a deformation field," *Med. Phys.*, vol. 35, no. 1, pp. 81–88, 2008.

[15] B. K. Bay, T. S. Smith, D. P. Fyhrie, and M. Saad, "Digital volume correlation: Three-dimensional strain mapping using X-ray tomography," *Exp. Mech.*, vol. 39, pp. 217–226, 1999.

[16] W. J. Palenstijn, K. J. Batenburg, and J. Sijbers, "Performance improvements for iterative electron tomography reconstruction using graphics processing units (GPUs)," *J. Struct. Biol.*, vol. 176, pp. 250–253, Nov. 2011.

[17] W. Van Aarle, W. J. Palenstijn, J. Cant, E. Janssens, F. Bleichrodt, A. Dabravolski, J. De Beenhouwer, and J. Sijbers, "Fast and flexible X-ray tomography using the ASTRA toolbox," *Opt. Express*, vol. 24, no. 22, pp. 25129–25147, 2016.

[18] W. J. Palenstijn, J. Bédorf, and K. J. Batenburg, "A distributed SIRT implementation for the ASTRA toolbox," in *Fully Three-Dimensional Image Reconstruction Radiology and Nuclear Medicine: Proc.*, pp. 166–169, Jun. 2015.

[19] L. A. Feldkamp, L. C. Davis, and J. W. Kress, "Practical cone-beam algorithm," *J. Opt. Soc. Am. A*, vol. 1, pp. 612–619, Jun. 1984.

[20] Z. Wang, A. C. Bovik, H. R. Sheikh, and E. P. Simoncelli, "Image quality assessment: From error visibility to structural similarity," *IEEE Trans. Image Process.*, vol. 13, no. 4, pp. 600–612, 2004.

[21] L. Zhang, L. Zhang, X. Mou, and D. Zhang, "FSIM : A feature similarity index for image quality assessment," *IEEE Trans. Image Proc.*, vol. 20, no. 8, pp. 2378–2386, 2011.

[22] J. Kaipio and E. Somersalo, "Statistical inverse problems: Discretization, model reduction and inverse crime," *J. Comput. Appl. Math.*, vol. 198, no. 2, pp. 493–504, 2007.

[23] A. Kaestner, B. Münch, P. Trtik, and L. Butler, "Spatiotemporal computed tomography of dynamic processes," *Opt. Eng.*, vol. 50, p. 123201, Dec. 2011.

[24] M. Dierick, D. Van Loo, B. Masschaele, J. Van den Bulcke, J. Van Acker, V. Cnudde, and L. Van Hoorebeke, "Recent micro-CT scanner developments at UGCT," *Nucl. Instr. Meth. Phys. Res. B*, vol. 324, pp. 35–40, Apr. 2014.

5
Conclusions

Dynamic processes during the acquisition of a computed tomography scan arise in numerous applications, both in the imaging system and the scanned object. In classical CT algorithms these dynamics are neglected. As a result, the reconstruction quality of the resulting images deteriorates in the presence of these dynamics. In this thesis, several CT algorithms were developed with an incorporated dynamic model in order to remove or diminish dynamic process related artefacts.

While the developed algorithms in this thesis are vastly different, they share a similar design:

1. An appropriate *dynamic model* is chosen to model the dynamics of the process as close as possible. These models have a number of unknown parameters that have to be estimated.

2. A method to *incorporate the dynamic model* into the (reconstruction) algorithm is developed.

3. To estimate the parameters of the chosen dynamic model an *objective function* is constructed. This objective function is often based on the method developed in the previous step. The optimal parameters are those that minimize the objective function. In order to develop an efficient algorithm, it is important that an evaluation of this objective function has a low computational complexity. Moreover, a convex objective function is highly desirable. However, in practice this is often not achievable.

In the following the main conclusions of Chapters 2-4 are drawn.

Chapter 2 – Dynamic intensity normalization

In this chapter, a dynamic flat field correction was introduced. The method was designed to normalize datasets acquired with a varying intensity of the incoming beam, as is often encountered in synchrotron facilities. In order to capture the dynamics of the incoming beam principal component analysis is performed on a set of flat fields, resulting in a set of eigen flat fields. A linear combination of these eigen flat fields is then used to individually normalize each projection. Experiments on a numerical phantom and on synchrotron datasets showed that both the projections and the reconstructions contain less or no flat field variability related artefacts compared to classical normalisation techniques.

Chapter 3 – Affine deformation estimation and correction in cone beam computed tomography

In this chapter, an affine deformation estimation and correction technique was proposed for cone beam computed tomography. This algorithm is able to estimate the affine deformation of an object, compared to a short reference scan, on every projection of the CT dataset. These estimates can then be used to correct the projections individually for the affine deformation resulting in a reconstruction, without deformation artefacts, of the object at the time point of the reference scan. After the correction of every projection of the dataset, an accurate reconstruction of the object at the time point of the reference can be obtained. Since the affine deformation estimation and correction is done directly in the projection domain, no time consuming reconstructions have to be performed. The proposed technique was validated on both numerical and real cone beam datasets. The results reveal that the technique is able to alleviate/remove deformation artefacts resulting from approximately affine deformations.

Chapter 4 – MoVIT: A tomographic reconstruction framework for 4D-CT

In this chapter, the Motion Vector-based Iterative Technique (MoVIT) was introduced. This technique aims at reconstructing 4D-CT dataset with a high temporal resolution and signal-to-noise ratio (SNR). In order to achieve this the deformation between the different time frames is estimated. This enables including the projections of these time frames in the reconstruction of a certain time frame without introducing deformation artefacts. The MoVIT framework was validated both on numerical and real datasets of polyurethane foam under compression. The results show that the MoVIT framework can significantly improve the reconstruction quality, in terms of the MSE, SSIM and FSIM metrics, and improve the SNR of the obtained images compared to a range of classical techniques.

This work as a whole made a step forward in the incorporation of dynamic processes into the algorithms surrounding CT. The proposed techniques clearly show that incorporation of well-chosen dynamic models in the algorithms can significantly improve the reconstruction quality.

A
List of common abbreviations

Common symbols

ARM	Algebraic Reconstruction Method
ART	Algebraic Reconstruction Technique
CBCT	Cone Beam Computed Tomography
CCD	Charge Coupled Device
CT	Computed Tomography
DVF	Deformation Vector Field
EFF	Eigen Flat Field
FBP	Filtered Back Projection
FDK	Feldkamp-David-Kress algorithm
FFC	Flat Field Correction
FSIM	Functional Similarity Index
GPU	Graphics Processing Unit
MoVIT	Motion Vector-based Iterative Technique
MSD	Mean Squared Distance
MSE	Mean Squared Error
PCA	Principal Component Analysis
RMSE	Root Mean Squared Error
ROI	Region Of Interest
SART	Simultaneous Algebraic Reconstruction Technique
SIRT	Simultaneous Iterative Reconstruction Technique
SNR	Signal-to-Noise Ratio
SSIM	Structural Similarity Index
TV	Total Variation

B
Scientific contributions

Journal articles

- V. Van Nieuwenhove, J. De Beenhouwer, F. De Carlo, L. Mancini, F. Marone, and J. Sijbers, *"Dynamic intensity normalization using eigen flat fields in X-ray imaging"*, Optics Express, vol. 23, no. 21, pp. 27975–27989, 2015.

- G. Van Eyndhoven, K. J. Batenburg, D. Kazantsev, V. Van Nieuwenhove, P. D. Lee, K. J. Dobson, and J. Sijbers, *"An iterative CT reconstruction algorithm for fast fluid flow imaging"*, IEEE Transactions on Image Processing, vol. 24, no. 11, pp. 4446-4458, 2015.

- V. Van Nieuwenhove, G. Van Eyndhoven, K.J. Batenburg, N. Buls, J. Vandemeulebroucke, J. De Beenhouwer, and J. Sijbers, *"Local Attenuation Curve Optimization (LACO) framework for high quality low-dose cerebral perfusion CT"*, Medical Physics, vol. 43, no. 12, pp. 6429—6438, 2016.

- V. Van Nieuwenhove, J. De Beenhouwer, T. De Schryver, L. Van Hoorebeke, and J. Sijbers, *"Data-driven affine deformation estimation and correction in come beam computed tomography"*, IEEE Transactions on Image Processing, vol. 26, no. 3, pp. 1441-1451, 2017.

- V. Van Nieuwenhove, J. De Beenhouwer, J. Vlassenbroeck, M. Brennan and J. Sijbers, *"MoVIT: A tomographic reconstruction framework for 4D-CT"*, Optics Express, vol. 25, no. 16, pp. 19236-19250, 2017.

Conference proceedings (full paper)

- V. Van Nieuwenhove, J. De Beenhouwer, T. De Schryver, L. Van Hoorebeke, and J. Sijbers, *"Affine deformation correction in cone beam computed tomogra-*

phy", Fully Three-Dimensional Image Reconstruction in Radiology and Nuclear Medicine, Newport, Rhode Island, USA, pp. 182-185, 2015.

- *V. Van Nieuwenhove*, J. De Beenhouwer, F. De Carlo, L. Mancini, F. Marone, and J. Sijbers, *"Dynamic Flat field correction in X-ray computed tomography"*, Optical Measurement Techniques for Structures and Systems (OPTIMESS) III , Antwerp, Belgium, pp. 343-352, 2016.

- *V. Van Nieuwenhove*, J. De Beenhouwer, J. Vlassenbroeck, M. Moesen, M. Brennan, and J. Sijbers, *"Registration Based SIRT: A reconstruction algorithm for 4D CT"*, 7th Conference on Industrial Computed Tomography, Leuven, Belgium, 2017.

Conference proceedings (extended abstract)

- *V. Van Nieuwenhove*, J. De Beenhouwer, and J. Sijbers, *"Compensation of time dependent affine transformations in fan and cone beam 4DCT"*, International Conference on Industrial Computed Tomography (ICT), Wels, Austria, 2014.

- *V. Van Nieuwenhove*, G. Van Eyndhoven, J. De Beenhouwer, and J. Sijbers, *"Compensation of affine deformations in fan and cone beam projections"*, Micro-CT User Meeting, Ostend, Belgium, pp. 187-189, 2014.

- J. Goyens, L. Mancini, *V. Van Nieuwenhove*, J. Sijbers, P. Aerts, *"Comparison of conventional and synchrotron microCT scanning of thin membranes in the inner ear"*, Micro-CT User Meeting, Brussels, Belgium, pp. 187-189, 2017.

Conference abstracts

- *V. Van Nieuwenhove*, G. Van Eynhoven, J. De Beenhouwer, and J. Sijbers, *"Combined Estimation of Affine Movement and Reconstruction in Tomography"*, International Congress on 3D Materials Science 2014, Annecy, France, 2014.

- G. Van Eyndhoven, K. J. Batenburg, D. Kazantsev, *V. Van Nieuwenhove*, P. D. Lee, K. J. Dobson, and J. Sijbers, *"A 4D CT reconstruction algorithm for fast liquid flow imaging"*, Applied Inverse Problems Conference, Helsinki, Finland, 2015.

- *V. Van Nieuwenhove*, J. De Beenhouwer, and J. Sijbers, *"A fast 4D CT reconstruction algorithm for affine deforming objects"*, Applied Inverse Problems Conference, Helsinki, Finland, 2015.

- *V. Van Nieuwenhove*, J. De Beenhouwer, and J. Sijbers, *"Registration Based SIRT: capturing the dynamics of polyurethane foam under compression "*, Visual analysis of dynamic processes, Rigi Kulm, Switzerland, 2017.

- *V. Van Nieuwenhove*, G. Van Eyndhoven, J. De Beenhouwer, and J. Sijbers, *"A 4D reconstruction algorithm for cerebral perfusion CT "*, Meeting on Tomography and Applications, Milan, Italy, 2017.